Iowa State University
Digital Repository

Graduate Theses and Dissertations

Iowa State University Capstones, Theses and Dissertations

2017

Understanding electronic defects in organic solar cells: Defect identification, characterization & mitigation

Tanvir Muntasir
Iowa State University

Follow this and additional works at: https://lib.dr.iastate.edu/etd

Part of the Electrical and Electronics Commons

Recommended Citation

Muntasir, Tanvir, "Understanding electronic defects in organic solar cells: Defect identification, characterization & mitigation" (2017). *Graduate Theses and Dissertations*. 16262.
https://lib.dr.iastate.edu/etd/16262

This Dissertation is brought to you for free and open access by the Iowa State University Capstones, Theses and Dissertations at Iowa State University Digital Repository. It has been accepted for inclusion in Graduate Theses and Dissertations by an authorized administrator of Iowa State University Digital Repository. For more information, please contact digirep@iastate.edu.

المنارة للاستشارات

www.manaraa.com

Understanding electronic defects in organic solar cells: Defect identification, characterization & mitigation

by

Tanvir Muntasir

A dissertation submitted to the graduate faculty

in partial fulfillment of the requirements for the degree of

DOCTOR OF PHILOSOPHY

Major: Electrical Engineering

Program of Study Committee:
Vikram Dalal, Co-Major Professor
Sumit Chaudhary, Co-Major Professor
Rana Biswas
Jaeyoun Kim
Mani Mina

The student author and the program of study committee are solely responsible for the content of this dissertation. The Graduate College will ensure this dissertation is globally accessible and will not permit alterations after a degree is conferred.

Iowa State University

Ames, Iowa

2017

Copyright © Tanvir Muntasir, 2017. All rights reserved.

المنارة للاستشارات

www.manaraa.com

DEDICATION

To my parents, Md. Surut Zaman and Tauhida Begum, for their unconditional support.

المنارة للاستشارات
www.manaraa.com

TABLE OF CONTENTS

	Page
LIST OF FIGURES	v
LIST OF TABLES	x
NOMENCLATURE	xi
ACKNOWLEDGMENTS	xii
ABSTRACT	xiii
CHAPTER 1 INTRODUCTION TO BULK-HETEROJUNCTION ORGANIC SOLAR CELLS	1
1.1 Why Solar Photovoltaic	1
1.2 Status of Solar Photovoltaic	3
1.3 Organic Solar Cells	4
1.4 Working Principle of Organic Solar Cells	6
CHAPTER 2 DEFECTS IN ORGANIC SOLAR CELLS: MOTIVATION & OBJECTIVE	8
2.1 Background & Motivation	8
2.2 Status in Most Thoroughly Studied Polymer (P3HT) in OPV	10
2.3 Beyond P3HT	11
2.4 Understanding Defects in Organics is Still in Its Infancy	12
2.5 Objective	13
2.6 References	14
CHAPTER 3 ORGANIC SOLAR CELL FABRICATION & CHARACTERIZATION	16
3.1 Organic Solar Cell Structure	16
3.2 Organic Solar Cell Fabrication	19
3.3 Organic Solar Cell Characterization	20
3.4 References	28

www.manaraa.com

CHAPTER 4 UNDERSTANDING DEFECT DISTRIBUTION IN POLYTHIOPHENES VIA COMPARISON OF REGIOREGULAR AND REGIORANDOM SPECIES 30

4.1 Introduction 30
4.2 Results & Discussions 35
4.3 Conclusion 53
4.4 Experimental 53
4.5 References 55

CHAPTER 5 DEFECTS IN SOLUTION-PROCESSED DITHIENYLSILOLE-BASED SMALL-MOLECULE PHOTOVOLTAIC THIN-FILMS 59

5.1 Introduction 59
5.2 Existence of Trap States in The Bandgap of DTS-$(FBTTh_2)_2$ 61
5.3 Maximum Trap Emission Rate 67
5.4 Bulk & Interface Properties 69
5.5 tDOS Energy Spectra from Admittance Spectroscopy 72
5.6 Probing Deeper Trap States Using Low-frequency CV-profiling 74
5.7 Conclusion 77
5.8 Experimental 78
5.9 References 80

CHAPTER 6 POLYMER CRYSTALLINITY & ELECTRONIC DEFECTS IN ORGANIC SOLAR CELLS 83

6.1 Material Selection 83
6.2 Sample Organic Solar Cell Preparation 85
6.3 Optimized Device Performance 91
6.4 Probing Polymer Crystallinity using Raman Spectroscopy 94
6.5 Defect Study Based on Polymer Crystallinity 96
6.6 Conclusion 103
6.7 References 104

المنارة للاستشارات

www.manaraa.com

LIST OF FIGURES

Page

Figure 1.1 World net electricity generation by energy source, 2012-2040 published by U.S. Energy Information Administration (EIA).......... 1

Figure 1.2 Illustration of predicted primary energy use in upcoming years and energy generation from different sources 2

Figure 1.3 Illustration of global cumulative growth of photovoltaic capacity reported by Solar Power Europe (SPE) 3

Figure 1.4 Illustration of levelized cost of electricity generation from different technologies reported by Institute for Energy Research (IER).......... 4

Figure 1.5 Illustration of basic structure of an organic solar cell....................... 5

Figure 1.6 Simplified band-diagram of an organic solar cell illustrating the basic operation 6

Figure 2.1 Band diagram depiction of defect states in the donor leading to trapping of holes, causing carrier recombination............................. 9

Figure 2.2 Conceptual illustration of density of states in an organic semiconductor 10

Figure 2.3 Several types of defects theoretically postulated for a 10 monomer chain length P3HT 11

Figure 3.1 An example of organic solar cell on P-i-N structure 17

Figure 3.2 Corresponding band-diagram of an organic solar cell on P-i-N structure.. 17

Figure 3.3 An example of organic solar cell on N-i-P structure 18

Figure 3.4 Corresponding band-diagram of an organic solar cell on N-i-P structure.. 18

Figure 3.5 Illustration of typical solar cell IV curve and different parameters ... 21

Figure 3.6 Illustration of a typical solar cell dark IV curve 22

Figure 3.7 Illustration of a typical QE plot 23

www.manaraa.com

Figure 3.8 Schematic diagram of the QE setup 24

Figure 3.9 Band diagram showing the Schottky junction formed at the metal-active layer interface 25

Figure 4.1 (a) Structure of RR-P3HT, (b) Structure of RRa-P3HT, and (c) Schematic of an organic photovoltaic device 34

Figure 4.2 Illustration of dedoping over time in vacuum and dark at 325K 36

Figure 4.3 -F dC/dF plotted with frequency at different temperatures for (a) RR-P3HT:PCBM, (b) RRa-P3HT:PCBM, (c) RR-P3HT and (d) RRa-P3HT 37

Figure 4.4 Arrhenius plot of emission peak vs. 1/T for RR-P3HT:PCBM, RRa-P3HT:PCBM, RR-P3HT and RRa-P3HT 38

Figure 4.5 Illustration of the overlap of tDOS energy spectra using measured ATEF at different temperatures. For RR-P3HT:PCBM, RRa-P3HT: PCBM, RR-P3HT, and RRa-P3HT 39

Figure 4.6 Inverse of capacitance squared is plotted with applied bias (Mott-Schottky relation) for (a) RR-P3HT:PCBM, (b) RRa-P3HT:PCBM, (c) RR-P3HT and (d) RRa-P3HT 40

Figure 4.7 Illustration of rolling slope in Mott-Schottky plot at low frequency. Top left: RR-P3HT:PCBM with 200Hz as the frequency of AC signal, RRa-P3HT:PCBM with 100Hz, RR-P3HT with 100Hz, and RRa-P3HT with 100Hz 41

Figure 4.8 Defect density measured using profiler equation are plotted with reverse bias for (a) RR-P3HT:PCBM, (b) RRa-P3HT:PCBM, (c) RR-P3HT and (d) RRa-P3HT 43

Figure 4.9 Illustration of derivative of the defect density with respect to applied bias (calculated from profiler equation) plotted with reverse bias 44

Figure 4.10 Ratio of capacitance and geometric capacitance versus frequency for the four devices investigated 45

Figure 4.11 Illustration of tDOS energy spectra for (a) P3HT:PCBM devices, and (b) P3HT-only devices 45

Figure 4.12 Illustration of shift of capacitance-frequency profile toward lower frequency with lower temperature. (a) RR-P3HT:PCBM, (b) RRa-P3HT:PCBM, (c) RR-P3HT, and (d) RRa-P3HT 47

المنارة للاستشارات

www.manaraa.com

Figure 4.13 Nyquist plot at different applied biases obtained from impedance spectroscopy under illumination (1 sun) for both RR-P3HT:PCBM and RRa-P3HT:PCBM. It is evident that the impedance range of the RRa- is larger that the regular one 49

Figure 4.14 Illustration of the results of impedance spectroscopy (IS) and light IV under illumination (1 sun) of RR-P3HT:PCBM (in blue) and RRa-P3HT:PCBM (in red) as a function of applied bias. (a) Minority carrier mobility, (b) minority carrier transit time, (c) mobility-lifetime product, and (d) minority carrier lifetime, (e) Light IV 50

Figure 4.15 Conceptual illustration of the energy diagram of RR-P3HT and RRa-P3HT with the distribution of extracted traps. Trap distribution in presence of PCBM is illustrated with dashed band 51

Figure 5.1 (a) Schematic of the device structure employed. (b) Illuminated current-density vs. voltage characteristics of DTS-$(FBTTh_2)_2$: $PC_{70}BM$ devices 62

Figure 5.2 Illustration of the band-diagram of the complete device 63

Figure 5.3 Band-diagram showing the donor-cathode and acceptor-cathode interface separately for the case of active-layer of DTS-$(FBTTh_2)_2$: $PC_{70}BM$ blend (a) Band-diagram showing the Schottky-junction formed at the cathode-DTS-$(FBTTh_2)_2$ interface. (b) Band-diagram showing the Ohmic-contact formed at the cathode-$PC_{70}BM$ interface.. 64

Figure 5.4 (a) Mott-Schottky profiles of DTS-$(FBTTh_2)_2$:$PC_{70}BM$ regular-film at different small-signal frequencies. (b) Mott-Schottky profiles of DTS-$(FBTTh_2)_2$ regular-film at different small-signal frequencies. (c) Capacitance versus frequency plots of DTS-$(FBTTh_2)_2$:$PC_{70}BM$ regular-film at different temperatures with 0 V DC-bias. (d) Capacitance versus frequency plots of DTS-$(FBTTh_2)_2$ regular-film at different temperatures with 0 V DC-bias. The arrow indicates left shift in curves at lower temperatures 66

Figure 5.5 Derivatives of the CF-profiles of (a) DTS-$(FBTTh_2)_2$:$PC_{70}BM$ regular-film, and (b) DTS-$(FBTTh_2)_2$ regular-film versus small-signal frequency (at different temperatures). The arrows indicate the characteristic-frequency at which the change is capacitance is maximum 68

Figure 5.6 Arrhenius plot of the characteristic-frequency (F_m) versus inverse of temperature 68

المنارة للاستشارات

www.manaraa.com

Figure 5.7 Illustration of Nyquist plot of both regular and thick-film of DTS-$(FBTTh_2)_2$:$PC_{70}BM$. The negative of the imaginary part of impedance ($Z_{imaginary}$) is plotted with the real part of impedance (Z_{real}). Data points are obtained applying small-signal frequency ranging from 1 MHz to 100 mHz. The black arrows indicate the peak of the semicircles and the green arrows indicate the quasi-straight line portion of the profile 71

Figure 5.8 Illustration of tDOS energy spectra of regular and thick-films of DTS-$(FBTTh_2)_2$:$PC_{70}BM$ and DTS-$(FBTTh_2)_2$........ 73

Figure 5.9 Illustration of tDOS energy spectra, extracted from low-frequency CV-profiling, for the regular and thick-films of DTS-$(FBTTh_2)_2$: $PC_{70}BM$ and DTS-$(FBTTh_2)_2$. The solid lines represent the corresponding Gaussian fits........ 76

Figure 5.10 Trap concentration of different bands in tDOS energy spectra plotted with corresponding mean energy........ 77

Figure 6.1 Molecular structure of PTB7 polymer........ 83

Figure 6.2 Molecular structure of PffBT4T-2OD polymer........ 84

Figure 6.3 Schematic diagram of PffBT4T-2OD based organic solar cell on P-i-N structure........ 86

Figure 6.4 Corresponding band-diagram of PffBT4T-2OD based organic solar cell on P-i-N structure........ 87

Figure 6.5 Schematic diagram of PffBT4T-2OD based organic solar cell on N-i-P structure........ 88

Figure 6.6 Corresponding band-diagram of PffBT4T-2OD based organic solar cell on N-i-P structure........ 89

Figure 6.7 Schematic diagram of the ultrasonic-spray pyrolysis setup built for this study........ 90

Figure 6.8 Light IV curve of the optimized PffBT4T-2OD solar cell on P-i-N structure........ 91

Figure 6.9 QE spectra of the optimized PffBT4T-2OD solar cell on P-i-N structure........ 92

Figure 6.10 Light IV curve of the optimized PffBT4T-2OD solar cell on N-i-P structure........ 92

المنارة للاستشارات
www.manaraa.com

Figure 6.11 QE spectra of the optimized PffBT4T-2OD solar cell on N-i-P structure.......... 93

Figure 6.12 Light IV with device parameters, QE plot and device structure of PTB7 device.......... 94

Figure 6.13 Obtained Raman spectra from PffBT4T-2OD and PTB7 films. Top two plots show single peak fitting and bottom two plots show double peak fitting 95

Figure 6.14 Illustration of Mott-Schottky profile of PffBT4T-2OD and PTB7 films. The top figure is extracted from CV-profiling at high frequency and the bottom figure is extracted from CV-profiling at low frequency.......... 97

Figure 6.15 Illustration of trap distribution in the bandgap of PTB7 and PffBT4T-2OD in both P-i-N (standard) and N-i-P (inverted) structure.......... 99

Figure 6.16 Normalized QE plotted with photon energy for PTB7 and PffBT4T devices on both structures.......... 100

Figure 6.17 Normalized QE plotted with photon energy on semi-log scale for PTB7 and PffBT4T devices on both structures 101

Figure 6.18 Illustration of the PffBT4T-2OD:PCBM and PTB7:PCBM type-II heterojunction 102

www.manaraa.com

LIST OF TABLES

Page

Table 4.1 Obtained activation energy (E_a) and ATEF from temperature dependent CF measurements 38

Table 4.2 Doping, built-in voltage and Fermi energy extracted from CV measurements 41

Table 4.3 Calculated position of the peak of the Gaussian distribution of defect from depth profile 42

Table 4.4 Summary of tDOS energy spectra fitted parameters 46

Table 5.1 Summary of photovoltaic performance of DTS-$(FBTTh_2)_2$:$PC_{70}BM$ devices 62

Table 5.2 Summary of extracted bulk and interface properties of DTS-$(FBTTh_2)_2$ and DTS-$(FBTTh_2)_2$-cathode interface, respectively, from CV-profiling and IS 70

Table 5.3 Summary of extracted fitting parameters from Gaussian fit of the bands in tDOS energy spectra 74

Table 6.1 Comparison of properties between PffBT4T-2OD and PTB7 84

Table 6.2 Crystalline and amorphous peak position of PffBT4T-2OD and PTB7 film 95

Table 6.3 Summary of crystallinity parameter of PffBT4T-2OD and PTB7 film 96

Table 6.4 Summary of extracted parameters from CV-profiling on PffBT4T-2OD and PTB7 films 98

Table 6.5 Extracted Urbach energy of tail states near HOMO and LUMO of PffBT4T-2OD and PTB7 103

www.manaraa.com

NOMENCLATURE

PV	Photovoltaic
OPV	Organic Photovoltaic
P3HT	Poly(3-hexyltiophene)
PTB7	Poly[[4,8-bis[(2-ethylhexyl)oxy]benzo[1,2-b:4,5-b']dithiophene-2,6-diyl][3-fluoro-2-[(2-ethylhexyl)carbonyl]thieno[3,4-b]thiophenediyl]
PffBT4T-2OD	Poly[(5,6-difluoro-2,1,3-benzothiadiazol-4,7-diyl)-alt-(3,3’’’-di(2-octyldodecyl)-2,2’;5’,2’’;5’’,2’’’-quaterthiophen-5,5’’’-diyl)
Pff	PffBT4T-2OD
DTS-$(FBTTh_2)_2$	7,7'-(4,4-bis(2-ethylhexyl)-4H-silolo[3,2-b:4,5-b']-dithiophene-2,6-diyl)bis(6-fluoro-4-(5'-hexyl-[2,2'-bithiophen]-5-yl)benzo[c][1,2,5] thiadiazole)
DTS	DTS-$(FBTTh_2)_2$
CV	Capacitance-voltage
CF	Capacitance-frequency
HOMO	Highest Occupied Molecular Orbital
LUMO	Lowest Unoccupied Molecular Orbital
ETL	Electron Transport Layer
HTL	Hole Transport Layer

www.manaraa.com

ACKNOWLEDGMENTS

I would like to show my gratitude towards Dr. Vikram Dalal and Dr. Sumit Chaudhary for their guidance toward learning the diverse field of semiconductors and giving me the opportunity to work under them. I would also like to thank Dr. Rana Biswas, Dr. Jaeyoun Kim and Dr. Mani Mina for serving as my committee members and their continued guidance through this research. I would like to thank my wife for her encouragements. Special thanks to John Carr for providing me training on capacitance measurements. In addition, special thanks to Max Noack, Wai Leung, Moneim, Ryan, Pranav, Mehran, Liang for their help and discussions. I would like to thank National Science Foundation for providing the funding. Finally, I would like to thank all my lab-mates and friends for their support.

المنارة للاستشارات
www.manaraa.com

ABSTRACT

Among several thin-film based solar technologies, organic or hybrid organic- inorganic photovoltaic (PV) technology is envisioned as a foremost candidate towards the realization of ubiquitous and economical solar power. Organic PV (OPV) technology has the advantages of facile fabrication suitable for roll-to-roll processing on flexible substrates, high optical absorption coefficients, low- temperature processing, and easy tunability by chemical doping. Substantial progress has resulted from the optimization of materials processing parameters and the emergence of new materials. Recent works have achieved conversion efficiencies exceeding 13%, but with the Shockley-Queisser limit calculated at 21% for single-junction cells, there are many facets left for improvement. Recombination and mobility deficits are considered two of the largest bottlenecks in organic solar cells – accounting for 50-60% of losses. Electronic defect bands can significantly affect both these bottlenecks, introducing charged trap sites, Shockley-Read-Hall centers, or both. Thus, the identification, characterization and mitigation of these defects largely remain open and important areas of interest. This research work focuses on understanding defects in OPVs through systematic identification of defects, characterization of their nature and exploring approaches for defect mitigation. An understanding on the physical origin of electronic defects is developed using several organic materials. Different approaches have been explored to minimize these defects to optimized device performance. This work shows the distribution of defect states in the bandgap of organic semiconductors used in OPVs with accurate energetic location and interpret on their physical origin. Exploring ways to minimized electronic defects, this work demonstrates improvement of power-conversion-efficiency and stability of OPVs

www.manaraa.com

CHAPTER I

INTRODUCTION TO BULK-HETEROJUNCTION ORGANIC SOLAR CELLS

1.1 Why Solar Photovoltaics

We all know that the energy demand is going up every year mainly due to population growth. There is also global warming, we have the oil that is peaking and there are pollutions. Figure 1.1 illustrates the world's net electricity generation by energy source (2012-2040) published by U.S. Energy Information Administration (EIA). This figure illustrates the growth of energy demand in coming years and predicts the energy generation from different sources. Figure 1.2 illustrates similar information published by German advisory council on global change.

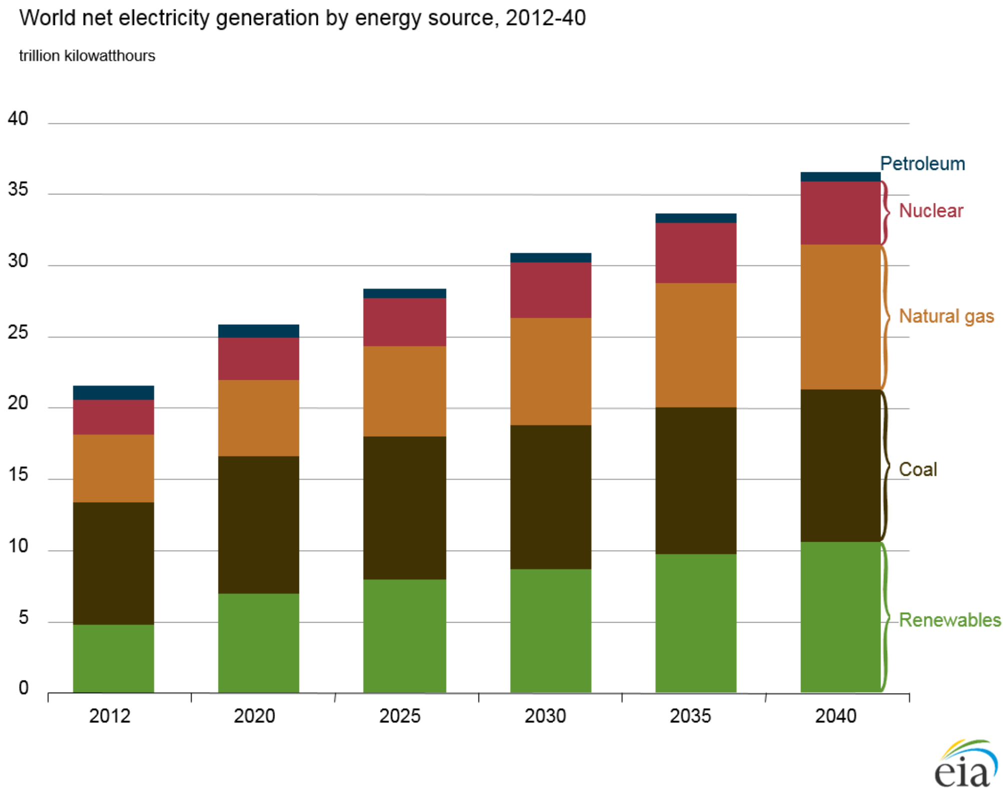

Figure 1.1: World net electricity generation by energy source, 2012-2040 published by U.S. Energy Information Administration (EIA).

www.manaraa.com

From figure 1.2, it is apparent that we will be facing an energy gap that is as big as today's consumption by the year of 2050. Figure 1.2 shows the primary energy use in exajoule per annum where 1 exajoule is equivalent to 10^{18} joule. Current global energy use is around 14 TW. The power supply gap to be covered by 2050 is projected to be at least 14 TW. To cap CO_2 at 550 ppm, which is twice the pre-industrial level, most of this additional energy needs to come from carbon-free sources. The solution can only be renewable sources because in the end we will only have the renewables left. Solar energy is the largest renewable energy source (120,000 TW), but the challenge is to convert the solar energy at competitive cost.

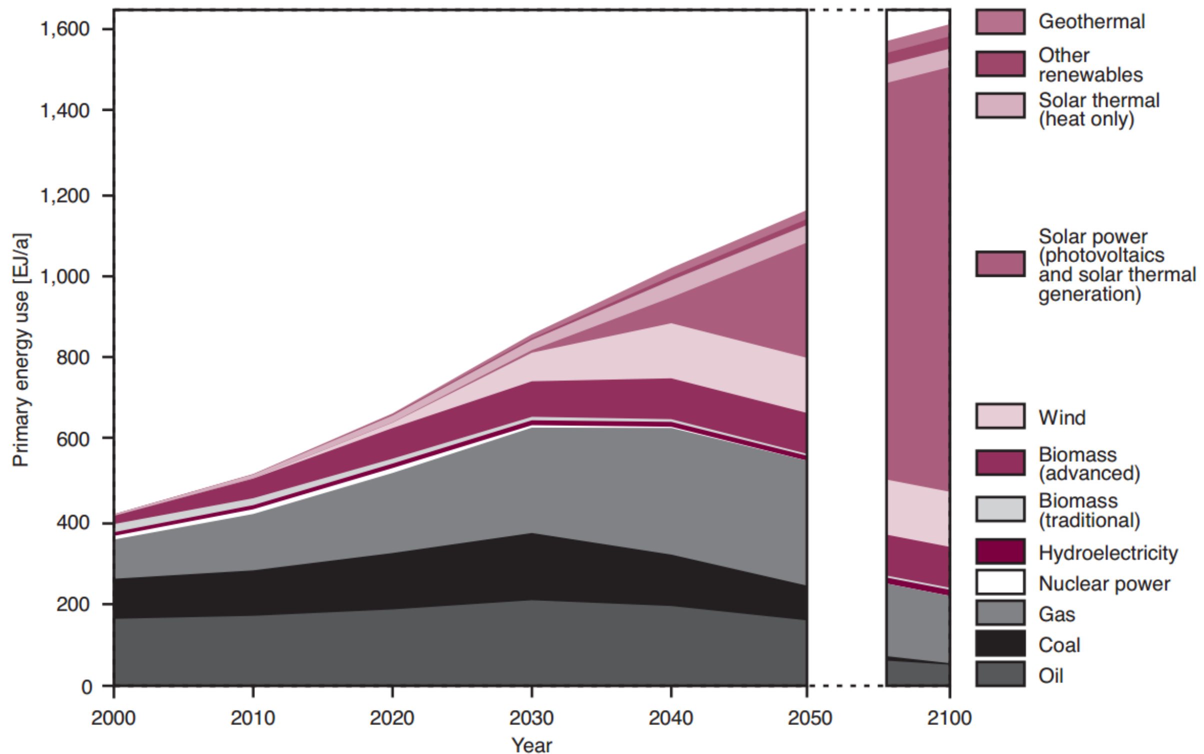

Figure 1.2: Illustration of predicted primary energy use in upcoming years and energy generation from different sources.

المنارة للاستشارات
www.manaraa.com

1.2 Status of Solar Photovoltaics

Solar photovoltaic is doing well. The world has seen an exponential growth in the solar photovoltaic capacity. Figure 1.3 Illustrates global cumulative growth of photovoltaic capacity reported by Solar Power Europe (SPE). The average growth of photovoltaic capacity has been calculated as 45% per year. Although there has been exponential growth in photovoltaic capacity, still further increase in photovoltaic capacity is required to meet the energy demand.

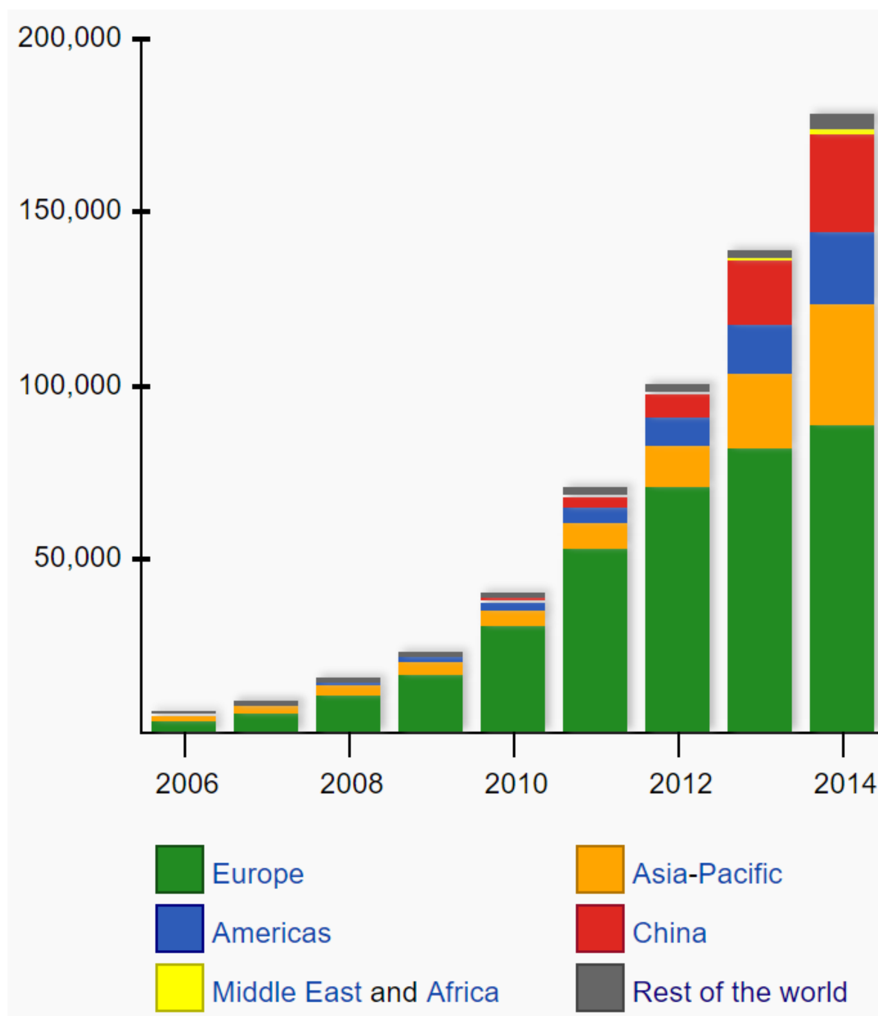

Figure 1.3: Illustration of global cumulative growth of photovoltaic capacity reported by Solar Power Europe (SPE).

المنارة للاستشارات
www.manaraa.com

1.3 Organic Solar Cells

We have already discussed in the previous sections that solar energy is the largest source of renewable energy while the challenge is to convert this energy at competitive cost. Figure 1.4 illustrates the estimated levelized cost of electricity generation from different technologies (reported by Institute of Energy Research). This figure shows that the solar photovoltaic is not comparatively cheap currently. This fact makes organic solar cells attractive.

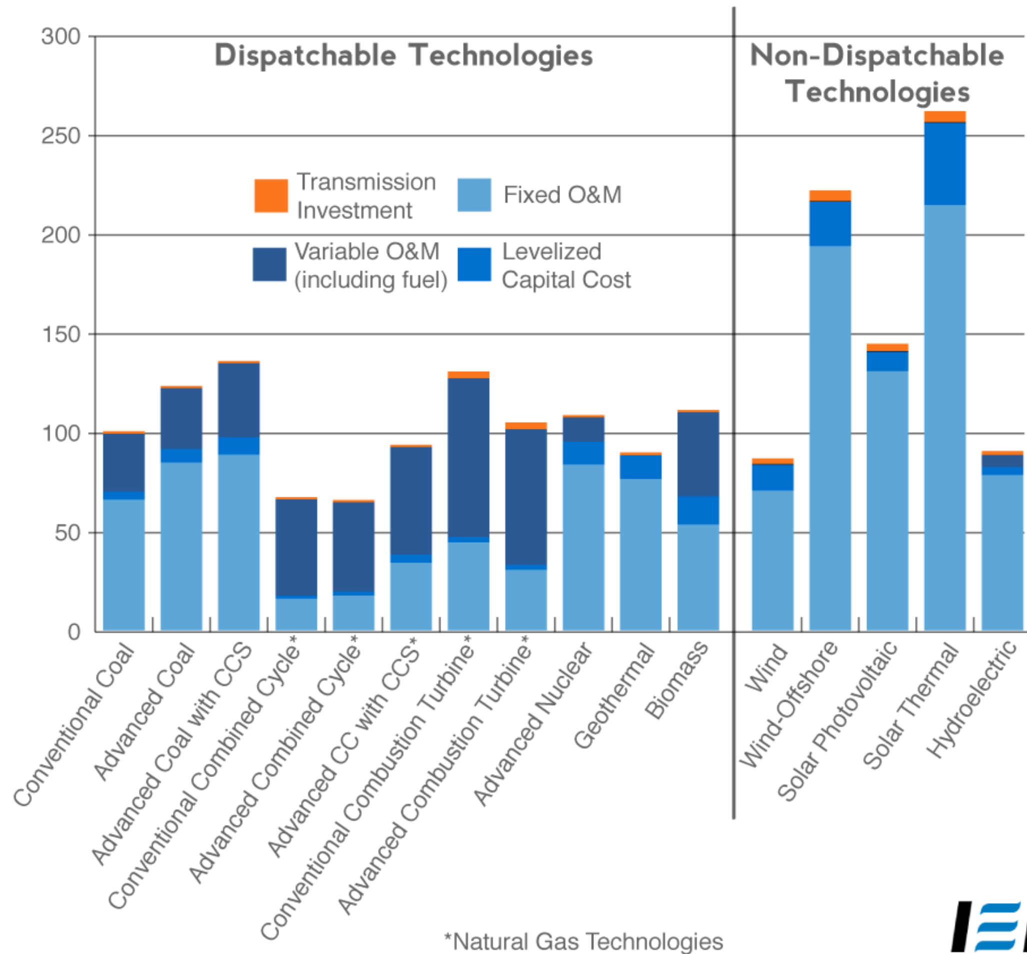

Figure 1.4: Illustration of levelized cost of electricity generation from different technologies reported by Institute for Energy Research (IER).

المنارة للاستشارات
www.manaraa.com

Organic solar cells have the advantage of low temperature and solution based processing. This advantage makes organic solar cells a potential candidate for large scale roll-to-roll production on flexible substrates. Therefore, organic solar cells are attractive as it is potentially cheaper than other solar cell technologies. The name “organic” comes from the use of polymers or small-molecules in the solar cells. These organic materials have high optical absorption coefficient.

The major challenge in organic solar cells is the power conversion efficiency and stability of these devices. More than 10% efficiency has already been achieved while the Shockley–Queisser (SQ) limit has been calculated as 33%. SQ limit indicates the theoretical limit of efficiency that can be obtained from a particular solar cell. The difference in reported highest obtained efficiency and SQ limit indicates that there are many opportunities left to improve efficiency of organic solar cells. This work on organic solar cell is focused on improvement of efficiency and stability of these devices.

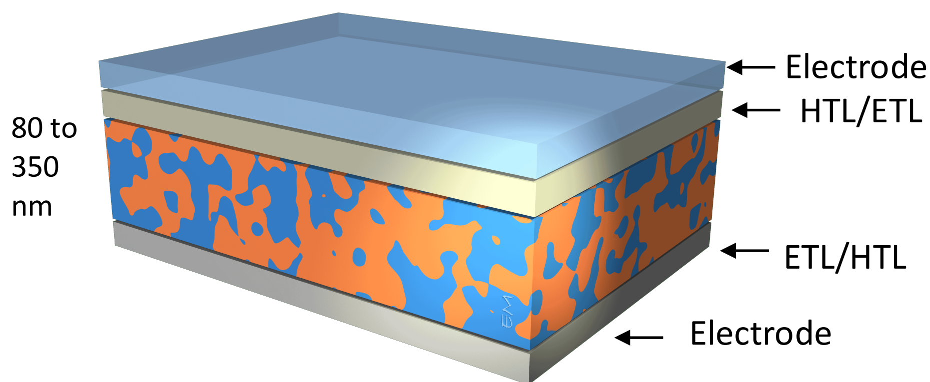

Figure 1.5: Illustration of basic structure of an organic solar cell

www.manaraa.com

1.4 Working Principle of Organic Solar Cells

Figure 1.5 illustrates the basic structure of a bulk-heterojunction organic solar cell. The layer illustrated using blue and orange color is the main layer. In this layer, light energy gets absorbed. For this reason, this layer is called the active layer. The active layer is consisted of interpenetrating network of donor and acceptor. To introduce donor and acceptor let us look at the simplified band-diagram illustrated in figure 1.6. This band-diagram is showing that donor acceptor creates a type-II heterojunction. Donor materials are either polymer or small-molecules. Donor materials have high absorption coefficient. Thus, light energy gets absorbed in this material. There are number of donor materials commercially available which are being used in organic solar cells.

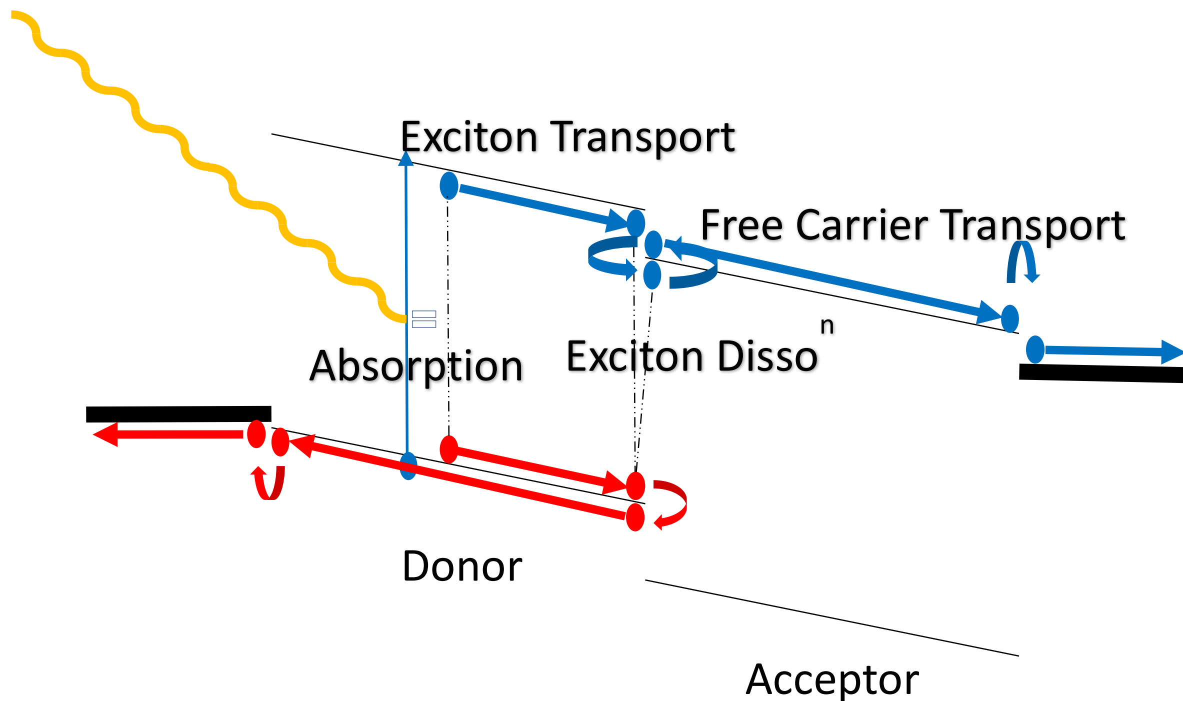

Figure 1.6: Simplified band-diagram of an organic solar cell illustrating the basic operation

المنارة للاستشارات
www.manaraa.com

Electron hole pair generates in the donor material due to absorption of photon energy. This phenomenon is illustrated in figure 1.6. This electron-hole pair is called exciton. One limitation of donor materials is that their dielectric constant is low, in the range of 3 to 4. So, the electron-hole pair binding energy is high (0.3-0.5) in these materials. As the electron-hole pair binding energy is high, the electron-hole pair moves as a unit.

In general, donor materials are p-type organic semiconductor and acceptor materials are n-type organic semiconductor. Simplified band-diagram of donor and acceptor is illustrated in figure 1.6. After the generation of electron-hole pair in the donor material, it moves as a unit due to high binding energy. But, the limitation is that the diffusion length of electron-hole pair is only about 10 nm while for effective absorption of photon energy the thickness of the active layer has to be much higher than 10nm. So, the structural challenge is that we need to have a mechanism so that this electron-hole pair will be dissociated within its diffusion length. Donor-acceptor interpenetrating network is utilized in order to achieve this goal.

Electron sees lower energy when the electron-hole pair reaches the donor-acceptor interface. As a result, the electron-hole pair gets dissociated at the donor-acceptor interface. To makes sure that most of the electron-hole pair reaches the donor-acceptor interface within its diffusion length, the donor-acceptor interpenetrating network is utilized. This interpenetrating network of donor-acceptor is termed as bulk-heterojunction.

There are electron transport layer and hole transport layer on top and bottom of the active layer. After the exciton dissociation, free electron moves in the acceptor which is n-type and reaches the electron transport layer and gets collected. Similarly, free hole moves in the donor material which is p-type and reaches the hole transport layer and finally gets collected.

المنارة للاستشارات
www.manaraa.com

CHAPTER II

DEFECTS IN ORGANIC SOLAR CELLS: MOTIVATION & OBJECTIVE

2.1 Background & Motivation

Among several thin-film based solar technologies, organic (polymers/oligomers) or hybrid organic- inorganic PV technology is envisioned as a foremost candidate towards the realization of ubiquitous and economical solar power [1-3]. Organic PV (OPV) technology has the advantages of facile fabrication suitable for roll-to-roll processing on flexible substrates, high optical absorption coefficients, low- temperature processing, and easy tunability by chemical doping. Substantial progress has resulted from the optimization of materials processing parameters and the emergence of new materials [4,5]. To date, power conversion efficiency exceeding 10% has recently been achieved in a single junction OPV cell [6]. However, the state-of-the-art device architecture is the so-called bulk-heterojunction (BHJ) in which the active layer is coated from a blend of donor and acceptor species. The nanoscale phase separation in a BHJ active layer alleviates the mismatch between exciton diffusion length (~10 nm) and optical absorption length (> 100 nm). However, there still exists a disparity between optical absorption length and charge transport scale. Recent works have achieved conversion efficiencies exceeding 10%, but with the Shockley-Queisser limit calculated at 21% for single-junction cells,[7] there are many facets left for improvement.

Recombination and mobility deficits are considered two of the largest bottlenecks in these devices – accounting for 50-60% of losses. Defect bands can significantly affect both these bottlenecks, introducing charged trap sites, Shockley-Read-Hall centers, or both. The former alters the internal electronic landscape, diminishing carrier mobility and reducing

المنارة للاستشارات
www.manaraa.com

exciton diffusion length, while the latter leads to free-carrier loss, especially if the defect exists near a domain interface.[8] This is illustrated in figure 2.1.

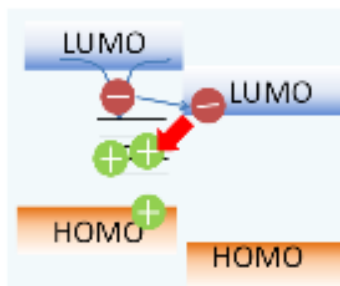

Figure 2.1: Band diagram depiction of defect states in the donor leading to trapping of holes, causing carrier recombination.

Figure 2.2 shows a conceptual illustration of density of states in an organic semiconductor. When speaking of organic semiconductors, the highest occupied molecular orbital (HOMO) and lowest unoccupied molecular orbital (LUMO) are commonly referenced as the valence band and conduction band, respectively. HOMO and LUMO are separated by a bandgap. Within this energy gap, it is well known that both shallow and deep-level states can be present.[8] Origins of these traps can be extrinsic or intrinsic. Extrinsic traps stem from chemical impurities introduced during material synthesis, device fabrication or when exposed to oxygen or moisture. Intrinsic traps stem from morphological disorder inherent in the amorphous nature of typical organic films.

Defects in the band-gap introduce recombination centers and charged point sites. Recombination centers lead to loss of free carriers through trap-assisted recombination. Charged defects is detrimental to carrier mobility and transport. As already discussed, recombination and mobility deficits are considered two of the largest bottlenecks in OPVs -

www.manaraa.com

accounting for 50-60% of losses. Thus, the identification, characterization and mitigation of these defects largely remain open and important areas of interest.

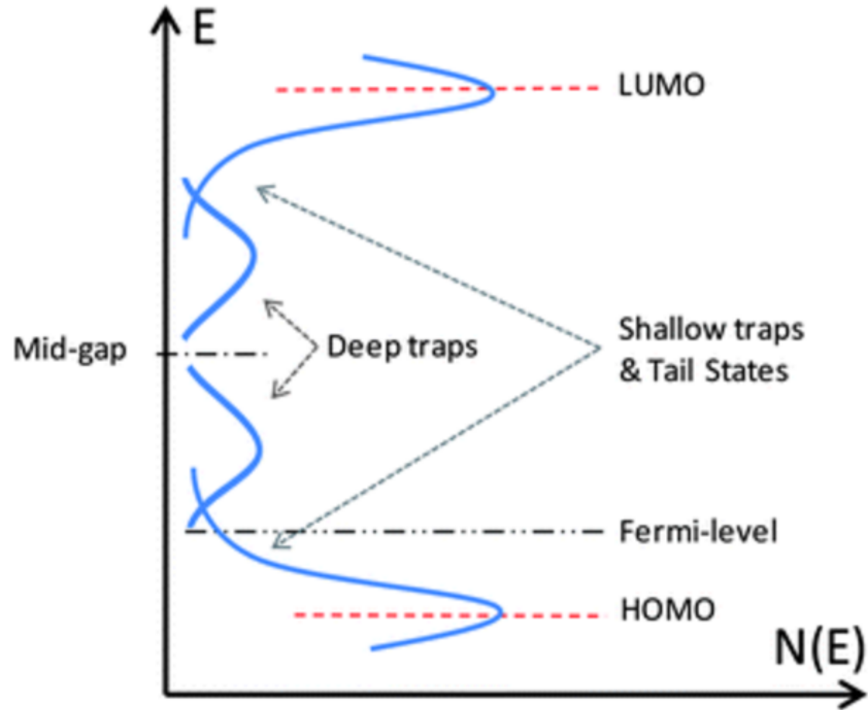

Figure 2.2: Conceptual illustration of density of states in an organic semiconductor [8]

2.2 Status in Most Thoroughly Studied Polymer (P3HT) in OPV

Poly(3-hexyltiophene) (P3HT) is the most thoroughly studied polymer in OPVs. Thus, it is intuitive to ask – what is the status of defect understanding in P3HT? To date, some work has profiled bandgap-residing states in P3HT. Subgap optical absorption has shown the valence band to be Gaussian, broadening of which introduces a distribution of tail-states.[8] Between the valence and Fermi-level, sub-gap optical absorption, thermally stimulated current (TSC), and fractional thermally stimulated current (FTSC) have identified several ionized dopant bands, both exponential and Gaussian in nature.[8] Above the Fermi-level, Gaussian shaped

www.manaraa.com

deep-defect have been reported by admittance spectroscopy (AS), conduction modeling, and TSC. However, no report had profiled deeper into the gap with accurate energetic location to reveal states above the shallow defects.

Thus, a portion of P3HT bandgap had remained uncharacterized. P3HT system has been characterized in this research work by coupling admittance spectroscopy and capacitance-voltage measurements, and two defect bands have been reported.[9] Presence of more defect bands than identified before can be expected as several defects have been theoretically postulated in P3HT as illustrated in figure 2.3.

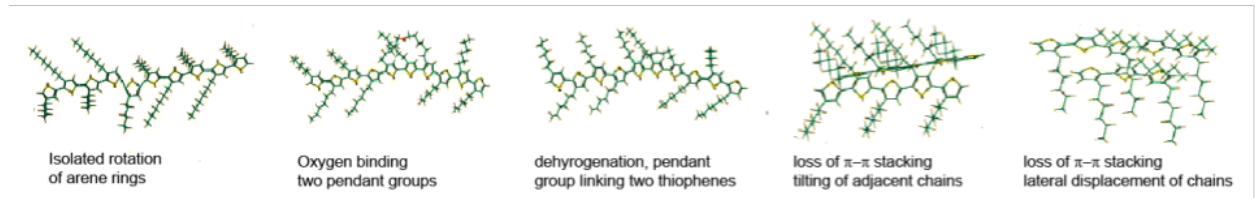

Figure 2.3: Several types of defects theoretically postulated for a 10 monomer chain length P3HT.

2.3 Beyond P3HT

There are several new polymers which have emerged. These materials, though promising in terms of their energy levels and band-gaps, inherit significant amount of defects.[8] Poly[N-9''-hepta-decanyl-2,7-carbazole- *alt* -5,5-(4',7'-di-2-thienyl-2',1',3'-benzothiadiazole)] (PCDTBT) is one such polymer. In contrast to P3HT, PCDTBT has only weak, short-range molecular order. In P3HT, thermal annealing enhances crystallinity, while in PCDTBT it reduces the coherence length of π-π stacking. PCDTBT devices can have efficiencies above 7% and internal quantum efficiencies approaching 100%. Achieving such high efficiencies and efficient charge collection, however, requires active layers that are too thin (~70 nm, due to defective nature of PCDTBT) to absorb more than 70% of the above band-

المنارة للاستشارات

www.manaraa.com

gap light. Thus, optical losses, which account for ~40% of total losses in typical OPVs, are also indirectly linked to defects. In essence, defects have a bearing on all the losses in OPVs, namely, recombination, poor charge carrier mobility, and optical.

Hence, it is imperative to thoroughly identify, characterize and mitigate defects – not only in the canonical P3HT system, but also in the emerging class of defective push-pull polymers. PTB7 (Poly[[4,8-bis[(2-ethylhexyl)oxy]benzo[1,2-b:4,5-b']dithiophene-2,6-diyl][3-fluoro-2-[(2-ethylhexyl) carbonyl] thieno[3,4-b]thiophenediyl]) has been proved promising due to the reports of high efficiency OPV devices using this polymers. PffBT4T-2OD (Poly[(5,6-difluoro-2,1,3-benzothiadiazol-4,7-diyl)-alt-(3,3’’’-di(2-octyldodecyl)-2,2’;5’,2’’;5’’,2’’’-quaterthiophen-5,5’’’-diyl)) has attracted much attention for reports on more than 10% efficient OPVs using this polymer.[6]

2.4 Understanding Defects in Organics is Still in Its Infancy

Following points highlight how understanding of defects in organics is still in its infancy:

- Capacitance characterization as a function of voltage (CV) and frequency (CF) are important techniques used to identify sub-band gap defects in semiconductors. CV theory on defective semiconductors was detailed by Kimerling in 1974 [10] In 1996, Walter et al. proposed the (CF) method to deduce energy distributions of defects in the band gap of a semiconductor by measuring the complex admittance of a junction.[11] CF method requires information about built-in potential and depletion width, which is generally extracted from CV measurements. It was not until 2009 that CV/CF methods were employed on organic bulk-heterojunction films to identify defects.[8]

www.manaraa.com

- The attempt to escape frequency is a characteristic parameter which defines the kinetics of trap occupancy. It is an essential parameter for admittance spectroscopy based defect measurements, Miller- Abraham hopping transport model, Marcus theory of charge transfer, and mobility model in interchain hopping. However, till date, little work has been done to universally quantify it in organic materials. To date, the majority of studies employing this parameter have borrowed values (1012–1014s-1) from inorganics or left the parameter as an unknown.[9] Few measurements on organics have yielded values from 1012 s-1 (pentacene) to theoretically implausible 33.4 s-1 (P3HT) [8]. To get the energetic location of trap states in the bandgap, this parameter needs to be calculated.
- There is lack of study on the physical origin of trap states or defect bands in the bandgap of organic materials. It is important to investigate on their origin and explore ways to minimize these defects changing process parameters to optimize the device performance.

2.5 Objective

This research work aims to develop a greater fundamental understanding of defects in organic photovoltaic (OPV) materials, thin-films and devices, through systematic identification of defects and characterization of their nature, establishing their universalities and specificities across different materials, and exploring approaches for defect mitigation. The field of OPVs has made steady progress in the last few years, mostly via development of better materials in terms of energy levels and band-gaps (though more defective than classic polymer polythiophene), and improved device processing. However, identification, characterization,

المنارة للاستشارات
www.manaraa.com

and mitigation of defects have not yet been thoroughly tackled. Thus, achieving the above aims is critical for the design of next generation efficient and stable OPV cells, and organic electronic devices in general. Specific objectives of the research work are the following:

OBJECTIVE 1: Identify energetic position, distribution and concentration of defects in OPV structures based on several donors and acceptors.

OBJECTIVE 2: Characterize the traps to determine their spatial locations, and their morphological nature.

OBJECTIVE 3: Mitigate the traps by application of external stimuli such as thermal annealing, solvent annealing or vacuum annealing during film growth to optimize device performance. Addition of UV-filter layer in the structure to prevent growth of defects during operation.

2.6 References

1. I. Etxebarria, J. Ajuria and R. Pacios, Org Electron **19**, 34-60 (2015).
2. Z. C. He, C. M. Zhong, X. Huang, W. Y. Wong, H. B. Wu, L. W. Chen, S. J. Su and Y. Cao, Adv Mater **23** (40), 4636-+ (2011).
3. S. E. Shaheen, D. S. Ginley and G. E. Jabbour, Mrs Bull **30** (1), 10-19 (2005).
4. *Organic photovoltaics*. (Wiley-VCH, 2008).
5. G. D. Tayebeh Ameri, Christoph Lungenschmied, Christoph J. Brabec, Energ Environ Sci (2009).
6. Yuhang Liu, Jingbo Zhao, Zhengke Li, Cheng Mu, Wei Ma, Huawei Hu, Kui Jiang, Haoran Lin, Harald Ade & He Yan, Nature Communications 5, Article number: 5293 (2014).

المنارة للاستشارات

www.manaraa.com

7. T. K. K. T. U. Rau, J. Phys. Chem. C **113** (17958–17966) (2009).

8. J. A. Carr and S. Chaudhary, Energ Environ Sci **6** (12), 3414-3438 (2013).

9. T. Muntasir and S. Chaudhary, J. Appl. Phys. 118 (20), 205504 (2015).

10. L. C. Kimerling, J. Appl. Phys. 45, 1839 (1974).

11. T. Walter, R. Herberholz, C. Muller and H. W. Schock, J Appl Phys **80** (8), 4411-4420 (1996).

www.manaraa.com

CHAPTER III

ORGANIC SOLAR CELL FABRICATION & CHARACTERIZATION

3.1 Organic Solar Cell Structure

Organic solar cells consist of 5 layers or thin films, among them the middle layer is a thin film of the polymer where light energy gets absorbed and electron hole generates. On two sides of the polymer layer, one is hole transport layer where generated hole gets transported and other is electron transport layer when electron gets transported. On top and bottom of the structure there are contacts where the connection is made. Detail on how OPV works is already described in section 1.4.

There are two basic structures in organic solar cells – P-i-N and N-i-P structures. P-i-N and N-i-P structures are also known as standard structure and inverted structure, respectively. An example of the P-i-N structure of the device is illustrated in figure 3.1. Associated band-digram is illustrated in figure 3.2. Here, light enters the device through glass substrate and sees the hole transport layer first, then it reaches the photo-active layer. ITO works as the back contact, PEDOT:PSS as the hole transport layer which is p-type and transparent, Pff:PCBM blend as the active layer where pff is the donor material and pcbm is the acceptor material. Finally, Ca/Al works as the top contact.

An example of the inverted structure of the device is illustrated in figure 3.3 and the corresponding band-diagram is shown in figure 3.4. Here, light sees the electron transport layer first, then the photo-active layer. ITO works as the back contact, aluminum doped ZnO as the electron transport layer which is n-type and transperent, Pff:PCBM blend as the active layer and finally MoOx, gold as the top contact.

المنارة للاستشارات
www.manaraa.com

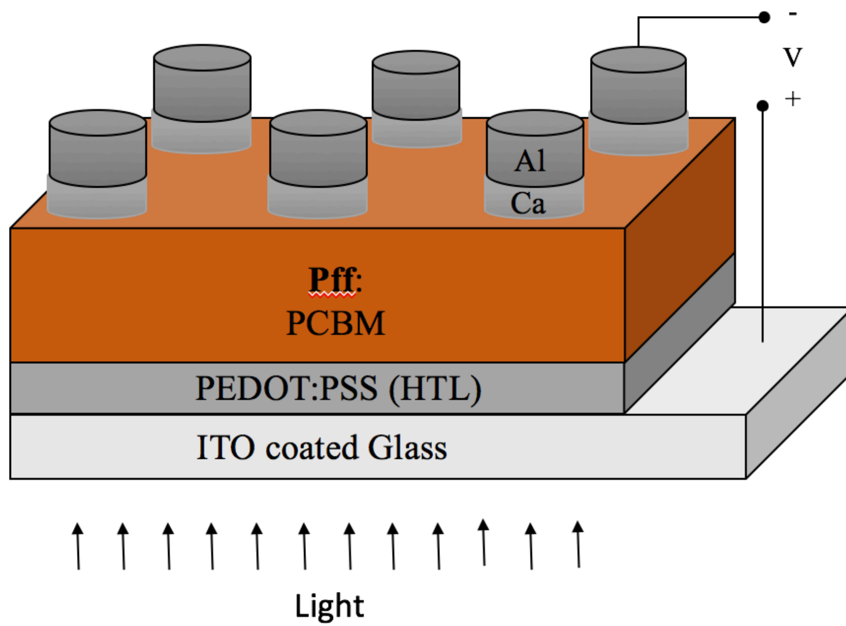

Figure 3.1: An example of organic solar cell on P-i-N structure

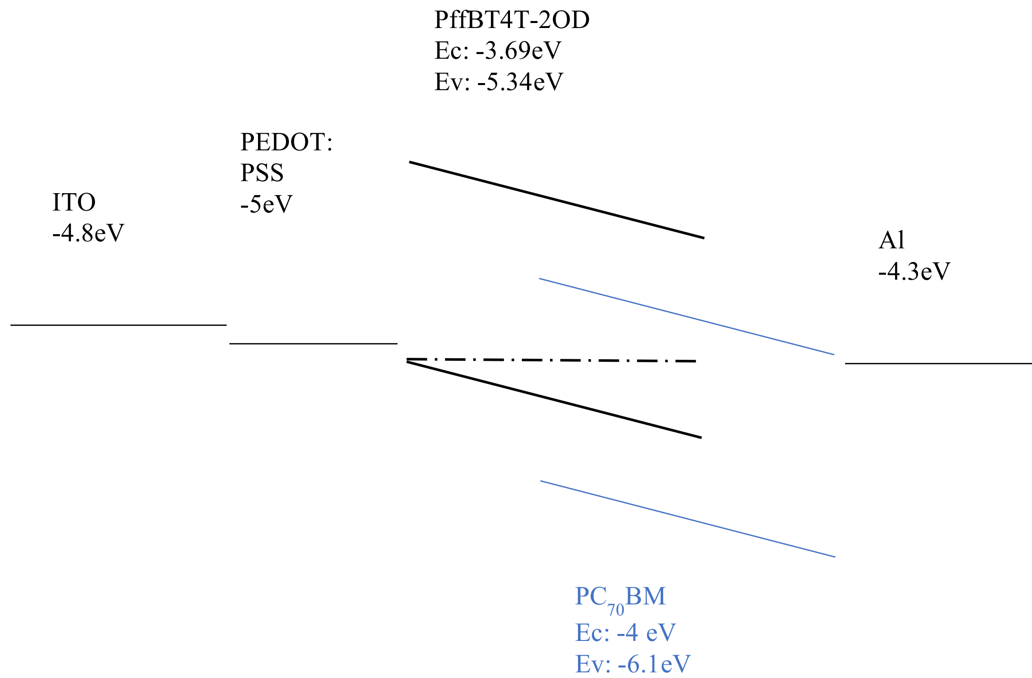

Figure 3.2: Corresponding band-diagram of an organic solar cell on P-i-N structure

المنارة للاستشارات
www.manaraa.com

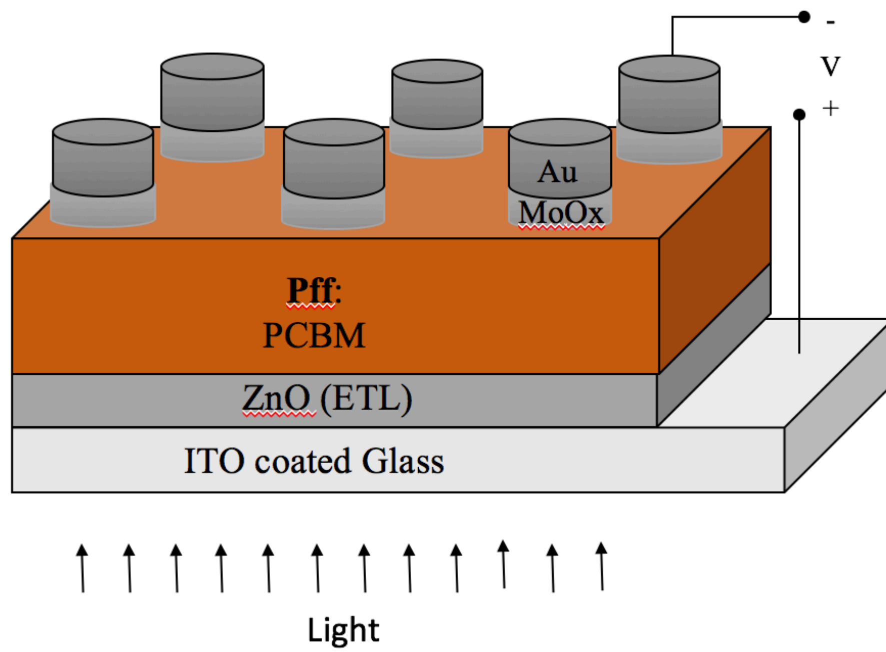

Figure 3.3: An example of organic solar cell on N-i-P structure

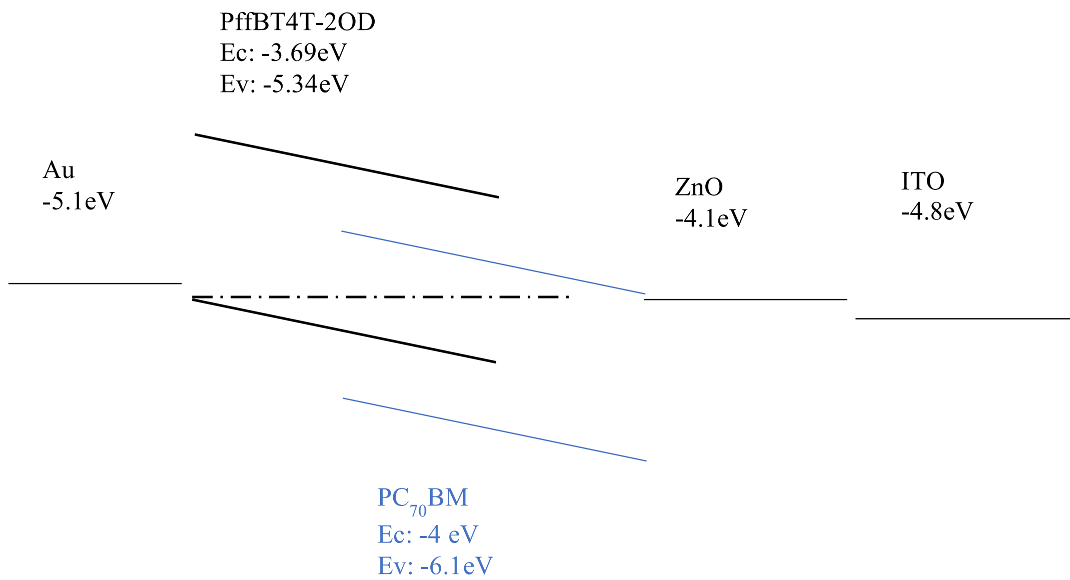

Figure 3.4: Corresponding band-diagram of an organic solar cell on N-i-P structure

المنارة للاستشارات
www.manaraa.com

3.2 Organic Solar Cell Fabrication

Devices are fabricated on ITO coated glass substrates (5-15 Ω/ , Delta Technologies). Substrates are ultrasonicated consecutively in detergent (alconox), de-ionized water, and 2-propanol for 10 minutes. Substrates are blown dry with nitrogen and kept on a hot plate at 130^{0}C for 10 minutes. They are then treated with air plasma. On top of these cleaned substrates hole-transport-layer is deposited in case of P-i-N structure or electron-transport-layer is deposited in case of N-i-P structure. For the case of P-i-N structure, PEDOT:PSS has been mostly used as the hole transport layer. ~40 nm of PEDOT:PSS (VP 4083 from HC Stark) is spin coated on cleaned ITO-coated glass at 4000 rpm for 60 seconds. Samples were then annealed at 140^{0}C for 10 minutes and transferred inside the glove box. For the case of N-i-P structure, ZnO layer is most commonly used in this research work. ZnO layer is deposited using an RF magnetron sputtering system. The process conditions are as follows: power 80W, Ar pressure 5mTorr, substrate temperature 150^{0}C, growth rate 40nm/min, deposition time 45 seconds. Using these conditions 30 nm thick ZnO layer was deposited.

Active-layer solutions were prepared inside the glove box. There are number of polymers as well as small-molecule have been utilized in this research work. Polymers and small-molecules have been bought from 1-materials Inc and CalOS. 1, 2-dichlorobenzene (DCB) and Chlorobenzene (CB) from Sigma-Aldrich were used as the solvent. Donor material and acceptor material are dissolved in the solvent. Different concentration of solutions was utilized. For a specific spin-coating speed, higher the solution concentration thicker is the spin-coated layer. These solutions were stirred at 400 rpm at 50^{0}C-110^{0}C on a hot plate for more than 12 hours and filtered using a 0.22 μm PTFE filter (Sigma-Aldrich) before spin coating on

المنارة للاستشارات
www.manaraa.com

the HTL or ETL coated ITO slides. Spin-coating speed was varied according to the desired active-layer thickness. Higher the spin-coating speed, thinner the deposited layer.

After spin-coating of the active layer, the samples can be dried slower keeping them under a petri-dish. This treatment is known as solvent annealing. Samples can also be kept in a vacuum chamber for some time so that the solvent can leave the film easily. This treatment is known as vacuum annealing. Finally samples are put on a hot plate to make sure that the film is dried and no solvent is left on the film.

Finally, 20 nm of Ca and 100 nm of Al were thermally evaporated sequentially on top of the slow dried (solvent annealed in a petri dish) films as the electrode on the P-i-N structured devices. For the case of N-i-P structured devices, MoOx and, Au or Ag was used as the top contact. Thermal evaporation was done in 10^{-6} mbar vacuum at a rate slower than 0.5 A^o/s for the first layer as high deposition rate can damage the organic film.

3.3 Organic Solar Cell Characterization

Light IV

Solar cell device performance is measured using Light IV measurement. Light has the effect of shifting the solar cell diode IV curve down into the fourth quadrant where power can be extracted from the diode. This phenomenon is illustrated in figure 3.5. The voltage at zero current is the open circuit voltage (V_{oc}). Short-circuit current (I_{sc}) is the current when voltage across the solar cell is zero. Here Jsc is the current density. The point where voltage times current is maximum gives the FF. Fill factor indicates the square-ness of the curve. Power conversion efficiency is the area under this curve. The product of these three parameters gives the PCE.

المنارة للاستشارات
www.manaraa.com

$$PCE = V_{OC}\, J_{SC}\, FF$$

As this curve is not rectangular Fill factor is the correction factor here to get the area under the curve from the product of Voc and Isc. So higher the Voc or Jsc or FF, higher the efficiency of the device.

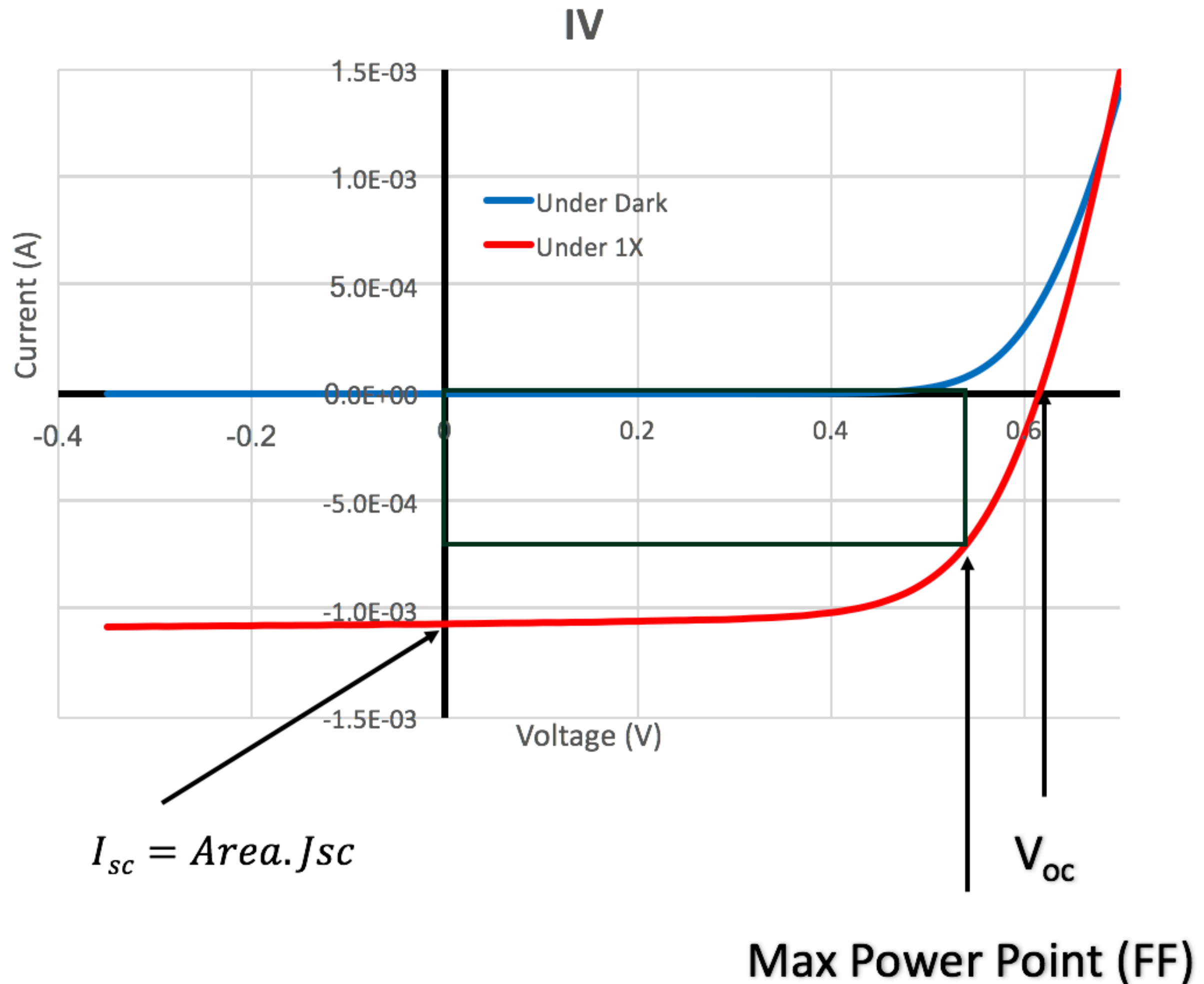

Figure 3.5: Illustration of typical solar cell IV curve and different parameters

المنارة للاستشارات
www.manaraa.com

Dark IV

Dark IV measurements are invaluable in examining different current transport mechanism inside the diode. A typical dark IV curve can be de-convoluted into three parts as illustrated in figure 3.6. The dark current equation is stated below.

$$I = I_{01}\left[exp\left(\frac{qV}{n_1KT}\right) - 1\right] + I_{02}\left[exp\left(\frac{qV}{n_2KT}\right) - 1\right] + \frac{V}{R_{sh}}$$

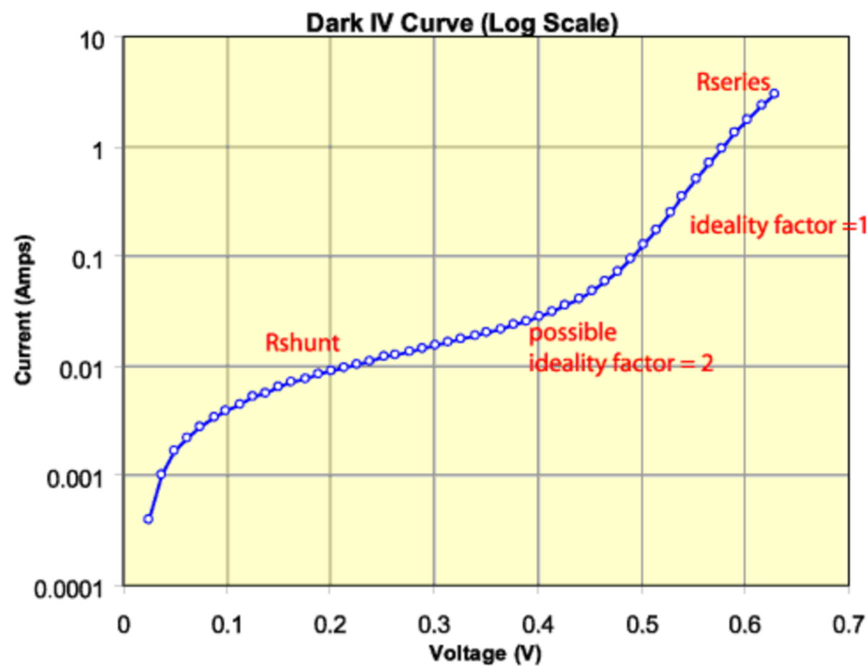

Figure 3.6: Illustration of a typical solar cell dark IV curve

The low voltage regime is the shunt region. This is followed by an exponential region that corresponds to SRH recombination. n1 refers to the diode ideality factor of this region. In ideal case for a single level trap distribution around mid of the energy band gap, n_1 will be 2. However, we see often this number to be lower than two implying multiple level of trap distribution inside the band-gap. Here I_{01} is proportional to SRH recombination which is proportional to Deep defects. At higher voltage we notice another exponential region where n_2

المنارة للاستشارات

www.manaraa.com

refers to the diode ideality factor of that region. In ideal condition the value of n_2 will be close to 1 because in that region the current is dominated by the diffusion of majority charge carrier. At higher voltage the current tends to saturate because of the dominance of series resistance.

Quantum Efficiency (QE)

Another important solar cell performance indicator is quantum efficiency (QE). QE is the ratio of number of carriers collected and number of carriers incident at a particular wavelength. Figure 3.7 shows a typical QE plot. This indicates how efficiently incident light of different wavelengths are being converted to charge carriers and being collected.

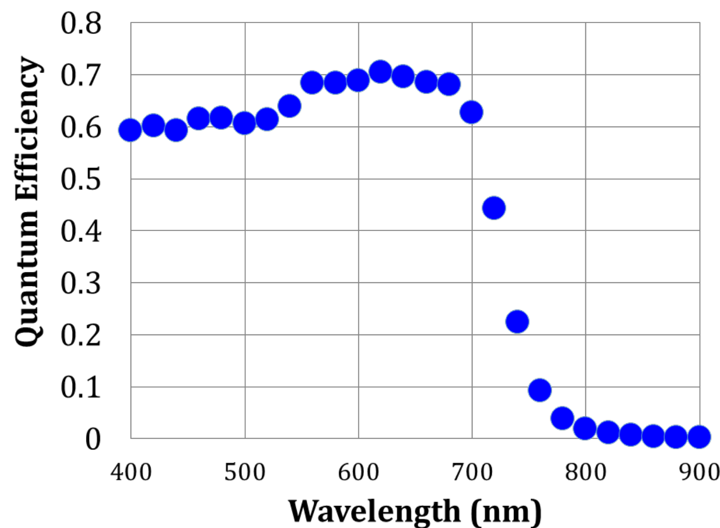

Figure 3.7: Illustration of a typical QE plot

Figure 3.8 shows the schematic diagram of the QE setup utilized in this research work. In QE setup, a mono-chromator is used to generate photon of a particular wavelength by using internal grating structure. A chopper is used to cancel out noise. Through a focusing lenses,

المنارة للاستشارات
www.manaraa.com

filters and mirrors, light of particular wave-length comes to the cell. Pre-amplifier helps in enhancing the low signal obtained from the DUT.

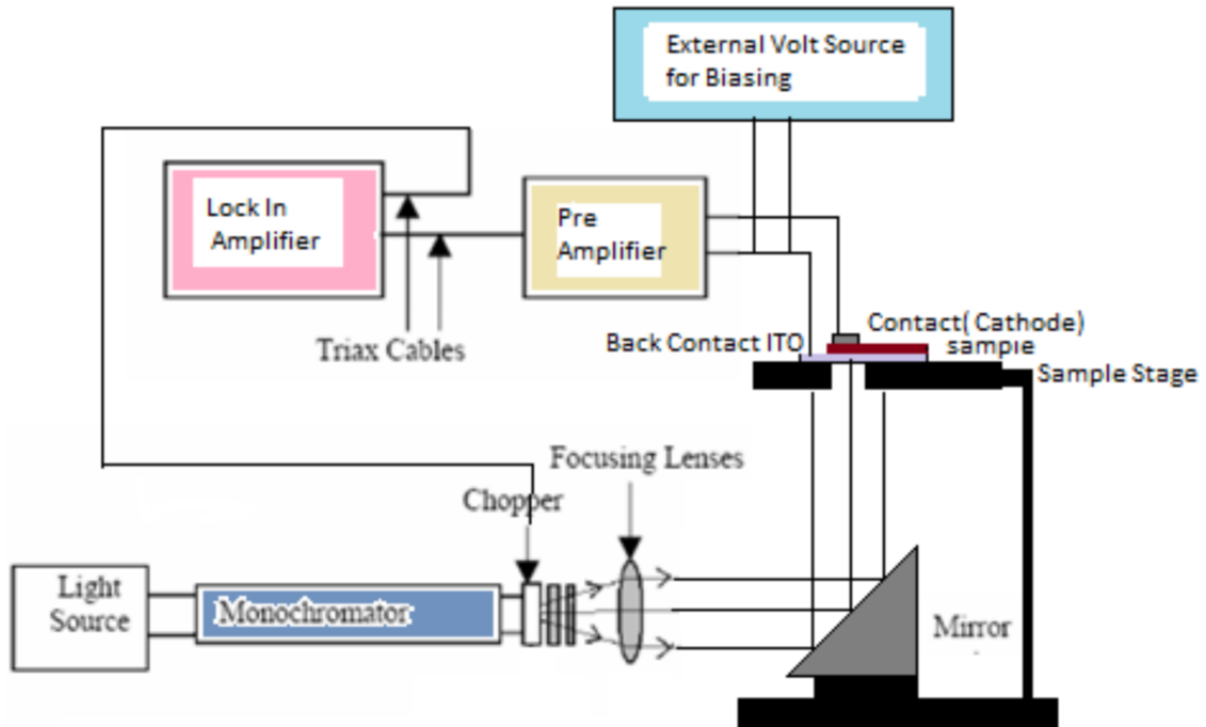

Figure 3.8: Schematic diagram of the QE setup

Capacitance Measurements

The Capacitance-voltage (CV) and capacitance-frequency (CF) measurements utilize the depletion region formed at the metal-semiconductor junction. In CV and CF measurements an AC signal with small modulation voltage is applied to measure the capacitance while a DC bias voltage maintain the junction. A Schottky junction is formed at the metal-organic semiconductor (active layer) interface which is shown in figure 2.[1,2] The band bending depends on the applied bias voltage. When no bias voltage is applied the amount of band bending is qV_{bi} in eV, where q is the charge of an electron and V_{bi} is the built-in voltage. If

المنارة للاستشارات
www.manaraa.com

forward bias (V_F) is applied the band bending is smaller ($qV_{bi} - qV_F$) and for reverse bias the band bending increases ($qV_{bi} + qV_R$).

If the bandgap of the semiconductor resides any trap energy level and if the trap energy level crosses the Fermi energy level, the trap states crossing the Fermi level may charge and discharge following the applied ac signal.[3] If this happens at the depletion region, this charging and discharging will affect the depletion width and consequently the junction capacitance will change.[4] The amount of band bending gives the position of the trap state from the Fermi energy level. So, the trap state position from the HOMO of the organic semiconductor is,

$$E_T = q(V_{bi} - V_{dc}) + E_F.$$

For the case of forward bias V_{dc} is positive and for the case of reverse bias it is negative.

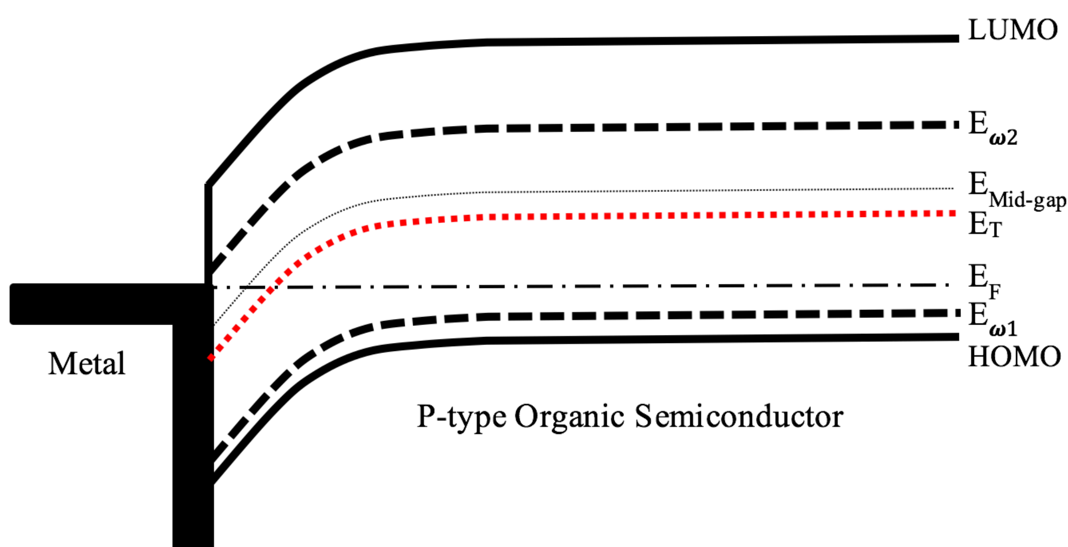

Figure 3.9: Band diagram showing the Schottky junction formed at the metal-active layer interface. Here E_F is the Fermi energy level, $E_{Mid\text{-}gap}$ the midgap energy level, $E_{\omega 1}$ the demarcation energy level at high frequency, $E_{\omega 2}$ the demarcation energy level at low frequency, and E_T is an assumed trap energy level.

المنارة للاستشارات
www.manaraa.com

Charging and discharging mechanism of the trap states also depends on the frequency of the applied ac signal. Dependence of the charging and discharging of the trap states, crossing the Fermi level, on the frequency of the applied AC signal comes from the thermal emission rate of a trap state. In a p-type semiconductor this thermal emission rate is expressed as,

$$e_p = N_v v_{th} \sigma_p exp\left(\frac{-E_A}{K_B T}\right).$$

Here N_V is the effective density of states in the valence band, v_{th} the thermal velocity, σ_p the capture cross-section, E_A the trap activation energy, K_B Boltzmann constant, and T temperature.[3,4] For organic semiconductor the prefactor of the expression ($N_v v_{th} \sigma_p$) is assumed temperature independent and termed as attempt-to-escape frequency (ω_0).[5,6] Linearizing equation (e_p) gives,

$$\ln(e_p) = -\frac{E_A}{K_B T} + \ln(\omega_0).$$

An Arrhenius plot of $\ln(e_p)$ with 1/T appears as a straight line whose slope gives the trap activation energy and intercept gives the attempt-to-escape frequency. This attempt-to-escape frequency and the frequency of the applied AC signal define the demarcation energy which can be quantified by the following expression as derived by Walter et al.

$$E_\omega = K_B T \, ln\left(\frac{\omega_0}{\omega}\right).$$

Here ω is the angular frequency of the applied AC signal ($\omega=2\pi f$).[7] For an AC signal with a specific frequency, the trap states with energy below the demarcation energy can respond. For high enough frequency if the demarcation energy level is below the Fermi level ($E_{\omega 1}$ in figure 3.9), no trap states can respond to the AC signal. As the frequency of the signal

المنارة للاستشارات
www.manaraa.com

is lowered the demarcation energy level goes above the Fermi level ($E_{\omega 2}$ in figure 3.9), then the trap levels between the demarcation energy level and the Femi level can respond to the applied signal and consequently the change in the capacitance can be detected. Using this method the upper limit of the detection is the midgap energy level, that is only the trap states between the midgap energy and the Fermi level can be detected.[7] Taking the derivative of the CF measurement, defect distribution at an energy E_{ω} can be determined by,[7]

$$N_T(E_\omega) = -\frac{V_{bi}}{qW}\frac{dC}{d\omega}\frac{\omega}{K_B T}.$$

Here C is the capacitance of the junction, and W is the depletion width. Semiconductor doping and built-in voltage of a one-sided junction formed at the metal- semiconductor interface can be found from CV utilizing the well-known Mott-Schottky (MS) equation,[8]

$$\frac{1}{C^2} = \frac{2}{A^2 q\varepsilon N_A}(V_{bi} - V_{dc}).$$

Here V_{dc} is the applied bias, N_A doping of the semiconductor, ε the dielectric constant of the semiconductor and A is the area of the contact. From the plot of $1/C^2$ vs. V_{dc}, the slope gives the doping density and the intercept gives built-in voltage. Solving Gauss's law for the charge at the depletion edge the classic profiler equation is found,[4]

$$N_A(x) = \frac{C^3}{q\varepsilon A^2}\frac{dV_{dc}}{dC}$$

Here x is the spatial distance from the junction. As this distance depends on applied bias, plotting N_A with V_{dc} can indicate the distribution of defects as trap states are pulled to the Fermi level.

المنارة للاستشارات

www.manaraa.com

Impedance Spectroscopy

Impedance Spectroscopy (IS) is a well-known technique to investigate the charge transport kinetics in solid-state devices which utilizes the Nyquist plot ($-Z_{imaginary}$ vs. Z_{real}).[9-16] In this method, like CV and CF, an AC signal with small modulation voltage is applied in addition to DC bias. Frequency of the AC signal is varied in a wide range and obtained impedance is recorded. When the negative of the imaginary part of the impedance is plotted with the real part of the impedance, one or more than one semicircle is obtained. The peak of the semicircle at lower frequency range is identified, and the inverse of the corresponding frequency (f_n) gives the minority carrier lifetime (τ_n=1/f_n). At the higher frequency end of this semicircle, an almost straight line is obtained. The point where this straight line crosses the semicircle is identified and the inverse of the corresponding frequency (f_d) gives the transit time (τ_d=1/f_d), which is also known as the electron diffusion time. The electron diffusion coefficient (D_n) and the electron mobility is obtained subsequently by,[10]

$$D_n = \frac{L^2}{\tau_d}.$$

$$\mu_n = \frac{eD_n}{K_B T}.$$

Here L is the active layer thickness.

3.4 References

1. T. Muntasir and S. Chaudhary, J. Appl. Phys. 118 (20), 205504 (2015).

2. T. Muntasir and S. Chaudhary, J. Appl. Phys. **119**, 025501 (2016).

3. L. C. Kimerling, J Appl Phys (1974).

المنارة للاستشارات

www.manaraa.com

4. P. Z. J. Heath, *Advanced Characterization Techniques for Thin Film Solar Cells*. (2011).
5. J. A. Carr and S. Chaudhary, Energ Environ Sci **6** (12), 3414-3438 (2013).
6. S. S. Hegedus and E. A. Fagen, J Appl Phys **71** (12), 5941-5951 (1992).
7. T. Walter, R. Herberholz, C. Muller and H. W. Schock, J Appl Phys **80** (8), 4411-4420 (1996).
8. S. M. Sze, *Semiconductor Devices Physics and Technology*. (John Wiley & Sons Inc., New York, 1985).
9. A. Kokil, K. Yang and J. Kumar, J Polym Sci Pol Phys **50** (15), 1130-1144 (2012).
10. G. Garcia-Belmonte, A. Munar, E. M. Barea, J. Bisquert, I. Ugarte and R. Pacios, Org Electron **9** (5), 847-851 (2008).
11. J. Bisquert, L. Bertoluzzi, I. Mora-Sero and G. Garcia-Belmonte, J Phys Chem C **118** (33), 18983-18991 (2014).
12. G. Garcia-Belmonte, P. P. Boix, J. Bisquert, M. Sessolo and H. J. Bolink, Sol Energ Mat Sol C **94** (2), 366-375 (2010).
13. B. J. Leever, C. A. Bailey, T. J. Marks, M. C. Hersam and M. F. Durstock, Adv Energy Mater **2** (1), 120-128 (2012).
14. G. Perrier, R. de Bettignies, S. Berson, N. Lemaitre and S. Guillerez, Sol Energ Mat Sol C **101**, 210-216 (2012).
15. J. Bisquert, J Phys Chem B **106** (2), 325-333 (2002).

المنارة للاستشارات
www.manaraa.com

CHAPTER IV

UNDERSTANDING DEFECT DISTRIBUTION IN POLYTHIOPHENES VIA COMPARISON OF REGIOREGULAR AND REGIORANDOM SPECIES

Organic photovoltaics (OPVs) are regarded promising for solar-electric conversion with steadily improving power conversion efficiencies. For further progress, it is crucial to understand and mitigate defect states (traps) residing in the band-gap of OPV materials. In this work, using capacitance measurements, we analyzed two major bands in the density of states (DOS) energy spectra of defects in poly(3-hexylthiophene) (P3HT); regio-regular and regio-random species of P3HT were compared to elucidate the role of morphological disorder. To accurately interpret the obtained DOS profile, trap emission prefactor and activation energy were extracted from temperature dependent capacitance-frequency (CF) measurements, while doping, Fermi energy, built-in voltage, and energy levels of the defects were extracted from capacitance-voltage (CV) measurements. We identified that the lower energy band - misinterpreted in literature as a defect distribution - stems from free carrier response. The higher energy defect distribution band for regio-random P3HT was an order of magnitude higher than region-regular P3HT, thus stemming from morphological disorder. Impedance spectroscopy was also employed for further comparison of the two P3HT species.

4.1 Introduction

Due to the feasibility of low-temperature and solution-based fabrication, organic photovoltaics (OPVs) are promising for large scale roll-to-roll production and economical solar-electric conversion.[1] Extensive research works on OPVs have been published over the

www.manaraa.com

last 30 years; efficiency and stability are still considered as the major directions for improvement.[1,2] Although the power conversion efficiency for single-junction bulk-heterojunction OPV devices has exceeded 10%, its Schockley-Queisser limit has been calculated as 23%.[3] Thus, there is scope for further research on better energy level alignment between donor-acceptor materials, adequate light trapping, enhanced exciton dissociation, reduction in recombination, and improvement in carrier mobilities.[4-8] Understanding fundamental physical properties also remains important; traps or defect states residing in the band-gap of OPV materials are one of the important physical paramters.[9] Defects are known to affect the physical operation of OPVs in multiple ways.[9] Defects introduce recombination centers leading to loss of free carriers, and detrimentally affect properties like carrier transport, charge separation, and exciton diffusion lengths; all these factors deteriorate the efficiency and stability of OPV devices.[9-13]

A common method to probe defects in OPVs is the determination of trap density of states (tDOS) profile throughout the band-gap of OPV active-layer materials. There are many reports on tDOS profiles.[12,14-18] Most reports are on the classic OPV material system of regio-regular-poly(3-hexylthiophene):phenyl-C61-butyric acid methyl ester (RR-P3HT:PCBM). Boix *et al*. reported a defect band centered at 0.38 eV above the highest occupied molecular orbital (HOMO) level of P3HT.[14] Nalwa *et al*. reported a band between 0.32 eV and 0.38 eV above the HOMO level of P3HT.[17] Ecker *et al*. reported two bands with unspecified energy levels[15] and attributed the first band to traps in the polymer and the second band to interfacial traps between the active-layer and the hole-transport layer. MacKenzie *et al*. did not report any Gaussian band but rather an exponential tail.[16] Recently, Carr *et al.* reported a defect band at 0.33 eV above the HOMO of P3HT and another band 0.36

www.manaraa.com

eV deeper in the tDOS energy spectra of RR-P3HT:PCBM.[19] For determination of accurate energy levels in tDOS profiles, knowledge of maximum trap emission rate is required.[20] There are anomalies in the values of maximum trap emission rate used in previous reports.[9] Most reports used the value of the maximum trap emission rate same as that in inorganics (10^{11} – 10^{13} Hz) or left it as unknown. [13,14,21-23] In addition to the variations in reports discussed above, interpretation of the physical origins of obtained bands in tDOS profiles are also rather lacking in the literature. Thus, further research is needed to accurately obtain and interpret tDOS energy spectra.

Comparing the tDOS spectra of Regio-random- (RRa-) and RR-P3HT creates an opportunity to elucidate the physical understanding of trap distributions. There is no report in the literature on the comparison of tDOS profiles of these two species of P3HT. It is only qualitatively known that RRa-P3HT is more disordered than RR-P3HT; structures of the two species are illustrated in figure 4.1. Reports on RRa-P3HT have mainly focused on device performance. It was shown that a ternary system, prepared by adding RRa-P3HT into RR-P3HT:PCBM blend, improved the morphology by reducing unwanted aggregates.[24] A study on the comparison of photoexcitations in RR-P3HT and RRa-P3HT films reported a moderately strong photoluminescence band, long-lived triplet excitons, and some intrachain charged polarons in RRa-P3HT.[25] For RR-P3HT, it was reported that the long-lived photoexcitations are interchain excitons and delocalized polarons in the lamellae. Another study on the comparison of photocarrier transport in RR-P3HT and RRa-P3HT showed that mobility in RR-P3HT is one order of magnitude larger than RRa-P3HT.[26] A study on the photogenerated charge dynamics in RR-P3HT:PCBM and RRa-P3HT:PCBM showed that the charge transfer excitons are photogenerated much faster in RRa-P3HT blends due to smaller

www.manaraa.com

domain size but exciton dissociation is poor, leading to poor power conversion efficiencies.[27]

In this work, we report the tDOS energy spectra of P3HT with energetic location of trap states determined utilizing the measured (rather than borrowed from inorganics) maximum trap emission rate. The tDOS energy spectra were obtained using the model of Walter *et al*.[20] We probed both RR and RRa-P3HT and their blends with PCBM to investigate the physical origins of the obtained trap distributions. For all the active-layers investigated (RR-P3HT, RRa-P3HT, RR-P3HT:PCBM, and RRa-P3HT:PCBM), the maximum trap emission rate was determined utilizing temperature dependent CF measurements to get the accurate energy level of the distributions in tDOS profiles. Two Gaussian distributions were obtained in the tDOS energy spectra of all four samples. The lower energy band was found to be stemming from free-carrier response, while in literature is has been reported as a defect distribution. The higher energy band was found to be stemming from morphological disorder; its magnitude in RRa-P3HT was one order of magnitude higher than RR-P3HT. In high frequency measurements, we identified free carrier freeze-out which happens when the carriers in the undepleted bulk material have no time to shift in and out of the depletion edge in response to the applied signal.[28] We also investigated electronic properties of both RR- and RRa-P3HT blends utilizing impedance spectroscopy.

For all devices studied in this report, we used the device structure (ITO)/PEDOT:PSS/active-layer/Ca/Al as shown in Figure 4.1. Four types of active-layers were investigated: RR-P3HT:PCBM, RRa-P3HT:PCBM, RR-P3HT, and RRa-P3HT.

المنارة للاستشارات
www.manaraa.com

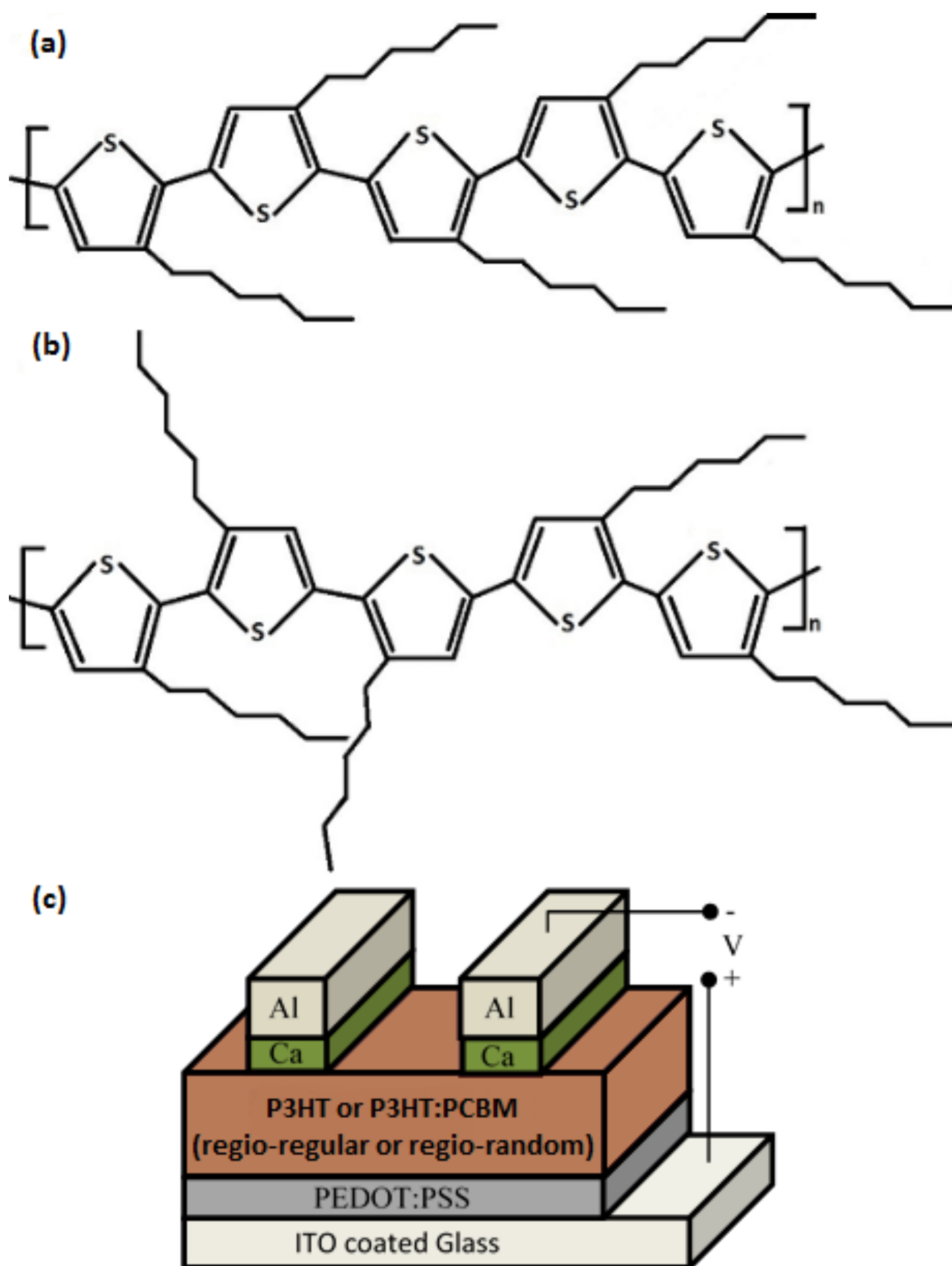

Figure 4.1: (a) Structure of RR-P3HT, (b) Structure of RRa-P3HT, and (c) Schematic of an organic photovoltaic device.

المنارة للاستشارات
www.manaraa.com

4.2 Results & Discussions

To probe trap states residing deep into the band-gap of the material under investigation, it is required to perform capacitance measurements up to as low frequency as possible. However, at low frequency, OPV data gets dominated by noise and AC impedance gets high, which can be a limiting factor for the equipment in use.[44] To reduce noise and get better quality capacitance data, thick films (>300nm) of the active-layers (thicker than typically employed for high efficiency OPV devices) were investigated. These thick films enabled capacitance measurements up to 10 mHz. For accurate interpretation of the capacitance data, we calculated geometric capacitance (C_{geo}) and dielectric constant (ε). Geometric capacitance was calculated under reversed bias that ensured complete depletion, thickness (d) of the active-layers was measured using SEM, and dielectric constant was calculated utilizing the equation, $C_{geo}=\varepsilon A/d$, where A is the area of the electrode. For both RR:P3HT and RRa:P3HT, dielectric constant was calculated as 3 and 3.5 for neat polymer and polymer:fullerene active-layers, respectively.

Maximum trap emission rate, defined by ATEF, is needed to get the accurate energetic location of trap states. We measured the ATEF of all four samples using temperature dependent CF measurements. As discussed in the theory section, ATEF can be obtained from the intercept of the Arrhenius plot of $\ln(e_p)$ versus 1/T. This measurement was conducted in a cryostat. Inside the cryostat, vacuum was maintained and temperature was varied from 325K to 100K. P3HT active-layers are known to dedope in vacuum.[45] As the devices dedope, the measured capacitance decreases with time. To ensure accurate measurement, stable capacitance is required over the duration of the measurement. To ensure stable capacitance, devices were kept

المنارة للاستشارات
www.manaraa.com

at 325K in vacuum for 24 hours before measuring. Capacitance versus time plots for four devices are shown in figure 4.2.

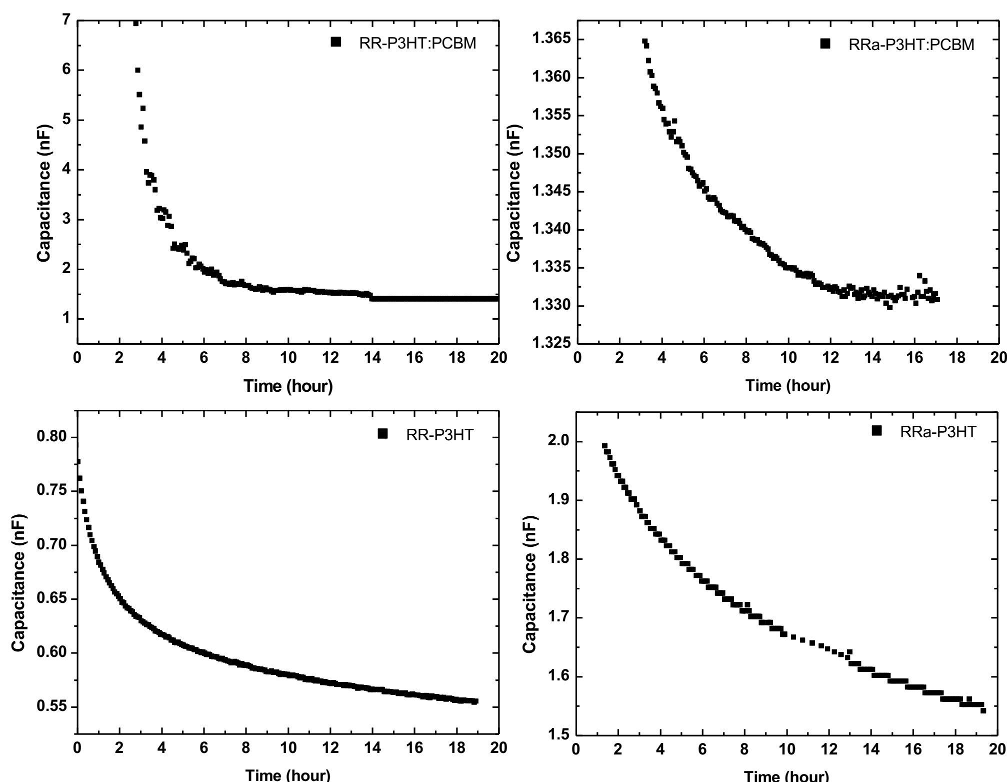

Figure 4.2: Illustration of dedoping over time in vacuum and dark at 325K.

When capacitance (C) is plotted with frequency (F), a step up in capacitance from higher frequency to lower frequency is found.[9] The frequency at which the step occurs defines the demarcation where the corresponding trap responds. The differential –F dC/dF plotted with frequency gives a peak at this step. This peak coincides with the emission rate (e_p) of the responding trap states. –F dC/dF vs. F was plotted at different temperatures for all four devices, as shown in figure 4.3. For RRa-P3HT, the band is broader than RR-P3HT, which is further discussed later in this section.

www.manaraa.com

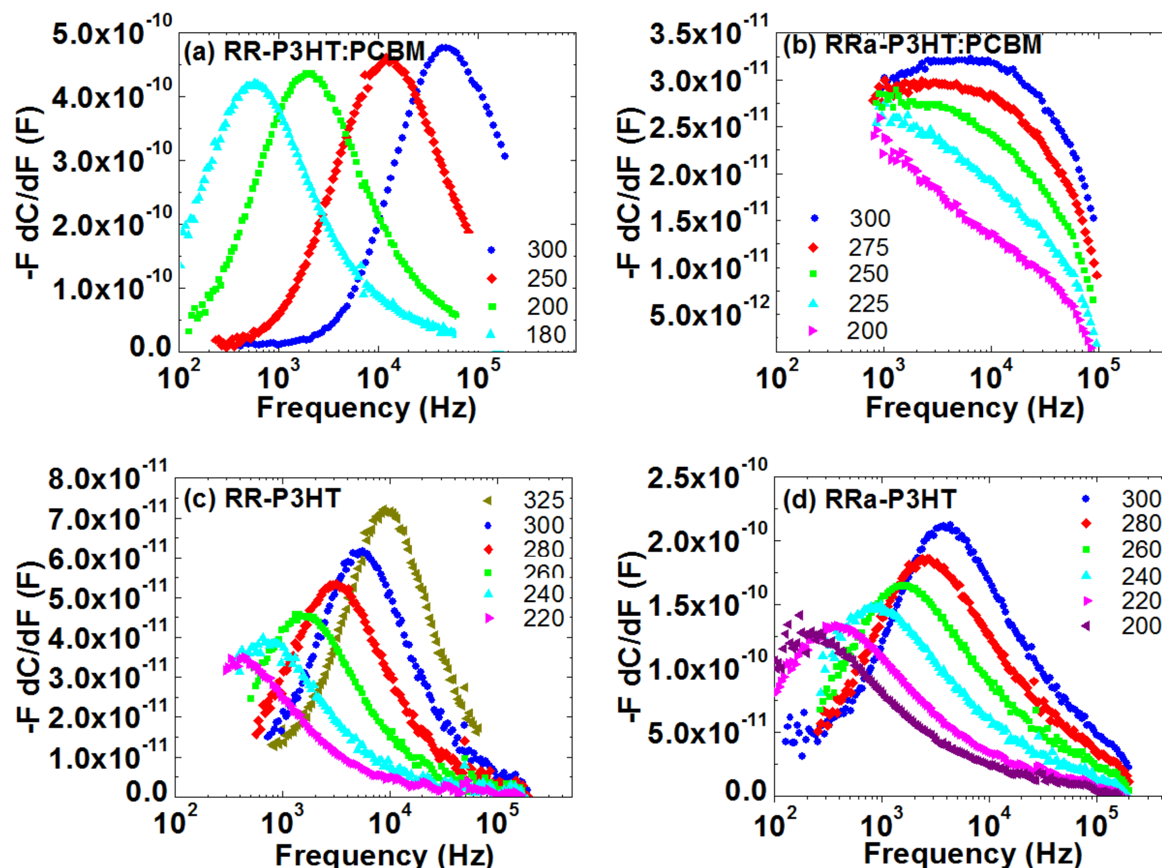

Figure 4.3: -F dC/dF plotted with frequency at different temperatures for (a) RR-P3HT:PCBM, (b) RRa-P3HT:PCBM, (c) RR-P3HT and (d) RRa-P3HT. The peak corresponds to the trap emission peak.

The obtained straight line plotting $\ln(e_p)$ versus 1/T is shown in figure 4.4. Calculated activation energy and ATEF are tabulated in table I. ATEF is highest for RR-P3HT:PCBM and lower by one to two order of magnitudes for the other devices. Using these values of ATEF, tDOS measured at different temperatures are plotted in figure 4.5. Overlap of tDOS energy spectra at different temperatures validates the values of the measured ATEF.

المنارة للاستشارات
www.manaraa.com

Table 4.1: Obtained activation energy (E_a) and ATEF from temperature dependent CF measurements

	RR-P3HT:PCBM	*RRa-P3HT:PCBM*	*RR-P3HT*	*RRa-P3HT*
E_a (eV)	0.225	0.175	0.20	0.17
ATEF (Hz)	4×10^8	5×10^6	1.2×10^7	3.7×10^6

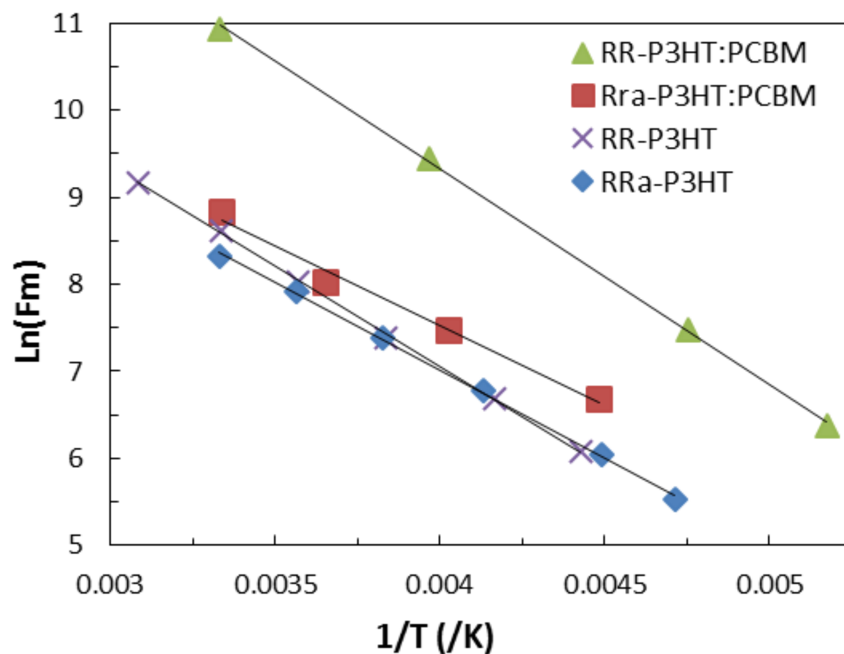

Figure 4.4: Arrhenius plot of emission peak vs. 1/T for RR-P3HT:PCBM, RRa-P3HT:PCBM, RR-P3HT and RRa-P3HT. The lines are showing linear fit.

Selection of frequency of the applied AC signal is important in CV measurements. Demarcation energy level of the corresponding frequency should be near Fermi energy to find doping of the active-layer. Higher frequency gives the demarcation level below Fermi level, so a portion of carriers may freeze. Lower frequency gives the demarcation level above the Fermi level, thus including traps states and their density in measured doping. Considering the measured ATEF, 200KHz was determined for RR-P3HT:PCBM and 200Hz for the other three types of devices as the frequency of the applied AC signal. Another important consideration

المنارة للاستشارات
www.manaraa.com

for reliable CV measurements is selection of parallel or series model of the equivalent circuit for small-signal measurement.[18,44] These models simplify the equivalent circuit of small-signal measurement so that we do not need to solve complex equations to get capacitance from LCR meter.[18] In general, series model is used for high frequency measurements and parallel model is used for low frequency measurements.[43-45] Another criterion is that series model is appropriate when the impedance value is less than 1 KΩ and parallel model is appropriate used when the impedance value is more than 100 KΩ.[44] Both models can be used when the impedance value is in between 1 KΩ to 100 KΩ.[44] Thus, we monitored impedance value and selected models accordingly. Data points with dissipation factor (D) less than 10 were considered to ensure accuracy of the calculated parameters.

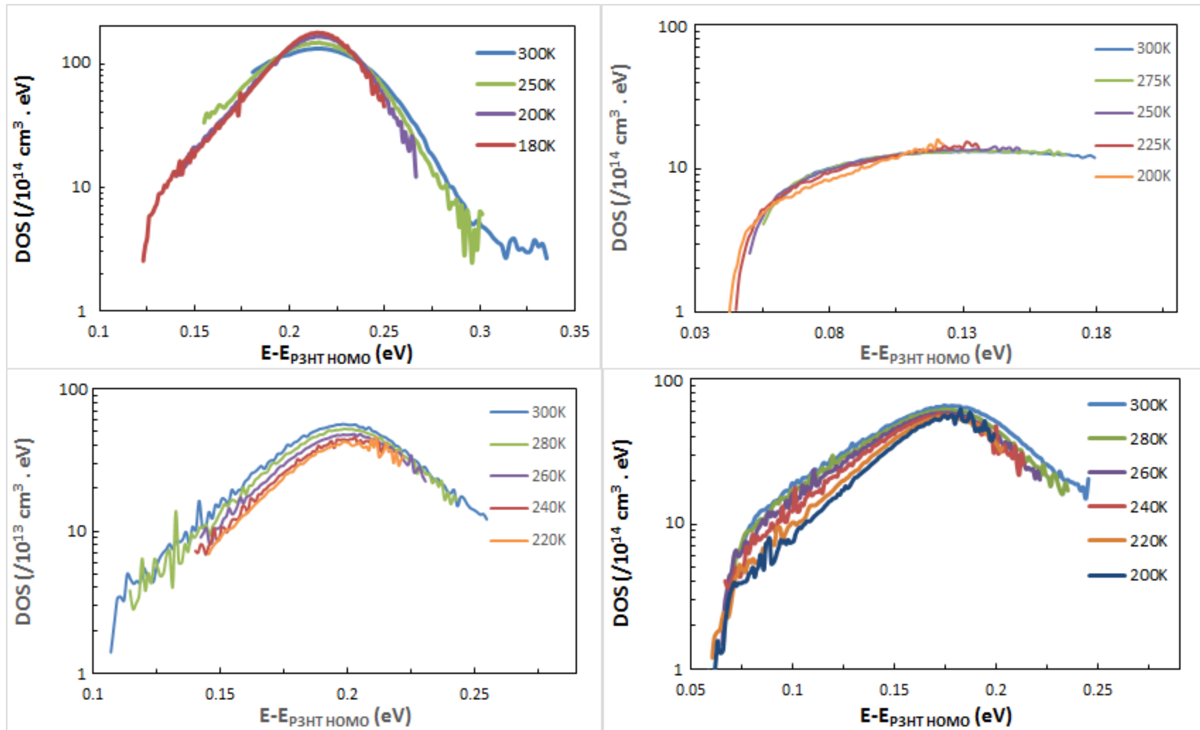

Figure 4.5: Illustration of the overlap of tDOS energy spectra using measured ATEF at different temperatures. Top left: RR-P3HT:PCBM, top right: RRa-P3HT:PCBM, bottom left: RR-P3HT, and bottom right: RRa-P3HT.

www.manaraa.com

Doping of the polymer and the built-in voltage at the metal-polymer junction were calculated utilizing the Mott-Schottky relation. Figure 4.6 illustrates the Mott-Schottky relation where inverse of the capacitance squared is plotted against the applied bias. Fermi energy is calculated from extracted doping concentration. Resulting values are tabulated in table II. We found that RRa active-layers were doped more than the RR counterparts, and neat-polymer devices were doped more than the blends.

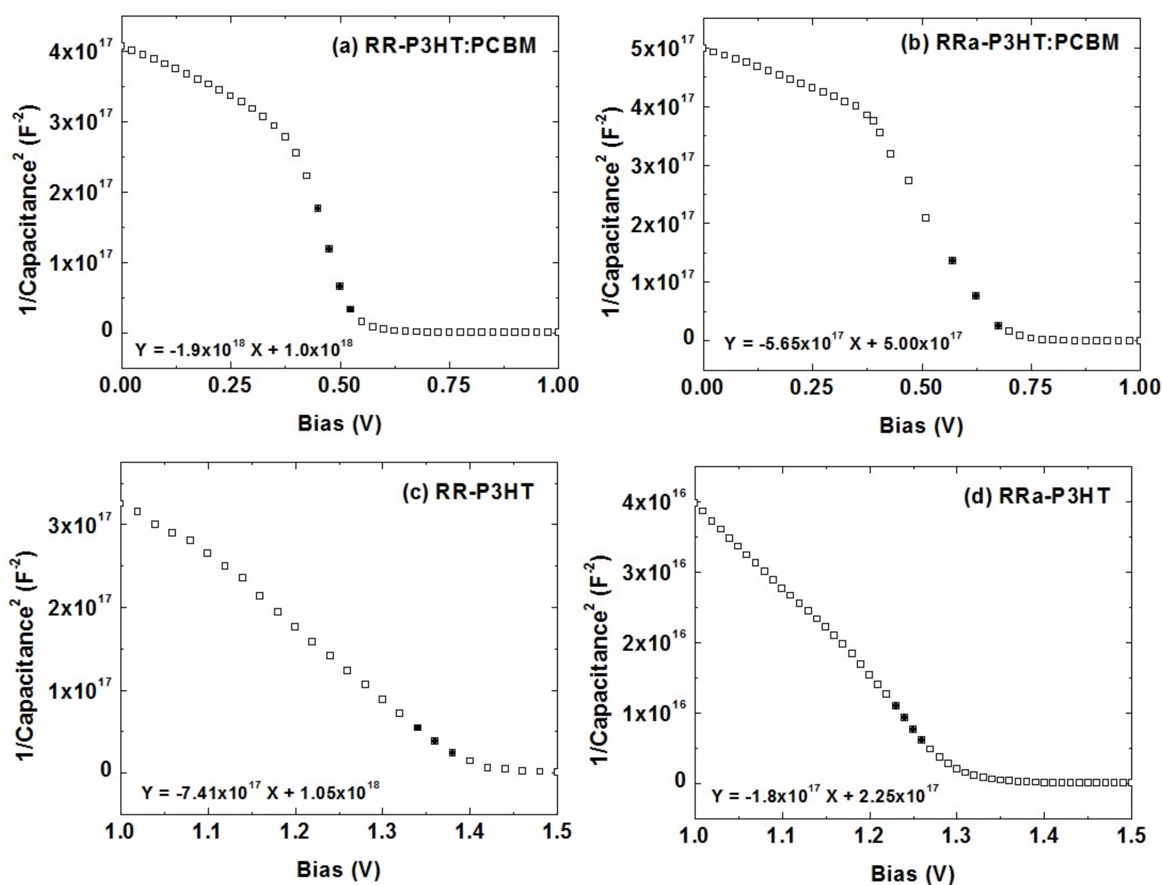

Figure 4.6: Inverse of capacitance squared is plotted with applied bias (Mott-Schottky relation) for (a) RR-P3HT:PCBM, (b) RRa-P3HT:PCBM, (c) RR-P3HT and (d) RRa-P3HT. The black data points indicate the portion from where slope and intercept were calculated. The equation that gave the linear fit of the selected portion is also included.

المنارة للاستشارات
www.manaraa.com

Table 4.2: Doping, built-in voltage and Fermi energy extracted from CV measurements.

	RR-P3HT:PCBM	*RRa-P3HT:PCBM*	*RR-P3HT*	*RRa-P3HT*
Doping (/cm^3)	1.2×10^{15}	5.8×10^{15}	4.4×10^{15}	1.6×10^{16}
Built-in voltage (V)	0.52	0.75	1.4	1.3
Fermi energy (eV)	0.23	0.18	0.20	0.17

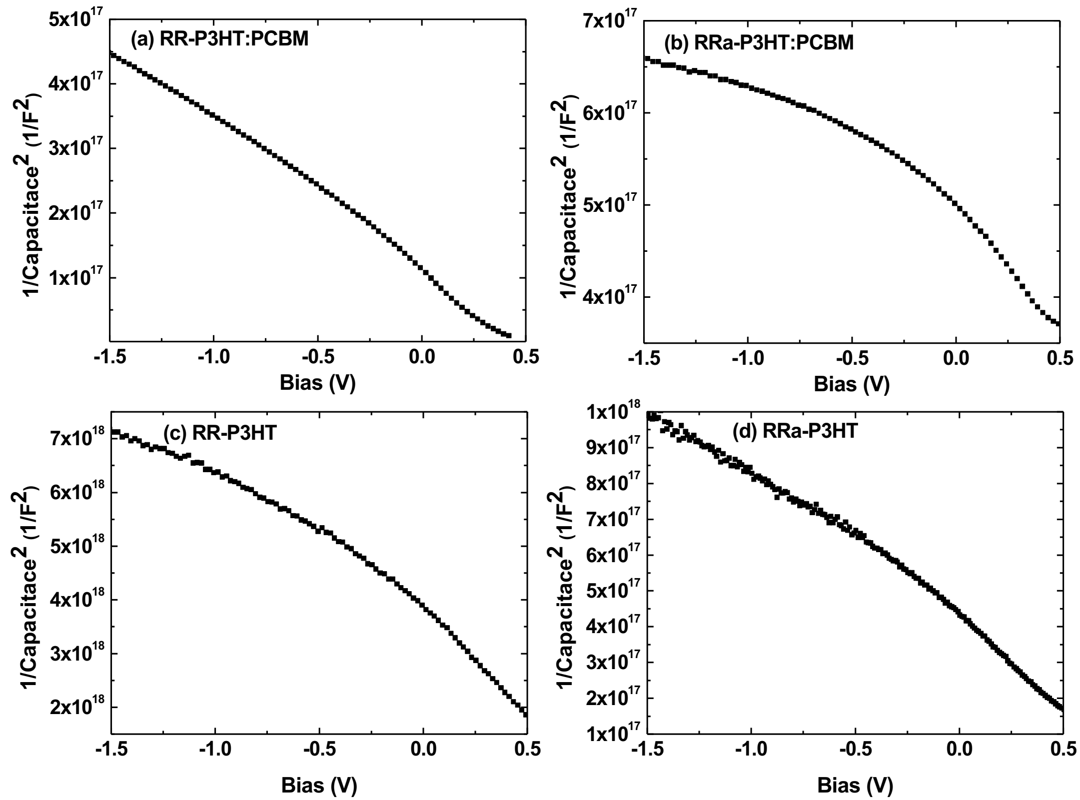

Figure 4.7: Illustration of rolling slope in Mott-Schottky plot at low frequency. Top left: RR-P3HT:PCBM with 200Hz as the frequency of AC signal, top right: RRa-P3HT:PCBM with 100Hz, bottom left: RR-P3HT with 100Hz, and bottom right: RRa-P3HT with 100Hz.

Mott-Schottky relation from low frequency CV measurements shows a rolling slope with increasing reverse bias as illustrated in figure 4.7. At the low frequency (<200Hz) employed, the demarcation energy level is further toward the midgap from the Fermi energy level. In this case, as more reverse bias is applied, more trap states are brought at Fermi level.

المنارة للاستشارات
www.manaraa.com

As more trap states cross the Fermi level, they respond and consequently a rolling slope is obtained. This is a clear indication of the existence of deep traps in the band-gap. Profiler equation was utilized to plot defect density as a function of reverse bias, as shown in figure 4.8, and the plot is referred as depth profile. A minima is found in this plot near the built-in voltage; the corresponding bias voltage at this minima represents the flat band voltage. At flat band voltage, no states cross the Fermi energy, so minimum distribution of defect density is obtained. There is charge injection at forward bias more than the built-in voltage, and trap states start to cross the Fermi energy level at reverse bias less than the built-in voltage. For all four devices, as more reverse bias is applied, there is an increase in the defect density after the flat band voltage. This increase corresponds to the inclusion of defects. Eventually, there is a gradual decrease in the rate of increase; this occurs at the peak of a Gaussian distribution of defects. When the derivative of this defect density with respect to applied bias is plotted with reverse bias, this peak becomes more apparent as shown in figure 4.9. The value of applied bias where the Gaussian distribution peaks was identified; energy levels of the corresponding defect states were calculated and tabulated in table 4.3.

Table 4.3: Calculated position of the peak of the Gaussian distribution of defect from depth profile.

	RR-P3HT:PCBM	*RRa-P3HT:PCBM*	*RR-P3HT*	*RRa-P3HT*
Major defect peak (V)	0.3	0.45	1.1	1.08
Energy level from HOMO (eV) $q(V_{bi}-V_{dc})+E_F$	0.45 (0.52-0.3+0.23)	0.48 (0.75-0.45+0.18)	0.50 (1.4-1.1+0.2)	0.39 (1.3-1.08+0.17)

المنارة للاستشارات
www.manaraa.com

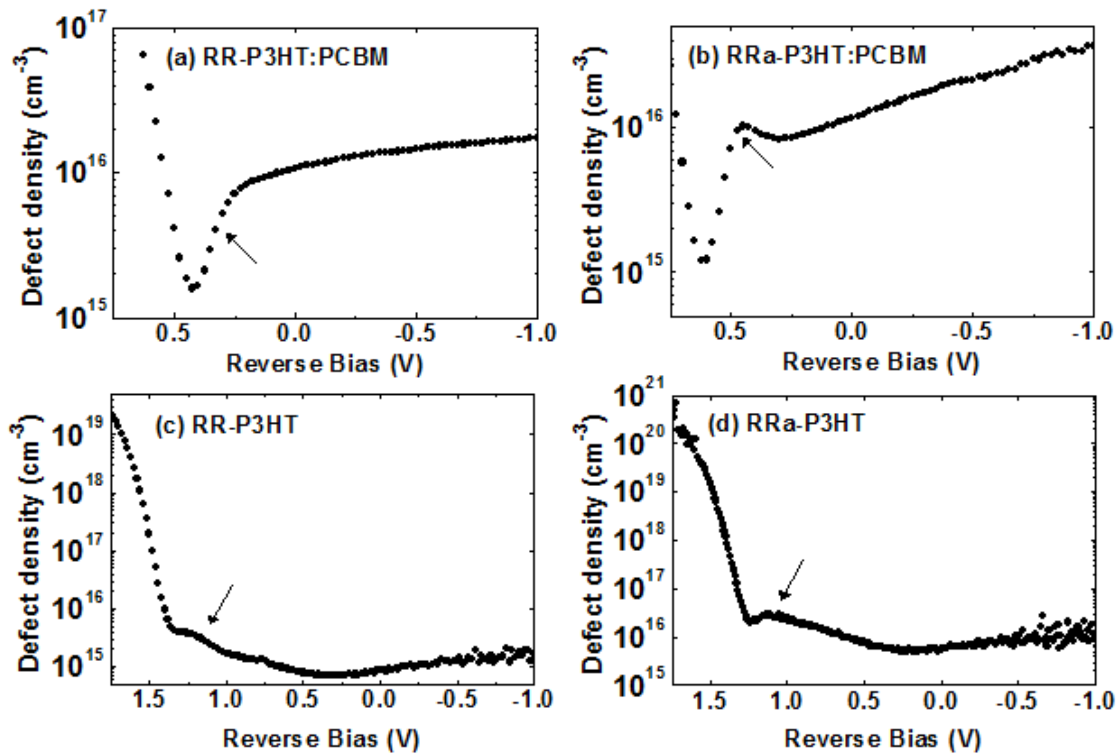

Figure 4.8: Defect density measured using profiler equation are plotted with reverse bias for (a) RR-P3HT:PCBM, (b) RRa-P3HT:PCBM, (c) RR-P3HT and (d) RRa-P3HT. The arrow indicates the position of the peak of a possible Gaussian distribution of defect in tDOS energy spectra.

CF plots of all four devices show two separate instances of increase in capacitance as illustrated in figure 4.10. This indicates the existence of two Gaussian distributions in the band-gap. The y-axis in figure 4.10 is the measured capacitance normalized to the geometric capacitance calculated from CV measurement in reverse bias.

tDOS energy spectra were extracted from CF measurements at zero bias voltage. The corresponding energy levels of the trap states were determined using the measured values of ATEF. Figure 4.11 shows the tDOS energy spectra for the blend and the neat polymer based active-layers. For all four devices, two separate Gaussian distributions are visible which was confirmed by Gaussian fit using the form,[17,19]

المنارة للاستشارات
www.manaraa.com

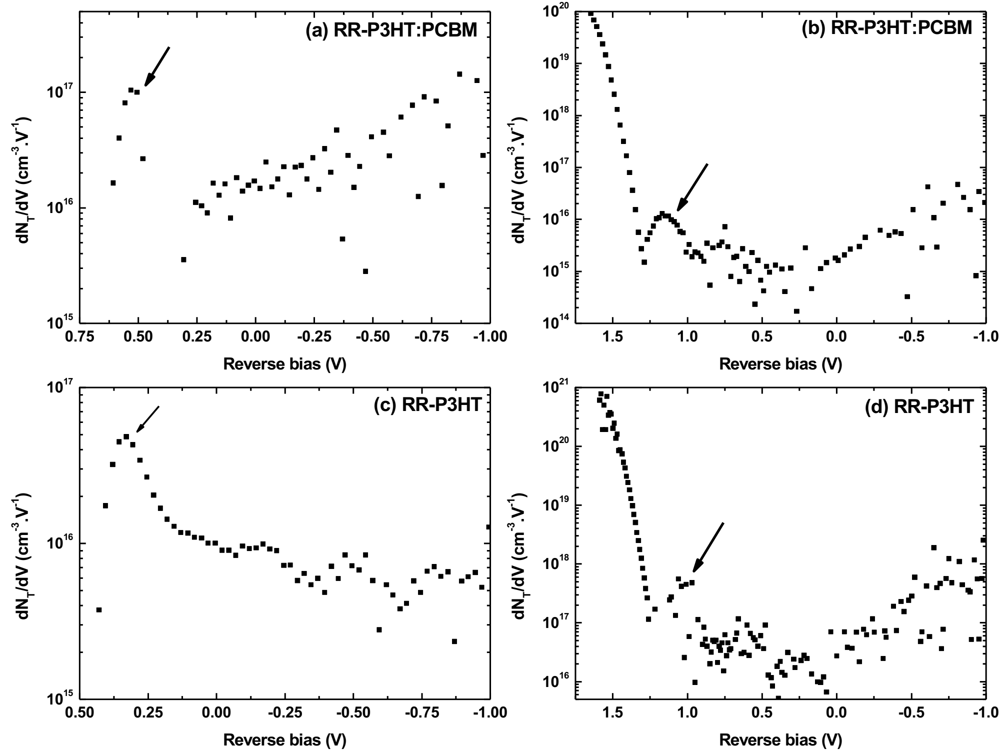

Figure 4.9: Illustration of derivative of the defect density with respect to applied bias (calculated from profiler equation) plotted with reverse bias (top left: RR-P3HT:PCBM, top right: RRa-P3HT:PCBM, bottom left: RR-P3HT, and bottom right: RRa-P3HT). The arrows indicate the corresponding peaks of Gaussian distributions.

$$N_T(E_\omega) = \frac{N_T}{\sqrt{2\pi\sigma}} exp\left[-\frac{(E_0 - E_\omega)^2}{2\sigma^2}\right]$$

Where N_T is the defect density, E_0 is the mean energy of the defect distribution and σ is the disorder parameter (that is half of the width of the distribution). The values of the fitted parameters, including the height (h) of the Gaussian distribution, of one set of devices are listed in table 4.4 (5 sets of devices examined showed good reproducibility of results).

www.manaraa.com

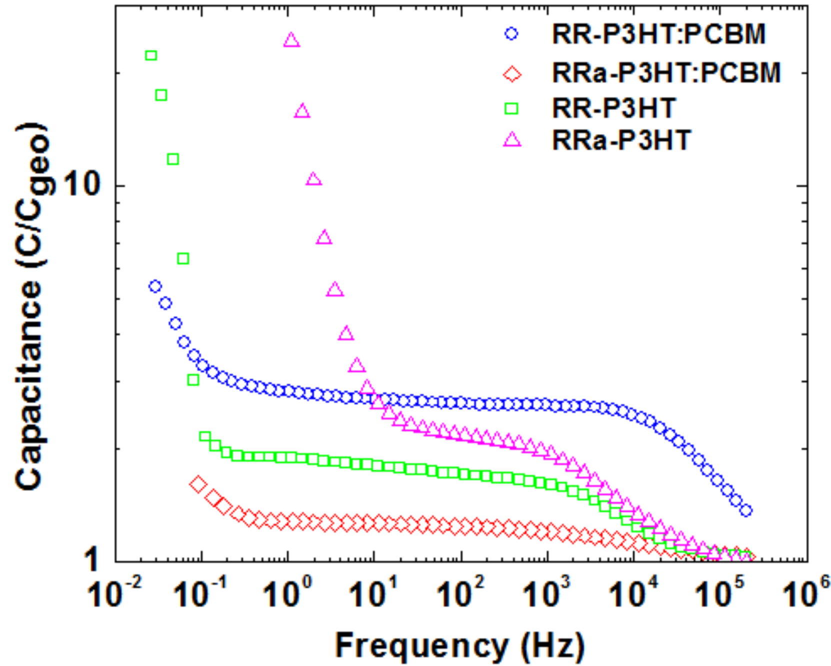

Figure 4.10: Ratio of capacitance and geometric capacitance versus frequency for the four devices investigated.

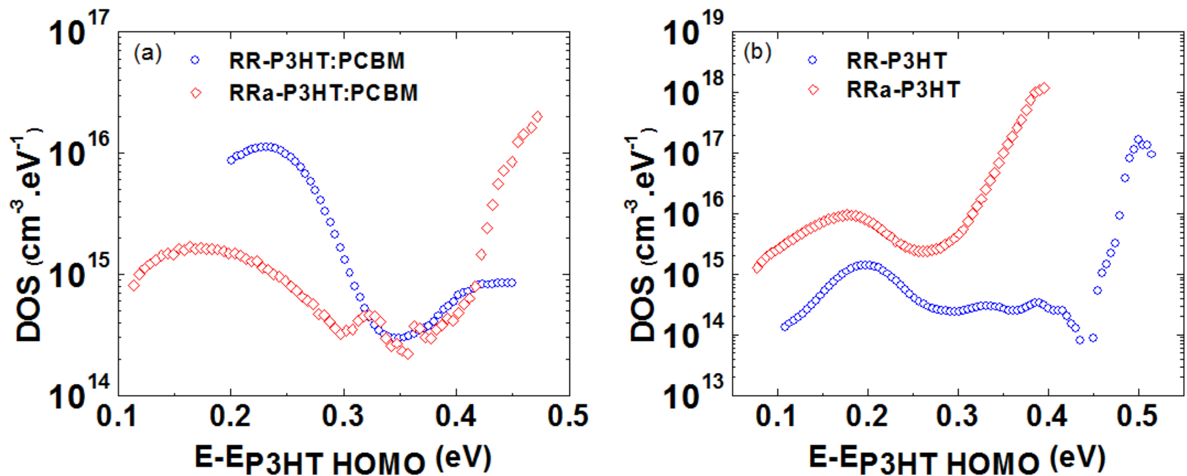

Figure 4.11: Illustration of tDOS energy spectra for (a) P3HT:PCBM devices, and (b) P3HT-only devices.

www.manaraa.com

Table 4.4: Summary of tDOS energy spectra fitted parameters.

		Band I				Band II			
		E_o (eV)	σ (meV)	h ($cm^{-3}eV^{-1}$)	N_T (cm^{-3})	E_o (eV)	σ (meV)	h ($cm^{-3}eV^{-1}$)	N_T (cm^{-3})
P3HT: PCBM	RR	0.23	34.5	1.18×10^{16}	1.11×10^{15}	0.44	51	8.52×10^{14}	1.08×10^{14}
	RRa	0.18	63.5	1.64×10^{15}	2.62×10^{14}	0.48	30	2.2×10^{16}	1.65×10^{15}
P3HT	RR	0.20	31.8	1.40×10^{15}	1.11×10^{14}	0.5	11.3	1.52×10^{17}	4.32×10^{15}
	RRa	0.17	39.4	9.34×10^{15}	9.22×10^{14}	0.39	17.02	1.19×10^{18}	5.09×10^{16}

At freeze-out condition, when the applied frequency is too high, charge carriers cannot respond to the applied signal.[28] In this situation, the capacitance response is the geometric capacitance, C=εA/d, where d is the thickness of the active-layer instead of the depletion width, A is the area of the electrode and ε is the dielectric constant.[28] It can be seen in figure 4.10 that all four devices reach geometric capacitance at high frequency; this indicates that freeze-out occurs within measurement range. CF profile at different temperatures demonstrate that the frequency around which geometric capacitance steps up, shifts to lower value at lower temperatures as shown in figure 4.12.[46] Thus, both low temperatures and high frequencies can cause freeze-out condition. Occurrence of freeze-out within the measurement range can be justified by much lower ATEF and mobility of organic semiconductors as compared to inorganic semiconductors. The measured ATEF in all four devices was in the range of 10^6 - 10^8 Hz, while for inorganic semiconductors it is reported in the range of 10^{11} - 10^{13} Hz. Another report found the value of ATEF for P3HT:PCBM system in the range of 1 to 100 Hz and we believe that resulted from improper selection of series or parallel model of equivalent circuit for small-signal measurement or inaccurate measurement of sample temperature.[47] Our extracted lower ATEF compared to inorganics indicates that freeze-out frequency for P3HT is

المنارة للاستشارات
www.manaraa.com

expected to be lower than the inorganic materials. It is also known for inorganic semiconductors that higher the charge carrier mobility, lower the temperature at which freeze-out occurs.[48,49] P3HT is known to have lower mobility than inorganic semiconductors; this also validates the freeze-out at lower frequency compared to inorganics.

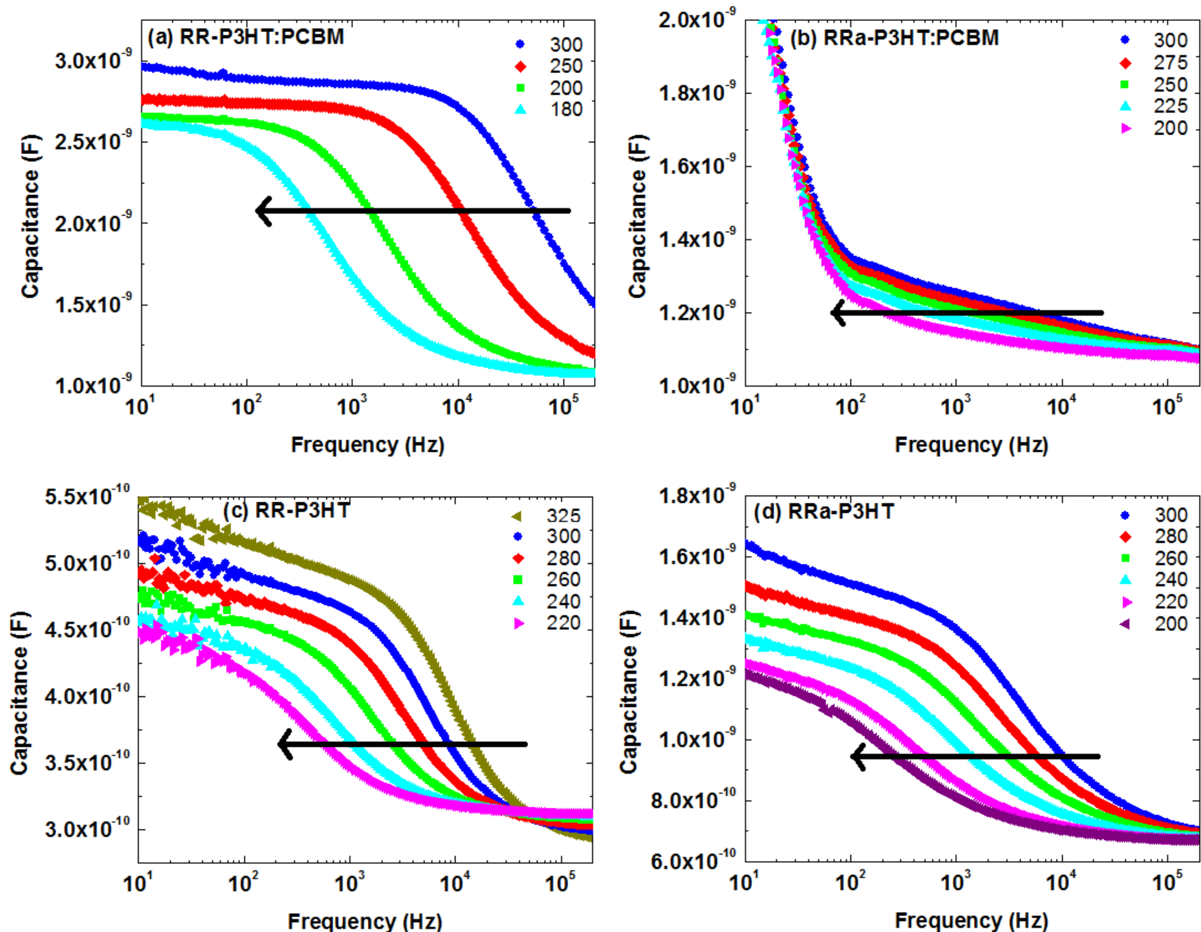

Figure 4.12: Illustration of shift of capacitance-frequency profile toward lower frequency with lower temperature. (a) RR-P3HT:PCBM, (b) RRa-P3HT:PCBM, (c) RR-P3HT, and (d) RRa-P3HT. The black arrow shows the direction of the shift of the profile at lower temperatures.

One important observation from the tDOS spectra is that the first Gaussian distribution (band I) is centered at the corresponding Fermi energy for all four devices. Thus, Fermi energy is equal to the corresponding measured activation energy. The dielectric relaxation depends on

المنارة للاستشارات
www.manaraa.com

the free carrier density with thermal activation energy of Fermi energy[28] and the first Gaussian distribution resulted from the step in the capacitance from geometric capacitance, as shown in figure 4.10. The increase in capacitance from geometric value is due to the transition of capacitance from $C = \varepsilon A/d$ to $C = \varepsilon A/< x >$, where d is the thickness of the active layer and <x> is the first moment of charge response.[28] This clearly indicates that this band is caused by free carrier response. This band may also get affected by trap distribution located at the Fermi level.

The disorder parameter, σ, (half of the width of the distribution) is directly related to doping concentration. In disordered organic semiconductors, electronic states are localized hopping sites. Due to low dielectric constant in organics, the Coulombic interaction between charged species affects the energy of localized states.[50] Doping disordered organic semiconductors produces a random distribution of dopant ions, which interact with carriers localized in intrinsic hopping sites. As a result, energy disorder is increased and there is broadening of the deep tail of the tDOS distribution.[50] As shown in table 4.2, RRa-P3HT:PCBM blend has more doping than the RR counterpart; fitted σ of band I is also higher for RRa blend. Also in the neat polymer devices, RRa-P3HT showed higher doping, which results into an inherent higher value of σ.

In organic semiconductors, as discussed, additional deep Columbic traps of opposite polarity are created with doping. These traps strongly suppress the carrier mobility.[50] Electron mobility of the blend was measured using impedance spectroscopy. Obtained Nyquist plots are shown in figure 4.13. The resultant minority carrier mobility of both RR and RRa blend is illustrated in figure 4.14(a) as a function of applied bias where it is evident that the electron mobility of the RR-P3HT:PCBM is more than one order of magnitude higher than the

المنارة للاستشارات
www.manaraa.com

RRa-P3HT:PCBM. Higher electron mobility is supported by the obtained minority carrier transit time (time electron takes to diffuse to the electrode). Obtained electron transit time indicates that electron reaches the electrode more than one order of magnitude faster in RR-P3HT:PCBM than in RRa-P3HT:PCBM, as shown in figure 4.14(b).

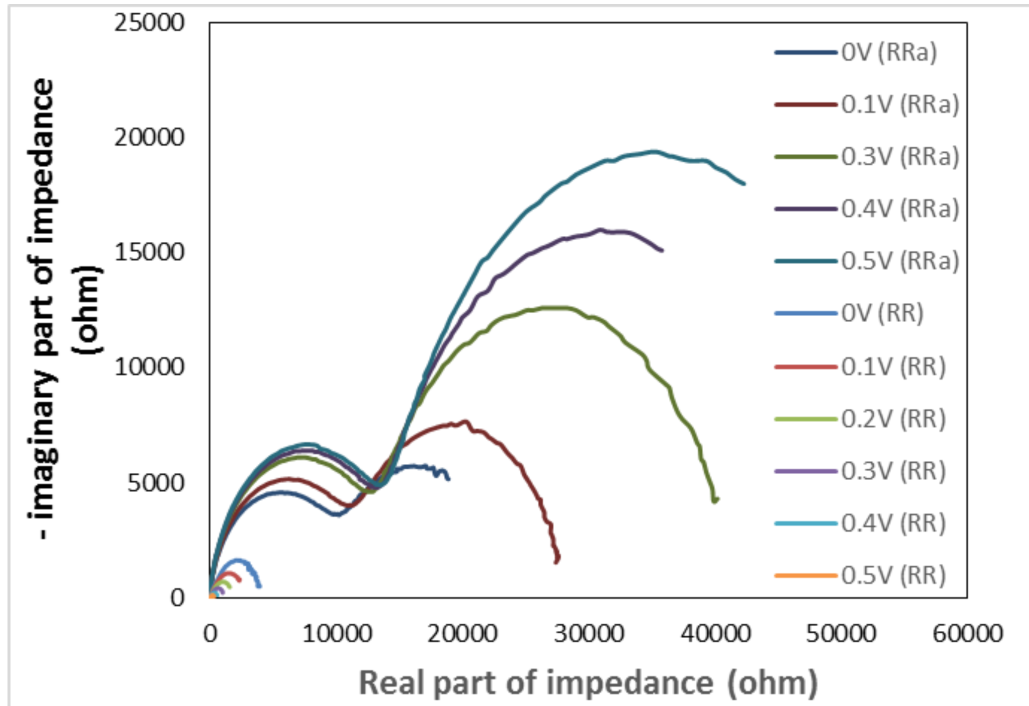

Figure 4.13: Nyquist plot at different applied biases obtained from impedance spectroscopy under illumination (1 sun) for both RR-P3HT:PCBM and RRa-P3HT:PCBM. It is evident that the impedance range of the RRa- is larger that the regular one.

The area of band I can readily be assigned to the amount of free carriers while band I is resulted from free-carrier response and the width of band I is related to the amount of doping. In table 4.4, N_T indicates the area of the corresponding band and the area of band I corresponds to the density of free carriers available in the material. For band I of RR-P3HT:PCBM, N_T is 1.11×10^{15} cm^{-3} which is close to the measured doping 1.20×10^{15} cm^{-3} (table 4.2). For the other three devices, the extracted free carrier density (N_T of band I) is around one order of

المنارة للاستشارات
www.manaraa.com

magnitude less than measured doping (table II) which can be explained by lower mobility of RRa-P3HT:PCBM and absence of bulk-heterojunction (BHJ) in RR-P3HT and RRa-P3HT. BHJ is known to improve the carrier transport in OPV.[51]

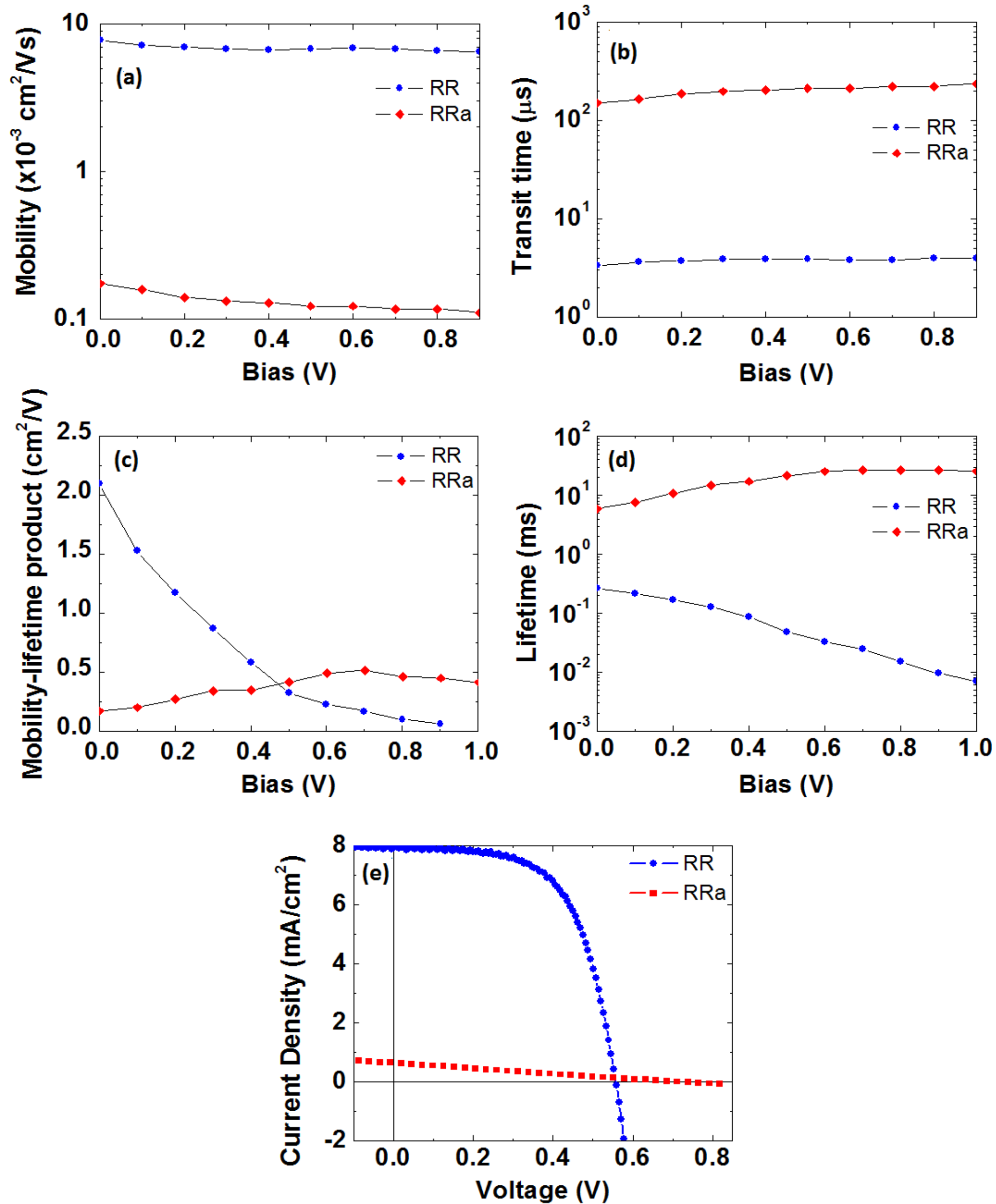

Figure 4.14: Illustration of the results of impedance spectroscopy (IS) and light IV under illumination (1 sun) of RR-P3HT:PCBM (in blue) and RRa-P3HT:PCBM (in red) as a function of applied bias. (a) Minority carrier mobility, (b) minority carrier transit time, (c) mobility-lifetime product, and (d) minority carrier lifetime, and (e) Light IV.

المنارة للاستشارات
www.manaraa.com

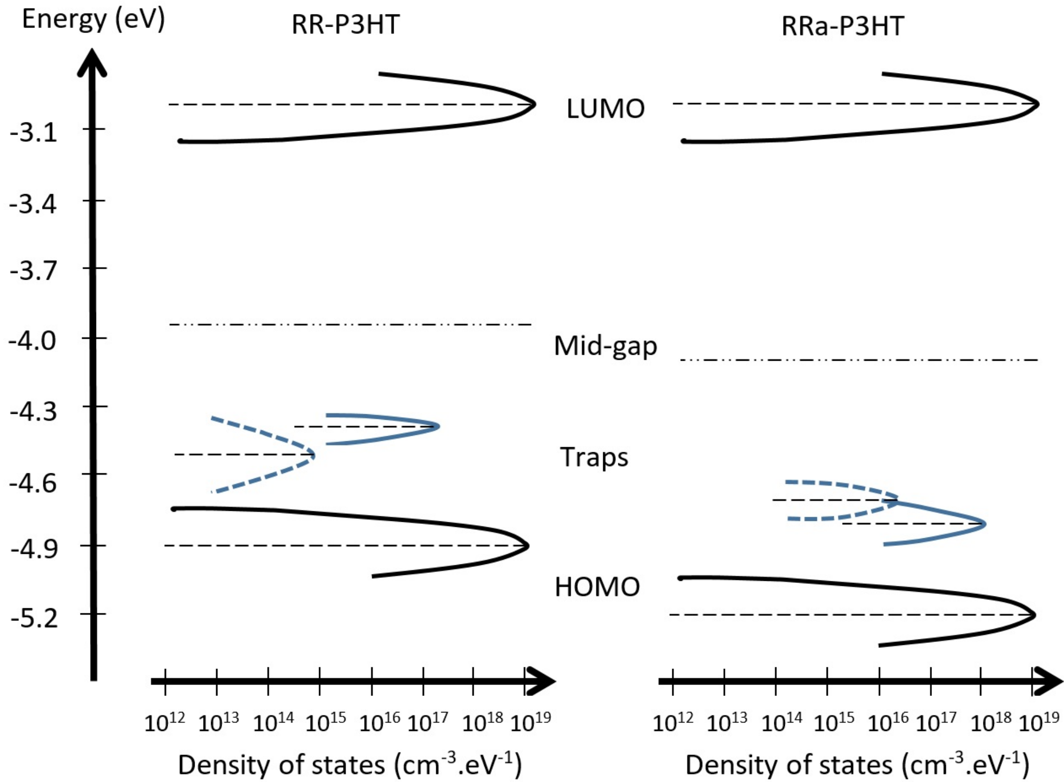

Figure 4.15: Conceptual illustration of the energy diagram of RR-P3HT and RRa-P3HT with the distribution of extracted traps. Trap distribution in presence of PCBM is illustrated with dashed band.

All four devices showed a second Gaussian distribution (band II) at higher energy in the tDOS profile. This band II stems from the step in capacitance at lower frequencies as shown in figure 4.10. Deep defects have low emission rate due to which they cannot charge and discharge when the applied AC signal has high frequency. As the frequency is lowered, these states respond if the state crosses the Fermi level and consequently the band II is obtained in tDOS energy spectra. Thus, the area of band II represents the corresponding defect density in the material. As this band II exists in all four devices, this distribution is inherent to P3HT. Both RR- and RRa- P3HT:PCBM blends inherit lower amount of defect density than the respective P3HT-only devices. This indicates that PCBM mitigates a portion of defects in the blend. For both cases, blends and the neat polymer, the RR species have nearly one order of

المنارة للاستشارات
www.manaraa.com

magnitude lower defect density in band II than RRa. This shows that the corresponding defect states originate from morphological disorder or polymer chain packing. Energy diagram of both RR-P3HT and RRa-P3HT with extracted trap distribution is illustrated in figure 4.15.

Two observations are made from the depth profile: mean energy of the obtained defect distribution (band II) in tDOS energy spectra for all four devices is exactly same as that predicted from the respective depth profile, and band I, which is concluded as the free carrier response, is absent in depth profile. As depth profile was obtained using profiler equation and CV data measured with a constant low frequency AC signal, freeze-out did not occur; so, band I is absent. We can thus conclude that CV measurement can be utilized to detect defect bands in the band-gap as it provides exact energetic location of band II. One advantage of CV measurements is that unlike CF measurements, it does not suffer from the noise and equipment limitation at low frequency.

Figure 4.14(c) shows the mobility-minority carrier lifetime product as a function of applied bias. Initially the product of RR-P3HT:PCBM is higher than RRa-P3HT:PCBM which can be expected as RRa-P3HT is more disordered. But, the product gets smaller after around 0.5V bias; this behavior is readily supported by the current density versus voltage plot (Fig. 9(e)) which shows that after 0.55 V, generated power is still positive for the RRa species. When minority carrier lifetime alone is plotted with bias (Fig. 4.14(d)), lifetime for RR-P3HT:PCBM is found to be more than one order of magnitude lower than RRa-P3HT:PCBM, which indicates that there is higher amount of recombination in the RR-P3HT:PCBM. Higher amount of recombination in spite of having lower amount of defect density can be explained by the availability of higher amount of free carriers in the RR-P3HT:PCBM devices.

المنارة للاستشارات
www.manaraa.com

4.3 Conclusion

In this chapter, the tDOS energy spectra of RR- and RRa-P3HT was determined using the measured values of maximum trap emission rate. Both RR and RRa-P3HT and their blends with PCBM were probed to investigate the physical origins behind the tDOS energy spectra. Among the two obtained distributions, the lower energy band is concluded to be stemming from free carrier response contrary to its misinterpretation in literature as a defect band. The higher energy band is concluded to be stemming from morphological defects; RRa-P3HT inherits one order of magnitude higher amount of defects than RR-P3HT. We also show that these defects are mitigated by PCBM. Both CF and CV data were in good agreement with mean energy of the higher energy band matching that extracted from the depth profile. Minority carrier lifetime, mobility and transit time in both RR- and RRa-P3HT:PCBM, extracted utilizing IS method, were also discussed. It is believed that insights presented in this report are useful for defect characterization of amorphous and non-crystalline semiconductor devices beyond those based on conjugated organic materials.

4.4 Experimental

Devices were fabricated on ITO coated glass substrates (5-15 Ω/ , Delta Technologies). Substrates were ultrasonicated consecutively in detergent (alconox), de-ionized water, and 2-propanol for 10 minutes. Substrates were blown dry with nitrogen and kept on a hot plate at 130^0C for 10 minutes. They were then treated with air plasma and ~40 nm of PEDOT:PSS (VP 4083 from HC Stark) was spin coated on them at 4000 rpm for 60 seconds. Samples were then annealed at 140^0C for 10 minutes and transferred inside the glove box. Active-layer solutions were prepared inside the glove box. RR-P3HT, RRa-P3HT and $PC_{60}BM$

المنارة للاستشارات
www.manaraa.com

from 1-materials Inc. were dissolved in 1, 2-dichlorobenzene (DCB) from Sigma-Aldrich with dilution of 40mg/ml for RR-P3HT:PCBM (1:1 by weight), RRa-P3HT:PCBM (1:1 by weight), RR-P3HT, and RRa-P3HT. These solutions were stirred at 850 rpm at 50^0C on a hot plate for more than 12 hours and filtered using a 0.22 μm PTFE filter (Sigma-Aldrich) before spin coating on the PEDOT:PSS coated ITO slides at 400 rpm for RR-P3HT:PCBM and RRa-P3HT:PCBM, and 450 rpm for RR-P3HT and RRa-P3HT for 40 seconds. Finally, 20 nm of Ca and 100 nm of Al were thermally evaporated sequentially on top of the slow dried (solvent annealed in a petri dish) films as the electrode. Thermal evaporation was done in 10^{-6} mbar vacuum at rate slower than 0.5 and 5 A^o/s, respectively.

CV measurements were conducted using PARSTAT 2273 LCR meter at room temperature in dark and vacuum. IS measurements were also conducted using PARSTAT 2273 LCR meter at room temperature under 1 sun (AM1.5) illumination in air. CF measurements were carried out in a cryostat using HIOKI IM3533-01 LCR meter in dark and vacuum. A continuous flow of liquid nitrogen in the cryostat was utilized to vary the temperature between 100K and 375K. Temperature was monitored using platinum resistance temperature detectors (RTDs).

Current-voltage measurements under illumination were performed at a simulated AM1.5 condition using an ELH quartzline lamp. A crystalline silicon photodiode coupled with a KG-5 filter was utilized to calibrate the system.

المنارة للاستشارات

www.manaraa.com

4.5 References

1. *Organic photovoltaics*. (Wiley-VCH, 2008).

2. G. D. Tayebeh Ameri, Christoph Lungenschmied, Christoph J. Brabec, Energ Environ Sci (2009).

3. T. K. K. T. U. Rau, J. Phys. Chem. C **113** (17958–17966) (2009).

4. C. Z. Zhicai He, Shijian Su, Miao Xu, Hongbin Wu, Yong Cao, Nature Photonics (2012).

5. K. T. Thomas Kirchartz, Uwe Rau, J Phys Chem C (2009).

6. T. Muntasir, S. Das Gupta and M. S. Islam, 2012 Ieee International Conference on Electron Devices and Solid State Circuit (Edssc) (2012).

7. T. M. Md. Khan, A. Rahman, U. Acharjee, Md. Layek, in *IEEE Symposium on Industrial Electronics and Applications (ISIEA)* (Langkawi, Malaysia, 2011).

8. M. I. Tanvir Muntasir, S. Gupta, in *International Conference on Informatics, Electronics & Vision (ICIEV)* (Dhaka, Bangladesh, 2012).

9. J. A. Carr and S. Chaudhary, Energ Environ Sci **6** (12), 3414-3438 (2013).

10. B. A. Gregg, J Phys Chem C **113** (15), 5899-5901 (2009).

11. B. A. Gregg, Soft Matter **5** (16), 2985-2989 (2009).

12. G. Garcia-Belmonte, P. P. Boix, J. Bisquert, M. Lenes, H. J. Bolink, A. La Rosa, S. Filippone and N. Martin, J Phys Chem Lett **1** (17), 2566-2571 (2010).

13. J. Bhattacharya, R. W. Mayer, M. Samiee and V. L. Dalal, Appl Phys Lett **100** (19) (2012).

14. P. P. Boix, G. Garcia-Belmonte, U. Munecas, M. Neophytou, C. Waldauf and R. Pacios, Appl Phys Lett **95** (23) (2009).

www.manaraa.com

15. B. Ecker, J. C. Nolasco, J. Pallares, L. F. Marsal, J. Posdorfer, J. Parisi and E. von Hauff, Adv Funct Mater **21** (14), 2705-2711 (2011).

16. R. C. I. MacKenzie, C. G. Shuttle, G. F. Dibb, N. Treat, E. von Hauff, M. J. Robb, C. J. Hawker, M. L. Chabinyc and J. Nelson, J Phys Chem C **117** (24), 12407-12414 (2013).

17. K. S. Nalwa, R. C. Mahadevapuram and S. Chaudhary, Appl Phys Lett **98** (9) (2011).

18. J. A. Carr and S. Chaudhary, Appl Phys Lett **100** (21) (2012).

19. J. A. Carr and S. Chaudhary, J Appl Phys **114** (6) (2013).

20. T. Walter, R. Herberholz, C. Muller and H. W. Schock, J Appl Phys **80** (8), 4411-4420 (1996).

21. H. C. F. Martens, P. W. M. Blom and H. F. M. Schoo, Phys Rev B **61** (11), 7489-7493 (2000).

22. N. I. Craciun, J. Wildeman and P. W. M. Blom, Phys Rev Lett **100** (5) (2008).

23. J. A. Carr, K. S. Nalwa, R. Mahadevapuram, Y. Q. Chen, J. Anderegg and S. Chaudhary, Acs Appl Mater Inter **4** (6), 2831-2835 (2012).

24. M. Campoy-Quiles, Y. Kanai, A. El-Basaty, H. Sakai and H. Murata, Org Electron **10** (6), 1120-1132 (2009).

25. X. M. Jiang, R. Osterbacka, C. P. An and Z. V. Vardeny, Synthetic Met **137** (1-3), 1465-1468 (2003).

26. S. S. Pandey, W. Takashima, S. Nagamatsu, T. Endo, M. Rikukawa and K. Kaneto, Jpn J Appl Phys 2 **39** (2A), L94-L97 (2000).

27. S. Singh, B. Pandit, T. P. Basel, S. Li, D. Laird and Z. V. Vardeny, Phys Rev B **85** (20) (2012).

المنارة للاستشارات

www.manaraa.com

28. P. Z. J. Heath, *Advanced Characterization Techniques for Thin Film Solar Cells*. (2011).

29. M. S. A. Abdou, F. P. Orfino, Y. Son and S. Holdcroft, J Am Chem Soc **119** (19), 4518-4524 (1997).

30. S. Hoshino, M. Yoshida, S. Uemura, T. Kodzasa, N. Takada, T. Kamata and K. Yase, J Appl Phys **95** (9), 5088-5093 (2004).

31. G. Dennler, C. Lungenschmied, N. S. Sariciftci, R. Schwodiauer, S. Bauer and H. Reiss, Appl Phys Lett **87** (16) (2005).

32. L. C. Kimerling, J Appl Phys (1974).

33. A. G. B. Biswajit Ray, Bryan W. Boudouris, Muhammad A. Alam, J. Phys. Chem. C **118** (31), 17461-17466 (2014).

34. S. S. Hegedus and E. A. Fagen, J Appl Phys **71** (12), 5941-5951 (1992).

35. S. M. Sze, *Semiconductor Devices Physics and Technology*. (John Wiley & Sons Inc., New York, 1985).

36. B. G. S. S. Banerjee, *Solid State Electronic Devices*. (Prentice-Hall, 1995).

37. A. Kokil, K. Yang and J. Kumar, J Polym Sci Pol Phys **50** (15), 1130-1144 (2012).

38. G. Garcia-Belmonte, A. Munar, E. M. Barea, J. Bisquert, I. Ugarte and R. Pacios, Org Electron **9** (5), 847-851 (2008).

39. J. Bisquert, L. Bertoluzzi, I. Mora-Sero and G. Garcia-Belmonte, J Phys Chem C **118** (33), 18983-18991 (2014).

40. G. Garcia-Belmonte, P. P. Boix, J. Bisquert, M. Sessolo and H. J. Bolink, Sol Energ Mat Sol C **94** (2), 366-375 (2010).

المنارة للاستشارات

www.manaraa.com

41. B. J. Leever, C. A. Bailey, T. J. Marks, M. C. Hersam and M. F. Durstock, Adv Energy Mater **2** (1), 120-128 (2012).

42. G. Perrier, R. de Bettignies, S. Berson, N. Lemaitre and S. Guillerez, Sol Energ Mat Sol C **101**, 210-216 (2012).

43. J. Bisquert, J Phys Chem B **106** (2), 325-333 (2002).

44. *Agilent impedance measurement handbook*, 4th edition ed. (Agilent Technologies).

45. H. Hintz, H. Peisert, H. J. Egelhaaf and T. Chasse, J Phys Chem C **115** (27), 13373-13376 (2011).

46. M. B. S. Grecu, A. Opitz, W. Brutting, (2004).

47. P. P. Boix, J. Ajuria, I. Etxebarria, R. Pacios and G. Garcia-Belmonte, Thin Solid Films **520** (6), 2265-2268 (2012).

48. J. c. D. A K Walton, J. Phys. C: Solid State Phys (1977).

49. H. Y. H. A. Ohtomo, (2004).

50. V. I. Arkhipov, P. Heremans, E. V. Emelianova and H. Bassler, Phys Rev B **71** (4) (2005).

51. C. J. T. Alexander L. Ayzner, Sarah H. Tolbert, Benjamin J. Schwartz, (2009).

المنارة للاستشارات

www.manaraa.com

CHAPTER V

DEFECTS IN SOLUTION-PROCESSED DITHIENYLSILOLE-BASED SMALL-MOLECULE PHOTOVOLTAIC THIN-FILMS

DTS-$(FBTTh_2)_2$ is a prominent solution-processable small-molecule donor for donor-acceptor bulk-heterojunction organic photovoltaics. Power conversion efficiency of DTS-$(FBTTh_2)_2$ based photovoltaic devices exceeds 8%. This paper reports on the distribution of sub-bandgap trap states in DTS-$(FBTTh_2)_2$. Trap states were probed using admittance spectroscopy and low-frequency capacitance-voltage profiling, and analyzed using established theoretical models. Three distributions were revealed in the trap density of states energy spectra. Key observations were: (1) thicker solution-processed films with higher drying time had 55% less traps than thinner films that dried relative faster, (2) blending of DTS-$(FBTTh_2)_2$ with the acceptor $PC_{70}BM$ introduced traps at the center of the donor-acceptor interfacial bandgap. Charge carrier dynamics in DTS-$(FBTTh_2)_2$ based thin-films was also characterized using impedance spectroscopy.

5.1 Introduction

Organic photovoltaics (OPVs) are considered one of the potential candidates for economical solar-electric power conversion.[1,2,3] The most successful device architecture in OPVs is the bulk-heterojunction (BHJ), in which donor and acceptor materials are intermixed in the photovoltaic active-layer.[4] Donors are either polymers or small-molecules. While early small-molecule based devices were mostly fabricated by heating-assisted evaporation methods, some recent molecular structures are amenable to solution processing.[6,8,10] Small-

www.manaraa.com

molecules are preferable over polymers due to their more well-defined molecular structure, lower batch to batch variability of molecular weight, higher material purity, and simpler purification methods.[4,5,6] Optical, electronic, and physical characteristics of small-molecules are also more controllably tunable than polymers.[5] Highest reported power conversion efficiency (PCE) in small-molecule based single junction BHJ OPVs is now above 9%.[8] One of the popular solution-processed small-molecule donors is 7,7'-(4,4-bis(2-ethylhexyl)-4H-silolo[3,2-b:4,5-b']-dithiophene-2,6-diyl)bis(6-fluoro-4-(5'-hexyl-[2,2'-bithiophen]-5-yl)benzo[c][1,2,5]thiadiazole) ((DTS-$(FBTTh_2)_2$). DTS-$(FBTTh_2)_2$ is an attractive donor material with device efficiencies >8%.[12,13] This chapter reports on the sub-bandgap traps in DTS-$(FBTTh_2)_2$ based thin-films. Understanding of traps is important as they affect several optoelectronic properties relevant to achieving high performance devices. For example, trap states introduce recombination centers and charged point sites; former leads to loss of free carriers and latter leads to energetic disorder which lowers charge carrier mobility.[11] Trap states also have detrimental effect on excitons.[11] Although, there are reports in the literature on characterization of trap states in polymer based OPVs, to the best of our knowledge, there is no report on energy-level identification and characterization of trap states in recent solution-processed SM-OPVs.

In this study, we probed the trap states in DTS-$(FBTTh_2)_2$ based thin-films using capacitance measurements, and analyzed tDOS energy spectra from the Fermi level to the midgap, utilizing the models of Kimerling, Cohen and Lang, and Walter *et al.*[14-16] We investigated DTS-$(FBTTh_2)_2$-only devices as well as BHJ devices with acceptor [6-6]-phenyl C_{70} butyric acid methyl ester ($PC_{70}BM$). We also varied spin-coating conditions to realize DTS-$(FBTTh_2)_2$ and DTS-$(FBTTh_2)_2$:$PC_{70}BM$ thin-films with two different film thicknesses

المنارة للاستشارات
www.manaraa.com

(125 ± 15 nm and 200 ± 15 nm; the former thickness is typical of high performance DTS-$(FBTTh_2)_2$ based OPVs and will be referred to as the regular-film,[12,13] and the latter will be referred to as the thick-film). Studying the effect of film-thickness variation on trap states was motivated by a previous report on polythiophene which showed that thicker films dry slower and have lower concentration of traps.[17] To obtain accurate tDOS energy spectra, maximum trap emission rate, dielectric constant, doping concentration, Fermi energy, and built-in voltage at the donor-cathode interface for all samples were extracted from admittance spectroscopy (AS) and capacitance-voltage (CV) profiling.[18] In addition to quantifying the trap-state distributions and revealing aspects of their physical origins, we also employed impedance spectroscopy to measure mobility, electron transit-time, and electron lifetime in all samples.

5.2 Existence of Trap States in The Bandgap of DTS-$(FBTTh_2)_2$

Organic The device structure employed for all measurements was anode/hole-transport-layer/active-layer (DTS-$(FBTTh_2)_2$ or DTS-$(FBTTh_2)_2$:$PC_{70}BM$)/cathode (Ca/Al). The detailed device structure and current-density versus voltage curves under illumination are illustrated in figure 5.1(a) and 5.1(b), respectively. Table 5.1 summarizes the photovoltaic performance of DTS-$(FBTTh_2)_2$:$PC_{70}BM$ devices (three sets of devices examined showed good reproducibility of results). PCE of the regular-film device is 6.25% while for the thick-film device it is 4.4%. Devices with 100 nm thick DTS-$(FBTTh_2)_2$:$PC_{70}BM$ active-layers give optimum PCE; but almost complete depletion occurred for those devices at 0 V bias voltage.[12,13] CV-profiling method fails to provide doping concentration when complete depletion occurs; so, we worked with thicker active-layers that give less PCE than the state of

المنارة للاستشارات
www.manaraa.com

the art.[22] Devices with DTS-$(FBTTh_2)_2$ only active-layer showed almost no photovoltaic behavior due to the absence of acceptor material in the active-layer.

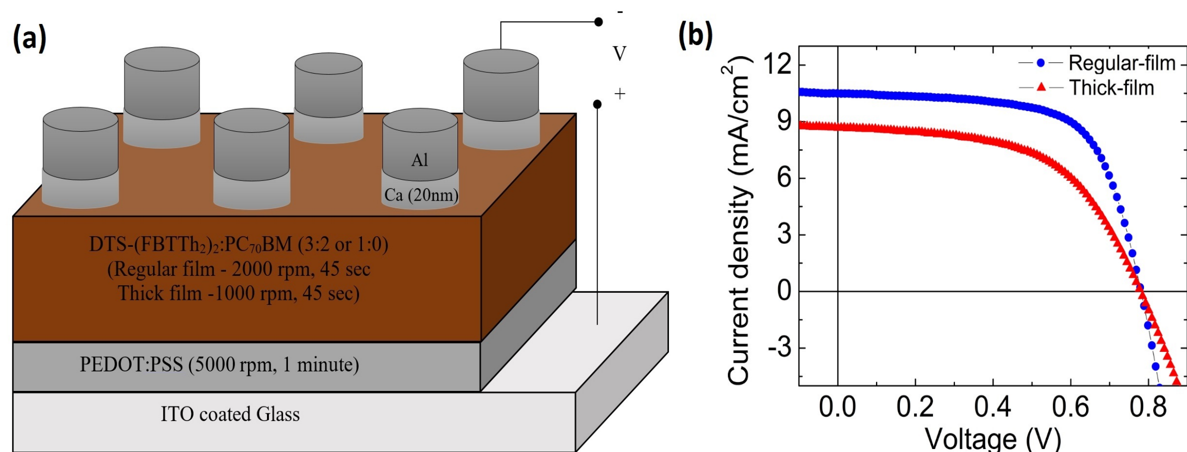

Figure 5.1: (a) Schematic of the device structure employed. (b) Illuminated current-density vs. voltage characteristics of DTS-$(FBTTh_2)_2$:$PC_{70}BM$ devices.

Table 5.1: Summary of photovoltaic performance of DTS-$(FBTTh_2)_2$:$PC_{70}BM$ devices.

	125 nm thick DTS$(FBTTh_2)_2$:$PC_{70}BM$ film	*200 nm thick DTS$(FBTTh_2)_2$:$PC_{70}BM$ film*
Open-circuit voltage (V)	0.78	0.78
Short-circuit current (mA/cm^2)	10.40	8.56
Fill-factor (%)	65	55
PCE (%)	6.25	4.40

The associated band-diagram of the complete device is shown in figure 5.2. Here, the Fermi level of DTS-$(FBTTh_2)_2$ and $PC_{70}BM$ is assumed to be aligned with their HOMO and LUMO level, respectively. Though, the active layer is not completely depleted when no reverse bias voltage is applied, for simplicity this is not shown in this diagram. The work function of Al is assumed 4.3eV. The work function of 20 nm thick Ca is interpreted to be pinned at the 4.3eV which is also the LUMO level of $PC_{70}BM$. In donor material, exciton is generated from

المنارة للاستشارات
www.manaraa.com

photon energy. The exciton gets dissociated into free carriers at the donor-acceptor interface. In the active layer bulk-heterojunction, the electron is transferred to the cathode from the LUMO of $PC_{70}BM$. Similarly, the hole is transferred to the HTL from the HOMO of DTS-$(FBTTh_2)_2$. Finally, the hole is transferred to the anode (ITO) from HTL.

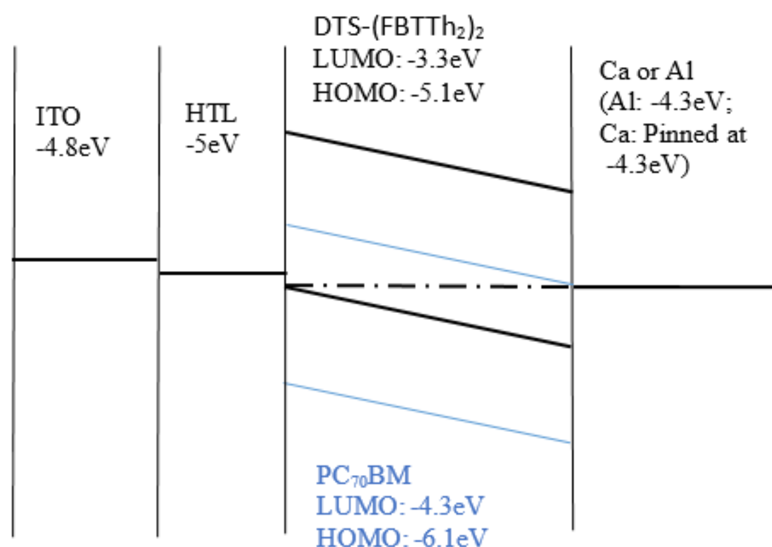

Figure 5.2: Illustration of the band-diagram of the complete device. The stated energy values are from the vacuum level.

In the active-layer, DTS-$(FBTTh_2)_2$ serves as the donor material which is analogous to p-type semiconductor in inorganics and $PC_{70}BM$ serves as the acceptor material which is analogous to n-type semiconductor in inorganics.[19,20,34] DTS-$(FBTTh_2)_2$:$PC_{70}BM$ blend active layer is composed of mixing of DTS-$(FBTTh_2)_2$ and $PC_{70}BM$ where each compound keeps its microscopic composition.[4] For this reason, both DTS-$(FBTTh_2)_2$ and $PC_{70}BM$ have interfaces with the cathode. The band-diagrams associated with DTS-$(FBTTh_2)_2$/cathode interface and $PC_{70}BM$/cathode interface are shown in figure 5.3(a) and 5.3(b), respectively.

www.manaraa.com

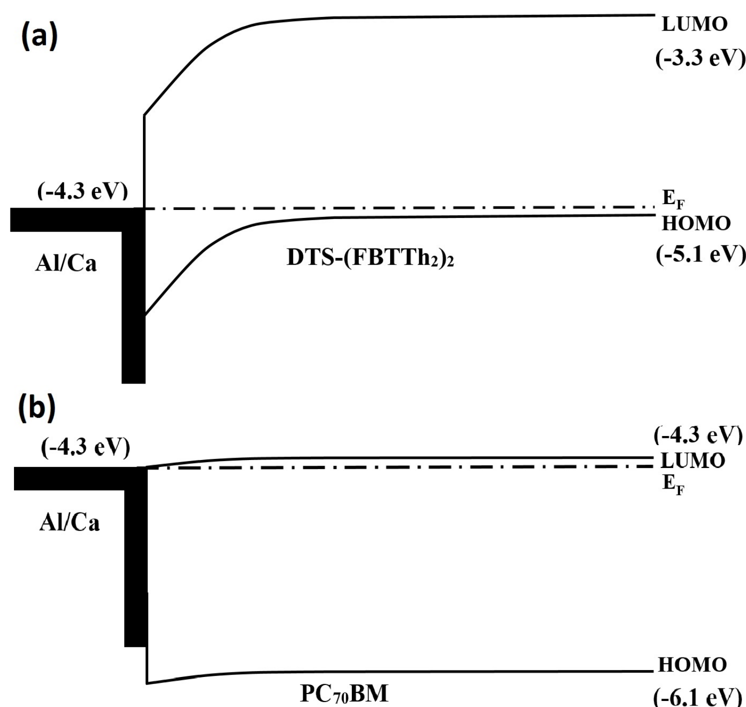

Figure 5.3: Band-diagram showing the donor-cathode and acceptor-cathode interface separately for the case of active-layer of DTS-$(FBTTh_2)_2$:$PC_{70}BM$ blend (a) Band-diagram showing the Schottky-junction formed at the cathode-DTS-$(FBTTh_2)_2$ interface. (b) Band-diagram showing the Ohmic-contact formed at the cathode-$PC_{70}BM$ interface.

AS and CV-profiling methods exploit the depletion region of a semiconductor junction.[14-16] As it is shown in figure 5.3, only the donor material forms Schottky-junction at the DTS-$(FBTTh_2)_2$/cathode interface and this junction displays a parallel-plate-like capacitance. As the acceptor material forms Ohmic-contact at the $PC_{70}BM$/cathode interface, there is no depletion region at this interface and this interface is not probed in our experiments. As the capacitance response comes from the Schottky-junction formed at the DTS-$(FBTTh_2)_2$/cathode interface, we have extracted properties of DTS-$(FBTTh_2)_2$ utilizing AS and CV-profiling methods. Mott-Schottky (MS) relation for this Schottky-junction is expressed as,[21]

www.manaraa.com

$$\frac{1}{C^2} = \frac{2}{A^2 q \varepsilon N_A}(V_{bi} - V_{dc})$$

Here, C is the capacitance of the junction, V_{dc} the applied bias, N_A the mobile-charge density of the donor-material, V_{bi} the built-in voltage of the junction, ε the dielectric constant of the donor-material, q the charge of an electron, and A the area of the contact. N_A is extracted from the slope of the $1/C^2$ versus V_{dc} plot, also known as the MS-profile. As trap states in the bandgap of DTS-$(FBTTh_2)_2$ cross the Fermi level in the depletion region (formed at the DTS-$(FBTTh_2)_2$/cathode interface and illustrated in figure 3.9) as a function of small signal frequency or DC voltage or both, parallel-plate-like capacitance of the junction is augmented by the dynamics of change in occupancy of trap states.[14-16,18,21,35] Thus, extracted N_A includes a portion of the trap density in DTS-$(FBTTh_2)_2$. figure 5.4(a) and (b) illustrates the MS-profile of the DTS-$(FBTTh_2)_2$:$PC_{70}BM$ and DTS-$(FBTTh_2)_2$ regular-films, respectively, obtained from CV profiling at different small-signal frequencies.[18] A strong dependence of the MS-profile slope on both bias voltage and small-signal frequency is evident. Band-bending at the junction increases with reverse-bias and more trap states are pulled down to the Fermi level.[14,15,21] A decrease in the slope of the MS-profile with reverse-bias is apparent; this indicates the existence of trap states. The emission-rate of trap states depends on their location in the bandgap; the deeper the traps are toward the midgap, the slower is the emission-rate.[15] In MS-profiles for frequencies below 500 kHz, slope at a given bias gets lower as the small-signal frequency is reduced because trap states with slower emission rates start responding to the small-signal at lower frequencies.[15,22] MS-profiles for small-signal frequencies above 500 kHz exhibit less capacitance due to carrier freeze-out at high-frequency.

المنارة للاستشارات
www.manaraa.com

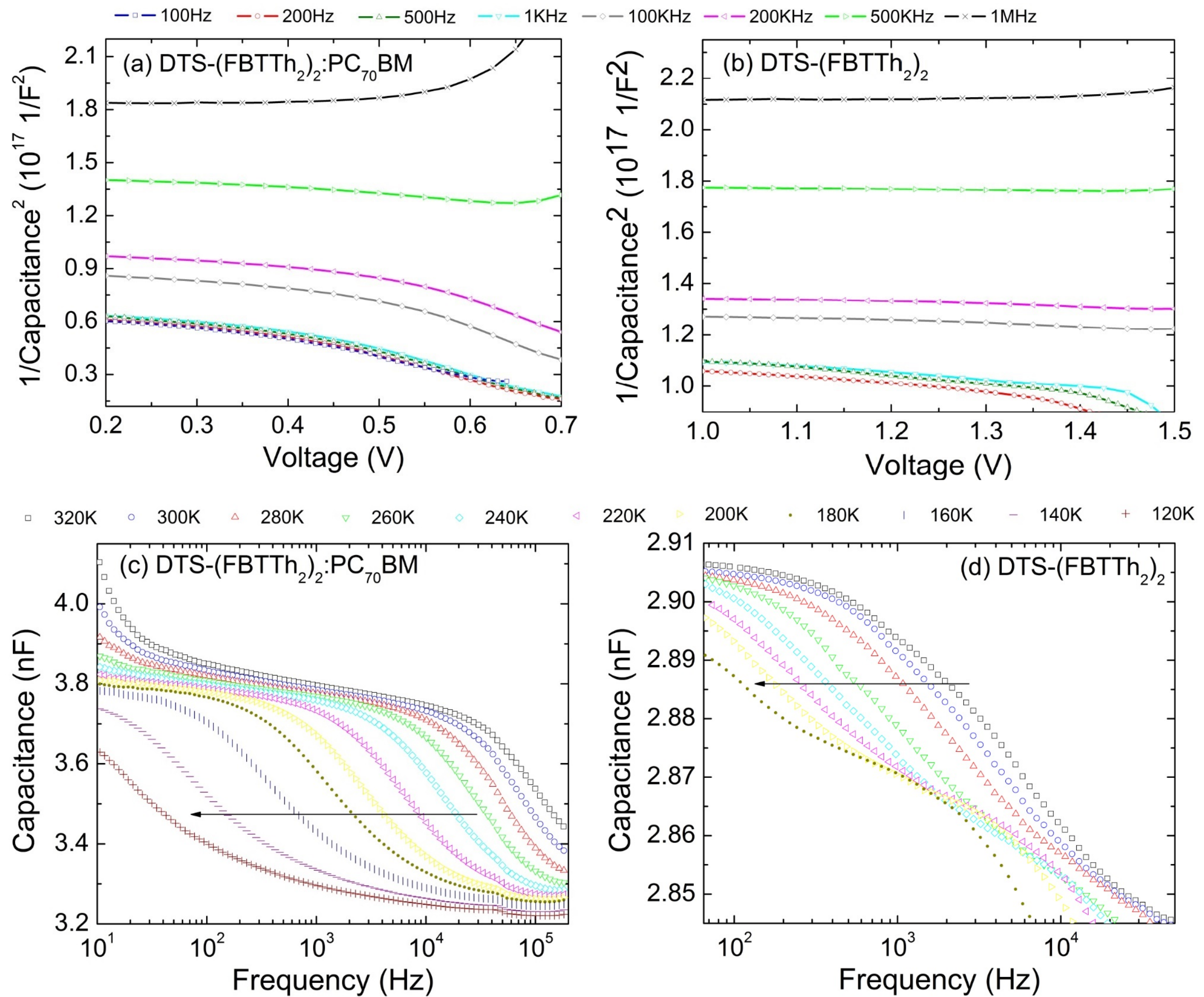

Figure 5.4: (a) Mott-Schottky profiles of DTS-$(FBTTh_2)_2$:$PC_{70}BM$ regular-film at different small-signal frequencies. (b) Mott-Schottky profiles of DTS-$(FBTTh_2)_2$ regular-film at different small-signal frequencies. (c) Capacitance versus frequency plots of DTS-$(FBTTh_2)_2$:$PC_{70}BM$ regular-film at different temperatures with 0 V DC-bias. (d) Capacitance versus frequency plots of DTS-$(FBTTh_2)_2$ regular-film at different temperatures with 0 V DC-bias. The arrow indicates left shift in curves at lower temperatures.

Dependence of the junction-capacitance on small-signal frequency is more evident in figure 5.4(c) and (d), where measured junction-capacitance of the DTS-$(FBTTh_2)_2$/cathode junction of DTS-$(FBTTh_2)_2$:$PC_{70}BM$ and DTS-$(FBTTh_2)_2$ regular-films, respectively, are plotted versus small-signal frequencies ranging from 10 Hz to 200 kHz. As the small-signal frequency is swept from high to low values, trap states located deeper into the bandgap respond

www.manaraa.com

to the signal. Steep changes in capacitance in the CF-profile result from response of trap states in the bandgap. A left shift in the CF-profile at lower temperatures is a direct result of the dependence of trap emission rate on temperature, as the thermal trap emission rate in a p-type semiconductor is expressed as,[16,18]

$$e_p = N_v v_{\mathrm{th}} \sigma_p exp\left(\frac{-E_A}{K_B T}\right)$$

Here, N_V is the effective density of states in the valence band, v_{th} the thermal velocity, σ_p the capture cross-section, E_A the trap activation energy, K_B the Boltzmann constant, and T the temperature. The frequency around the sharp change in capacitance in CF-profile defines the corresponding trap emission rate; as evident in figure 5.4(c) and (d), this frequency shifts to lower values at lower temperatures. Both MS-profile and CF-profiles clearly indicate the existence of sub-bandgap trap states in DTS-$(FBTTh_2)_2$.

5.3 Maximum Trap Emission Rate

Organic The characteristic-frequency (F_m) at which the change in capacitance is maximum in the CF-profile at a specific temperature, gives the corresponding trap emission rate at that temperature. F_m at different temperatures is identified from the peak of the derivative of the capacitance spectra as illustrated in figure 5.5(a) and 5.5(b) for DTS-$(FBTTh_2)_2$:$PC_{70}BM$ and DTS-$(FBTTh_2)_2$ films, respectively. To determine the tDOS energy spectra utilizing the model of Walter *et al.*[16], it is required to determine the maximum trap emission rate of the material under investigation. The pre-factor in the trap emission rate equation, $N_v v_{th} \sigma_p$, defines the maximum trap emission rate, also called as the attempt-to-escape-frequency (ω_0).[16,31] Linearizing the trap emission rate equation yields,

www.manaraa.com

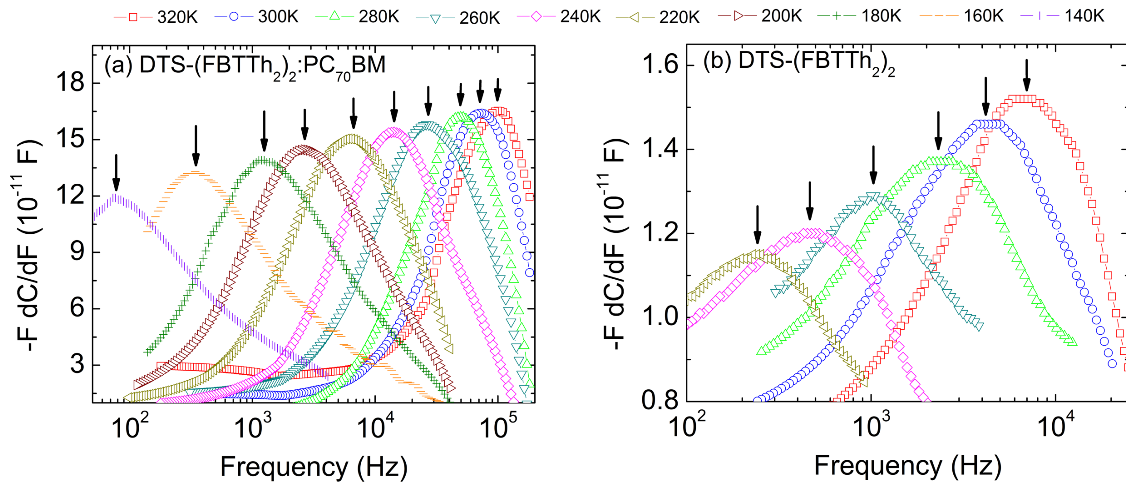

Figure 5.5: Derivatives of the CF-profiles of (a) DTS-$(FBTTh_2)_2$:$PC_{70}BM$ regular-film, and (b) DTS-$(FBTTh_2)_2$ regular-film versus small-signal frequency (at different temperatures). The arrows indicate the characteristic-frequency at which the change is capacitance is maximum.

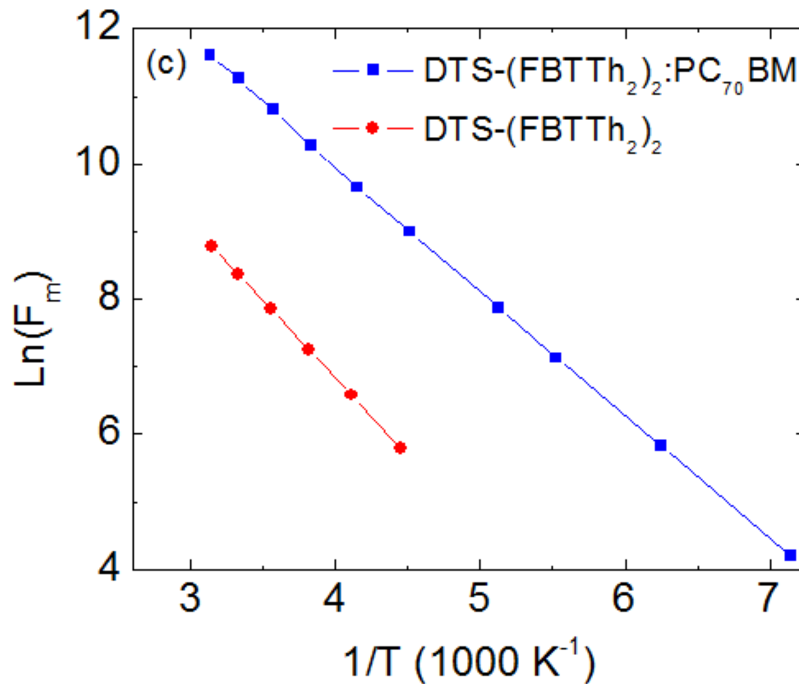

Figure 5.6: Arrhenius plot of the characteristic-frequency (F_m) versus inverse of temperature.

المنارة للاستشارات
www.manaraa.com

$$\ln(e_p) = -\frac{E_A}{K_B T} + \ln(\omega_0)$$

According to this relation, ω_0 and E_A of both DTS-$(FBTTh_2)_2$:$PC_{70}BM$ and DTS-$(FBTTh_2)_2$ films were extracted from the Arrhenius plot of F_m versus inverse temperature, as shown in figure 5.6. The extracted E_A and ω_0 for DTS-$(FBTTh_2)_2$:$PC_{70}BM$ devices are 0.16 eV and 4×10^7 Hz, respectively, while for DTS-$(FBTTh_2)_2$ devices, they are 0.20 eV and 8.5×10^6 Hz, respectively. The extracted ω_0 of both films are in the order of 10^6 to 10^7 Hz while it is commonly in the order of 10^{11} to 10^{13} Hz for inorganics.[11]

5.4 Bulk & Interface Properties

Organic We probed bulk and interface properties of the active-layer and active-layer cathode interface, respectively, to extract and analyze the defect profile in SM-OPVs. Geometric capacitance (C_{geo}) of the films was measured in reverse bias and thickness (d) was measured using AFM and surface profilometer. Using the relation $C_{geo} = \varepsilon A/d$, dielectric constant of DTS-$(FBTTh_2)_2$ was calculated as 3.7 and 3.5 in DTS-$(FBTTh_2)_2$:$PC_{70}BM$ and DTS-$(FBTTh_2)_2$ films, respectively. Doping concentration of the donor material and built-in voltage of the cathode-donor junction were extracted from the MS-profile with employed small-signal frequency high enough to exclude traps. The Fermi energy was calculated using the extracted doping concentration. The extracted parameters are summarized in table 5.2. The doping concentration is in the order of 10^{16} and 10^{15} cm^{-3} for DTS-$(FBTTh_2)_2$:$PC_{70}BM$ and DTS-$(FBTTh_2)_2$ films, respectively. BHJ films had higher doping concentration than neat films and regular-films have higher doping concentration than thick-films.

المنارة للاستشارات
www.manaraa.com

Table 5.2: Summary of extracted bulk and interface properties of DTS-$(FBTTh_2)_2$ and DTS-$(FBTTh_2)_2$-cathode interface, respectively, from CV-profiling and IS.

	125 nm thick DTS-$(FBTTh_2)_2$:$PC_{70}BM$ film	*200 nm thick DTS-$(FBTTh_2)_2$:$PC_{70}BM$ film*	*125 nm thick DTS-$(FBTTh_2)_2$ film*	*200 nm thick DTS-$(FBTTh_2)_2$ film*
Dielectric constant	3.7	3.7	3.5	3.5
Doping (cm^{-3})	2.3×10^{16}	1.3×10^{16}	5.8×10^{15}	3.9×10^{15}
Cathode interface V_{bi} (eV)	0.84	0.83	1.85	2.1
Fermi energy (eV)	0.16	0.17	0.20	0.21
Electron lifetime (µs)	12.5	13.9	…	…
Electron transit-time (µs)	4.2	6.25	…	…
Mobility ($\times10^{-3}$ cm^2/Vs)	2.9	2.7	…	…

The cathode in our devices was Ca (20 nm)/Al (100 nm). For DTS-$(FBTTh_2)_2$:$PC_{70}BM$ films, extracted built-in voltage (0.80 eV) at the cathode interface is equivalent to the difference between the HOMO of DTS-$(FBTTh_2)_2$ (-5.1 eV) and the lowest unoccupied molecular orbital (LUMO) of $PC_{70}BM$ (-4.3 eV); this indicates that Ca work-function is pinned at the $PC_{70}BM$ LUMO level. For DTS-$(FBTTh_2)_2$ films, the built-in voltage is close to the difference between DTS-$(FBTTh_2)_2$ HOMO and Ca work function (-2.9 eV); for this case, Ca work function is not pinned due to the absence of $PC_{70}BM$.

Impedance spectroscopy (IS) was utilized to extract minority-carrier (electron) mobility, transit-time, and lifetime in both regular and thick-films of DTS-$(FBTTh_2)_2$:$PC_{70}BM$.[23-28] Nyquist plots are shown in figure 5.7 and the extracted parameters are summarized in Table 5.2. The IS measurements were conducted by applying a forward bias equal to the corresponding open-circuit voltage; this ensures no extra charge injection and no band-bending which results in no internal electric-field.[23-28] Minority-carrier mobility was extracted utilizing Einstein relation.[24] DTS-$(FBTTh_2)_2$ only films were not probed using IS

المنارة للاستشارات
www.manaraa.com

measurements as there will be no dissociation of excitons due to the absence of acceptors. For the case of blends, a slightly shorter electron lifetime in regular-films indicates a higher amount of recombination than thick-films.[32,33] The higher amount of recombination is an indication of the existence of higher amount of traps in the regular-films. The electron transit-time is lower in regular-films; electrons reaches the cathode faster as the thickness is lower in regular-films. The electron mobility in the regular-film is also slightly higher than the thick-film.

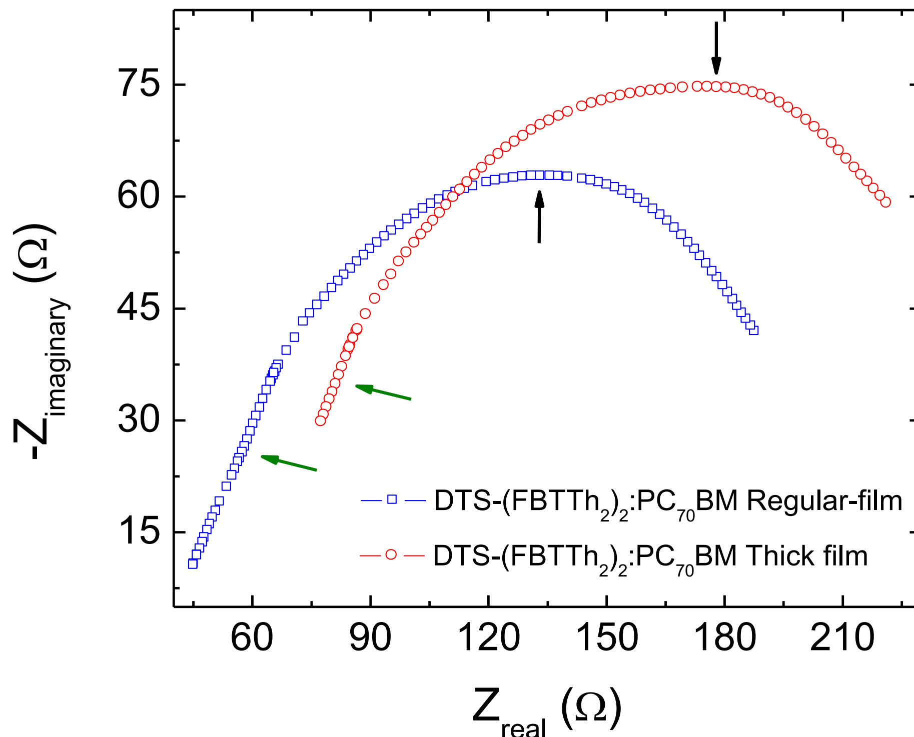

Figure 5.7: Illustration of Nyquist plot of both regular and thick-film of DTS-$(FBTTh_2)_2$:$PC_{70}BM$. The negative of the imaginary part of impedance ($Z_{imaginary}$) is plotted with the real part of impedance (Z_{real}). Data points are obtained applying small-signal frequency ranging from 1 MHz to 100 mHz. The black arrows indicate the peak of the semicircles and the green arrows indicate the quasi-straight line portion of the profile.

المنارة للاستشارات

www.manaraa.com

5.5 tDOS Energy Spectra from Admittance Spectroscopy

We derived the tDOS energy spectra from AS utilizing the model of Walter *et al*.[16] There is a demarcation-energy level, E_ω, corresponding to the small-signal frequency (ω), expressed as,[16,18]

$$E_\omega = K_B T \, ln\left(\frac{\omega_0}{\omega}\right)$$

The tDOS at the demarcation-energy level from the highest occupied molecular orbital (HOMO) level of a p-type semiconductor is expressed as,[16,18,22]

$$N_T(E_\omega) = -\frac{V_{bi}}{qW}\frac{dC}{d\omega}\frac{\omega}{K_B T}$$

Here, W is the depletion width of the metal-semiconductor junction. The obtained tDOS energy spectra of both regular and thick-films of DTS-$(FBTTh_2)_2$:$PC_{70}BM$ and DTS-$(FBTTh_2)_2$ are shown in figure 5.8. A Gaussian band is identified for all films within the energy range shown in figure 5.8. These bands were fitted utilizing Gaussian form[17] and the fitted parameters are summarized in Table 5.3 under the label "Band I", where N_T is the area under the Gaussian distribution and gives the trap concentration, E_0 is the mean energy of the distribution, and σ is the disorder parameter that is the full width at half maximum of the distribution. “Band I” is centered at the corresponding Fermi energy. As free carrier has thermal activation energy of Fermi energy, “Band I” concentration includes a portion of free cariers as well as the continuous energy distribution of defects in the bandgap.[16,18,30] Concentration in “Band I” is in the order of 10^{14} to 10^{15} cm^{-3}. DTS-$(FBTTh_2)_2$:$PC_{70}BM$ films have a higher amount of concentration in "Band I" compared to DTS-$(FBTTh_2)_2$ films,

المنارة للاستشارات
www.manaraa.com

although the band is narrower in the blends. Thus, the introduction of $PC_{70}BM$ as the acceptor material adds defects in the system. Thick-films have less trap concentration in "Band I" than regular-films for both DTS-$(FBTTh_2)_2$:$PC_{70}BM$ and DTS-$(FBTTh_2)_2$. This was expected as the thick-films take longer time than the regular-films to dry, and thus have better self-organization and less morphological disorder[17]. However, the bands of thick-films are broader in the energy spectra. The bands of BHJ films are centered at slightly lower energy than neat DTS-$(FBTTh_2)_2$ films. Bands of regular-films are also centered at slightly lower energy than thick-films.

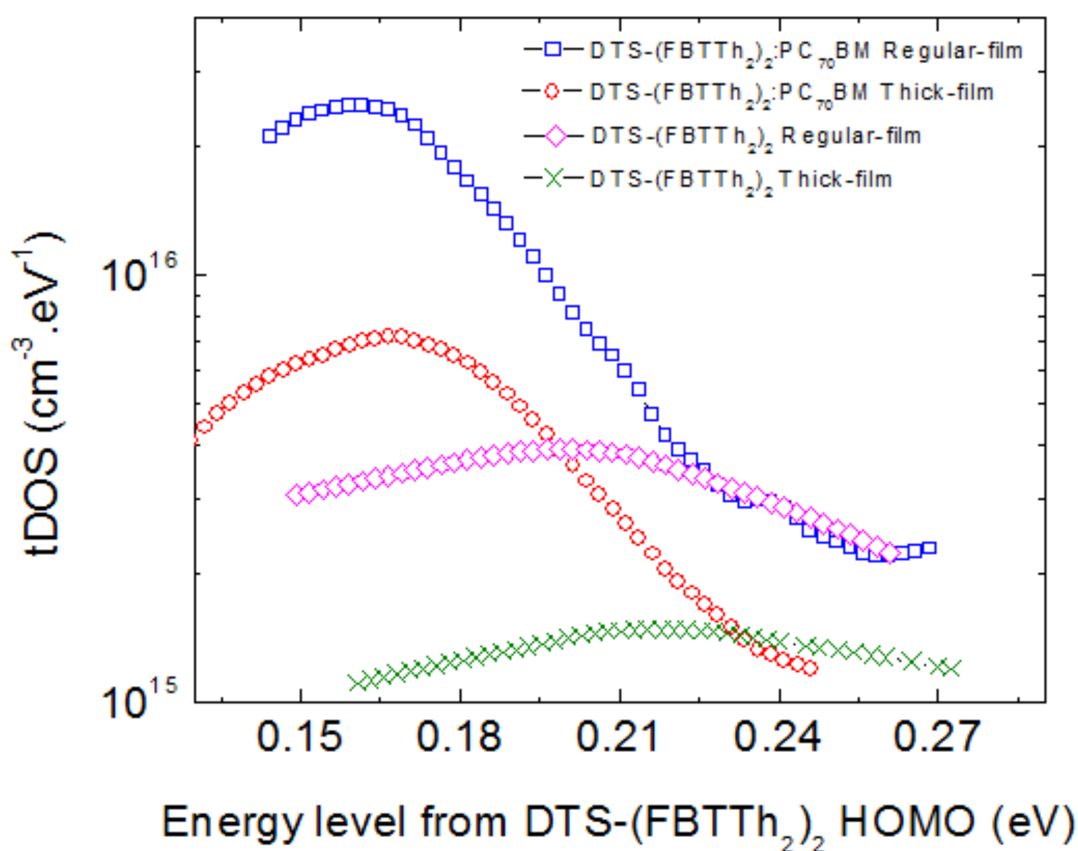

Figure 5.8: Illustration of tDOS energy spectra of regular and thick-films of DTS-$(FBTTh_2)_2$:$PC_{70}BM$ and DTS-$(FBTTh_2)_2$

المنارة للاستشارات
www.manaraa.com

Table 5.3: Summary of extracted fitting parameters from Gaussian fit of the bands in tDOS energy spectra.

		Admittance Spectroscopy			Low-frequency CV-profiling					
		Band I			Band II			Band III		
Film	Thickness (nm)	N_T (cm^{-3})	E_o (eV)	σ (meV)	N_T (cm^{-3})	E_o (eV)	σ (meV)	N_T (cm^{-3})	E_o (eV)	σ (meV)
$DTS(FBTTh_2)_2$:$PC_{70}BM$	125	1.7×10^{15}	0.16	27.2	1.1×10^{16}	0.46	156	2.6×10^{16}	0.86	225
	200	5.8×10^{14}	0.17	33.2	4.3×10^{15}	0.47	127	1.3×10^{16}	0.89	198
$DTS(FBTTh_2)_2$	125	5.3×10^{14}	0.20	54.3	1.2×10^{16}	0.67	62.7	4×10^{16}	0.89	90.1
	200	2.7×10^{14}	0.21	72.5	6.7×10^{15}	0.72	106	1.3×10^{16}	0.89	168

5.6 Probing Deeper Trap States Using Low-frequency CV-profiling

The highest observable energy level in the tDOS energy spectra obtained from AS is limited by the noise at low-frequency small signals. To probe defects at higher energies toward the midgap, we utilized low-frequency CV-profiling. Solving Gauss's law for charge at the depletion edge of a one-sided junction, the spatial distribution of acceptor states in an inhomogeneously doped semiconductor can be expressed as,[14,15]

$$N_A(x) = \frac{\varepsilon}{qx}\frac{dV_{dc}}{dx} = \frac{C^3}{q\varepsilon A^2}\frac{dV_{dc}}{dC}$$

Here, x is the spatial distance from the junction and dx the change in depletion width due to change in applied bias, dV_{dc}. When trap states are pulled below the Fermi level by applying bias, empty trap states become filled; positive donor-type trap states become neutral and neutral acceptor-type trap states become negative.[14,18] As the amount of immobile charge in the depletion region changes with applied bias, the depletion width changes accordingly to

المنارة للاستشارات
www.manaraa.com

cover or uncover an equal amount of charge at the depletion edge.[14] From this principle, this equation can give trap concentration at different energy levels in a homogeneously doped semiconductor, and the energy level of the trap states is determined from the amount of band bending. The trap energy level from the HOMO level can be expressed as,

$$E = q(V_{bi} - V_{dc}) + E_F$$

Here, E_F is the Fermi energy. A change in the measured carrier density with respect to the energy level gives the corresponding tDOS energy spectra. Figure 5.9 illustrates the extracted tDOS energy spectra of regular and thick-films of DTS-$(FBTTh_2)_2$:$PC_{70}BM$ and DTS-$(FBTTh_2)_2$. Two Gaussian bands of trap distribution are present in the tDOS profile of all four films. The fitted parameters of the two Gaussian bands are summarized in table 5.3 under the label "Band II" and "Band III". For comparison of the three bands, figure 5.10 shows the trap concentrations with corresponding mean energy for all four films. Band II is centered around 0.45 eV above DTS-$(FBTTh_2)_2$ HOMO for the case of BHJ films, while it is centered around 0.70 eV for DTS-$(FBTTh_2)_2$ only films. The reported HOMO level of DTS-$(FBTTh_2)_2$ is at -5.1 eV and most of the reports consider the LUMO level of $PC_{70}BM$ to be -4.3 eV.[5,12,29] In that case, the interfacial bandgap between DTS-$(FBTTh_2)_2$ and $PC_{70}BM$ is 0.8 eV. As "Band II" is centered at the midgap of this interfacial bandgap for the case of BHJ films, this band seems to stem from the defect at the donor-acceptor interface. The trap concentration in this band is lower in thick films; this can be the result of the slower drying of the thick films. BHJ films may also have a band of trap distribution around 0.70 eV; but it is not clear in tDOS profile, as shown in Fig. 6(a) and 6(b), due to the existence of other bands near it. For all four

المنارة للاستشارات
www.manaraa.com

films, a Gaussian band of trap states is centered around 0.9 eV, which is the midgap for DTS-$(FBTTh_2)_2$. The trap concentration in this "Band III" is also less in thick-films.

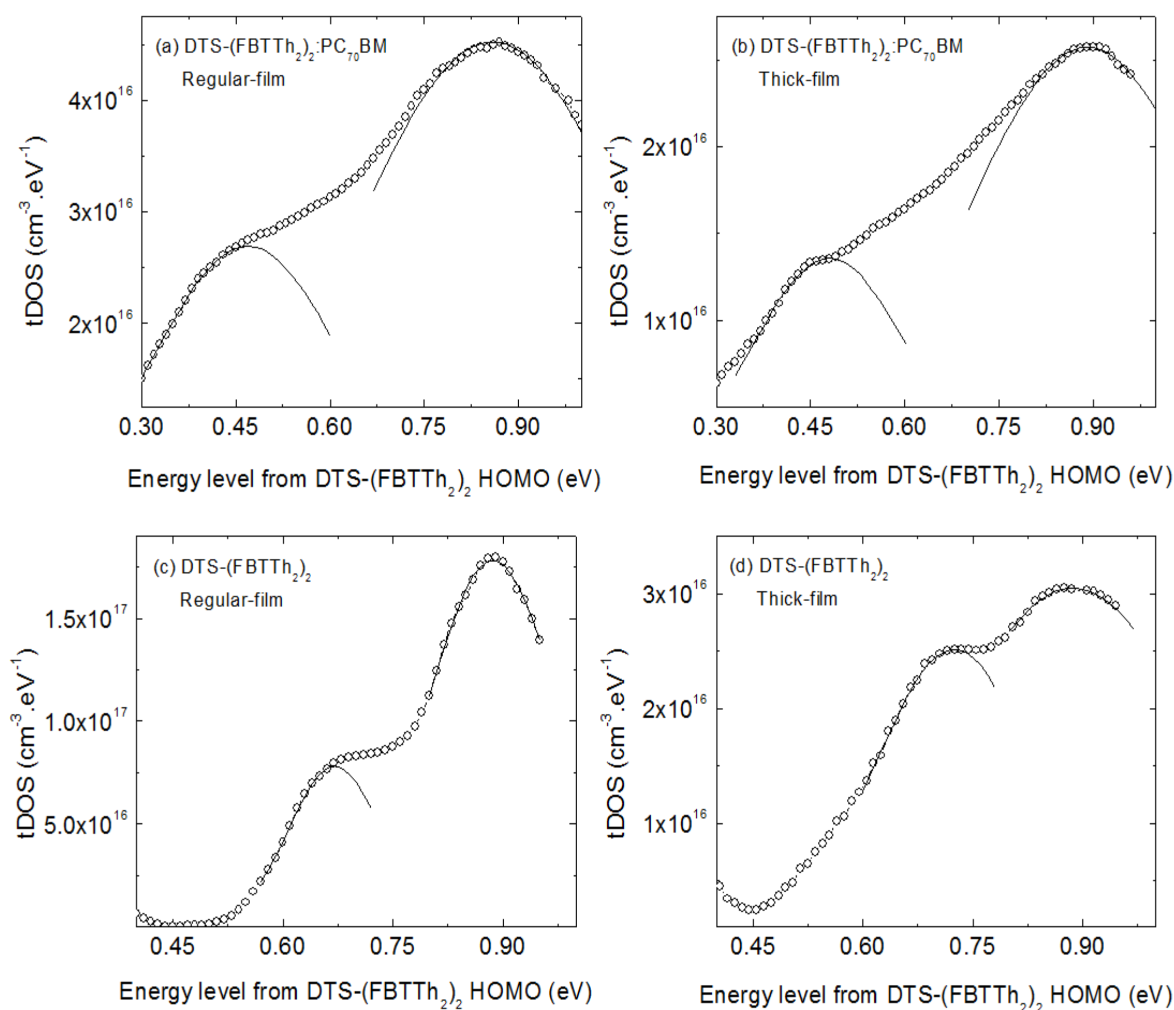

Figure 5.9: Illustration of tDOS energy spectra, extracted from low-frequency CV-profiling, for the regular and thick-films of DTS-$(FBTTh_2)_2$:$PC_{70}BM$ and DTS-$(FBTTh_2)_2$. The solid lines represent the corresponding Gaussian fits.

المنارة للاستشارات
www.manaraa.com

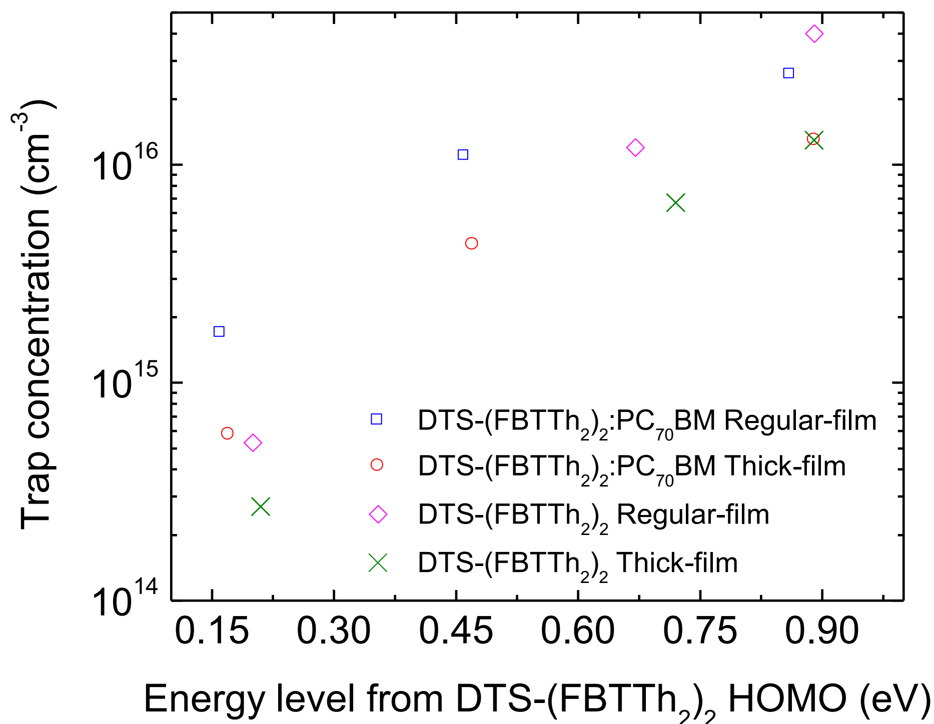

Figure 5.10: Trap concentration of different bands in tDOS energy spectra plotted with corresponding mean energy.

5.7 Conclusion

In summary, we probed the sub-bandgap trap states in DTS-(FBTTh$_2$)$_2$. We identified three separate bands of trap distribution in DTS-(FBTTh$_2$)$_2$ between the Fermi energy level and midgap energy level. We identified a band of defect distribution at the midgap of DTS-(FBTTh$_2$)$_2$ bandgap and we showed that the introduction of PC$_{70}$BM introduces a band of traps at the donor-acceptor interfacial midgap. The distribution of traps centered at the middle of the donor-acceptor interfacial bandgap indicates the importance of exploring acceptor materials other than fullerene-derivatives. Other acceptor materials may introduce less interfacial defects at the donor-acceptor interface; this is expected to improve the PCE. Summation of trap

المنارة للاستشارات
www.manaraa.com

concentrations in three bands lowers by nearly 55% in thick-films, showing that the slower drying rate in thick-films mitigates some traps. The PCE of thick-films were less than regular-films; this is because the required diffusion length is longer in thick-films. So, less amount of charge carriers can reach the electrodes in thick-films compared to regular-films. Thick-films provided us the opportunity to study defects in slower dried films. Lower defect density in slower dried films indicate that PCE of regular films can be improved by slowing down the drying rate after deposition of the active-layer; lower defect density will reduce charge carrier loss through trap-assisted recombination and more charge carriers will reach the electrodes. Conducting solvent annealing at temperatures lower than the room-temperature may make the film drying process slower and new techniques can be investigated.

5.8 Experimental

In Devices were fabricated on ITO coated glass substrates (5-15 Ω/) from Delta Technologies. ITO works as the transparent anode for standard OPV architecture. The substrates were ultrasonicated consecutively in detergent (alconox), de-ionized water and 2-propanol for 10 minutes. The substrates were blown dry with nitrogen and kept on a hot plate at 130^0C for 10 minutes. These were treated with air plasma and then PEDOT:PSS (VP 4083 from HC Stark) was spin coated on top of them at 5000 rpm for 40 seconds as the hole transport layer (HTL) of the device, and finally annealed at 130^0C for 10 minutes before transferring the substrates inside the glove box. The active layer solutions were prepared inside the glove box. DTS-$(FBTTh_2)_2$ and $PC_{70}BM$ from 1-materials Inc. were dissolved in chlorobenzene (CB) from Sigma-Aldrich with a total concentration of 35mg/ml for both DTS-$(FBTTh_2)_2$:$PC_{70}BM$ (3:2 by weight) and DTS-$(FBTTh_2)_2$. 0.4% by volume DIO was added to the solution. These

www.manaraa.com

solutions were stirred at 300 rpm at 60^0C on a hot plate for more than 12 hours and filtered using a 0.22 µm PTFE filter (Sigma-Aldrich). Solutions were heated to 90^0C for 15 minutes before spin coating on the HTL coated ITO slides. Regular-films and thick-films were spin coated at 2000 rpm and 1000 rpm, respectively, for 40 seconds. The spin coated films were solvent annealed for 10 minutes and thermal annealed at 80^0C for 10 minutes. Finally, 20 nm of Ca and 100 nm of Al were deposited sequentially on top of the active-layers as the cathode. Ca and Al were deposited using a thermal evaporator in 10^{-6} mbar vacuum at a rate slower than 0.5 and 5 Å/s, respectively.

CV-profiling was conducted using a PARSTAT 2273 LCR meter and cryostat. The devices were kept under vacuum and in the dark for 30 minutes before starting the measurement to prevent photo-capacitance effects. Impedance spectroscopy (IS) measurements were also conducted using a PARSTAT 2273 LCR meter at room temperature under 1 sun (AM1.5) illumination in air. The Nyquist plots were analyzed using Zsimpwin software. Admittance spectroscopy (AS) was measured using a HIOKI IM3533-01 LCR meter with the samples in the cryostat. A continuous flow of liquid nitrogen coupled with an electric heater in the cryostat was utilized to vary the temperature between 100K and 375K. The temperature was monitored using platinum resistance temperature detectors (RTDs). Light I-V measurements were carried out at a simulated AM1.5G spectrum using an ELH quartzline lamp. A crystalline silicon photodiode coupled with a KG-5 filter was utilized to calibrate the system. Film thickness was monitored using Surface Profilometer and AFM.

المنارة للاستشارات
www.manaraa.com

5.9 References

1. I. Etxebarria, J. Ajuria and R. Pacios, Org Electron **19**, 34-60 (2015).

2. Z. C. He, C. M. Zhong, X. Huang, W. Y. Wong, H. B. Wu, L. W. Chen, S. J. Su and Y. Cao, Adv Mater **23** (40), 4636-+ (2011).

3. S. E. Shaheen, D. S. Ginley and G. E. Jabbour, Mrs Bull **30** (1), 10-19 (2005).

4. Y. Z. Lin, Y. F. Li and X. W. Zhan, Chem Soc Rev **41** (11), 4245-4272 (2012).

5. B. Arredondo, B. Romero, G. Del Pozo, M. Sessler, C. Veit and U. Wurfel, Sol Energ Mat Sol C **128**, 351-356 (2014).

6. A. K. K. Kyaw, D. H. Wang, H. R. Tseng, J. Zhang, G. C. Bazan and A. J. Heeger, Appl Phys Lett **102** (16) (2013).

7. B. Walker, C. Kim and T. Q. Nguyen, Chem Mater **23** (3), 470-482 (2011).

8. Q. Zhang, B. Kan, F. Liu, G. K. Long, X. J. Wan, X. Q. Chen, Y. Zuo, W. Ni, H. J. Zhang, M. M. Li, Z. C. Hu, F. Huang, Y. Cao, Z. Q. Liang, M. T. Zhang, T. P. Russell and Y. S. Chen, Nature Photonics **9** (1), 35-41 (2015).

9. Y. H. Liu, J. B. Zhao, Z. K. Li, C. Mu, W. Ma, H. W. Hu, K. Jiang, H. R. Lin, H. Ade and H. Yan, Nat Commun **5** (2014).

10. J. D. Myers and J. G. Xue, Polym Rev **52** (1), 1-37 (2012).

11. J. A. Carr and S. Chaudhary, Energ Environ Sci **6** (12), 3414-3438 (2013).

12. A. K. K. Kyaw, D. H. Wang, V. Gupta, W. L. Leong, L. Ke, G. C. Bazan and A. J. Heeger, Acs Nano **7** (5), 4569-4577 (2013).

13. V. V. Brus, A. K. K. Kyaw, P. D. Maryanchuk and J. Zhang, Org Electron **15** (9), 2141-2147 (2014).

14. L. C. Kimerling, J. Appl. Phys. 45, 1839 (1974).

المنارة للاستشارات
www.manaraa.com

15. J. D. C. D. V. Lang, Phys Rev B **25** (8) (1982).

16. T. Walter, R. Herberholz, C. Muller and H. W. Schock, J Appl Phys **80** (8), 4411-4420 (1996).

17. K. S. Nalwa, R. C. Mahadevapuram and S. Chaudhary, Appl Phys Lett **98** (9) (2011).

18. P. Z. J. Heath, *Advanced Characterization Techniques for Thin Film Solar Cells*. (2011).

19. M. S. A. Abdou, F. P. Orfino, Y. Son and S. Holdcroft, J Am Chem Soc **119** (19), 4518-4524 (1997).

20. S. Hoshino, M. Yoshida, S. Uemura, T. Kodzasa, N. Takada, T. Kamata and K. Yase, J Appl Phys **95** (9), 5088-5093 (2004).

21. B. G. S. S. Banerjee, *Solid State Electronic Devices*. (Prentice-Hall, 1995).

22. J. A. Carr and S. Chaudhary, J Appl Phys **114** (6), 064509 (2013).

23. A. Kokil, K. Yang and J. Kumar, J Polym Sci Pol Phys **50** (15), 1130-1144 (2012).

24. G. Garcia-Belmonte, A. Munar, E. M. Barea, J. Bisquert, I. Ugarte and R. Pacios, Org Electron **9** (5), 847-851 (2008).

25. J. Bisquert, L. Bertoluzzi, I. Mora-Sero and G. Garcia-Belmonte, J Phys Chem C **118** (33), 18983-18991 (2014).

26. G. Garcia-Belmonte, P. P. Boix, J. Bisquert, M. Sessolo and H. J. Bolink, Sol Energ Mat Sol C **94** (2), 366-375 (2010).

27. B. J. Leever, C. A. Bailey, T. J. Marks, M. C. Hersam and M. F. Durstock, Adv Energy Mater **2** (1), 120-128 (2012).

28. J. Bisquert, J Phys Chem B **106** (2), 325-333 (2002).

29. H. L. Yip and A. K. Y. Jen, Energ Environ Sci **5** (3), 5994-6011 (2012).

المنارة للاستشارات
www.manaraa.com

30. T. Muntasir and S. Chaudhary, J. Appl. Phys. 118 (20), 205504 (2015).

31. M. Samiee, S. Konduri, B. Ganapathy, R. Kottokkaran, H. Abbas, A. Kitahara, P. Joshi, L. Zhang, M. Noack, and V. Dalal, Appl. Phys. Lett. 105, 153502 (2014).

32. T. Muntasir, M. Islam and S. Gupta, 2012 International Conference on Informatics, Electronics & Vision (ICIEV), Dhaka, Bangladesh, 2012, pp. 930-934.

33. T. Muntasir, S. Gupta and M. Islam, 2012 IEEE International Conference on Electron Devices and Solid State Circuit (EDSSC), Bangkok, Thailand, 2012, pp. 1-4.

34. J. E. Anthony, A. Facchetti, M. Heeney, S. R. Marder and X. Zhan, Advanced Materials 22(34), 3876-3892 (2010).

المنارة للاستشارات

www.manaraa.com

CHAPTER VI

POLYMER CRYSTALLINITY & ELECTRONIC DEFECTS IN ORGANIC SOLAR CELLS

We have already investigated the relation between defect density and polymer chain ordering, defects in small-molecule organic solar cells, interfacial defects at the donor/acceptor interface, and relation between defect density and film drying rate. On the next phase of defect study, the relation between polymer crystallinity and electronic defects in organic solar cells was investigated.

6.1 Material Selection

The first thing is selection of materials to work with. In last few years, record-efficiency OPVs were achieved with only three donor polymers and all of these three polymers belong to a specific polymer family based on PTB7.[1] PTB7 film suffer from low crystallinity and PTB7 polymers does not perform well when relatively thick active layers are used in OPV devices partially due to low hole mobility that results from low crystallinity. The polymer structure of PTB7 is shown in figure 6.1.

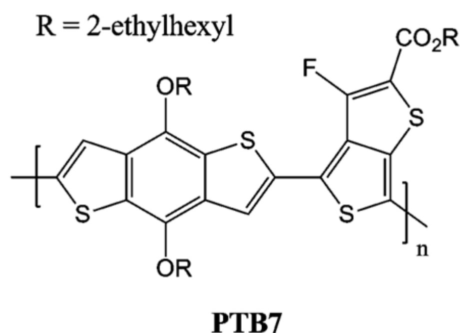

Figure 6.1: Molecular structure of PTB7 polymer

المنارة للاستشارات
www.manaraa.com

PffBT4T-2OD polymer was synthesized recently. This polymer provides >10% efficient organic bulk-heterojunction solar cells.[1] PffBT4T-2OD film has high polymer crystallinity. PffBT4T-2OD polymer performs well when thick active layer (~300 nm) is used in OPV devices due to high crystallinity. The polymer structure of PffBT4T-2OD is illustrated in figure 6.2.

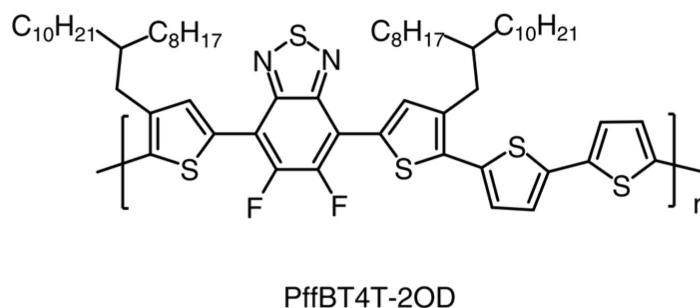

Figure 6.2: Molecular structure of PffBT4T-2OD polymer

As, PffBT4T-2OD is a new polymer that give high efficiency and has basic difference with PTB7, a study on electronic properties of PffBT4T-2OD polymer based organic solar cells was made. A comparative study on PTB7 and PffBT4T-2OD devices provides an opportunity to investigate the relation between polymer crystallinity and defect distribution. A comparison on different properties of PffBT4T-2OD and PTB7 is shown in Table 6.1.

Table 6.1: Comparison of properties between PffBT4T-2OD and PTB7

PffBT4T-2OD	PTB7
• LUMO ~ 3.69 eV • HOMO ~ 5.34 eV • Bandgap ~ 1.65 eV • Absorbs up to ~ 775 nm	• LUMO ~ 3.31 eV • HOMO ~ 5.15 eV • Bandgap ~ 1.8 eV • Absorbs up to ~ 750 nm

المنارة للاستشارات
www.manaraa.com

• Back-bone stacking is parallel to substrate • Face on orientation • Favorable charge transport for photovoltaics • Coherence length ~ 8.5 nm • Hole mobility ~ 2 x 10^{-2} $cm^2/V.s$ • Mostly crystalline	• Back-bone stacking is parallel to substrate • Face on orientation • Favorable charge transport for photovoltaics • Coherence length ~ 2 nm • Hole mobility ~ 5 x 10^{-4} $cm^2/V.s$ • Mostly amorphous

6.2 Sample Organic Solar Cell Preparation

Before investigating the electronic properties of PffBT4T-2OD based organic solar cells, sample cells need to be prepared. PffBT4T-2OD based organic solar cells on both P-i-N and N-i-P structures were prepared. Investigation on both type of structures make sure that the extracted properties are of the polymer of interest.

PffBT4T-2OD device on P-i-N structure

The device structure and associated band-diagram is illustrated in figure 6.3 and 6.4, respectively. At first, we clean the ITO coated glass. PEDOT:PSS is a solution dissolved in water and it is available commercially. This layer is deposited using a spin-coater. The optimum device performance was obtained when spin coating was conducted at 3000 rpm

المنارة للاستشارات
www.manaraa.com

followed by annealing on a hot-plate at 150C. This gives a 30nm thick film that is transparent, conductive and p-type.

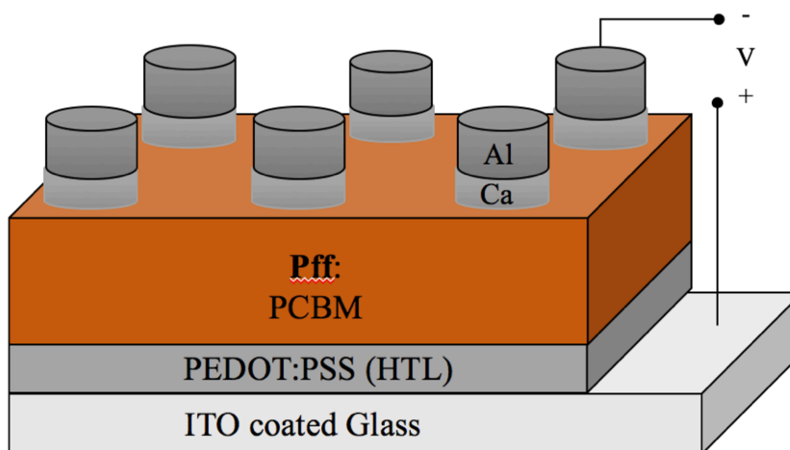

Figure 6.3: Schematic diagram of PffBT4T-2OD based organic solar cell on P-i-N structure

Polymer PCBM blend solution is spin-coated inside a glovebox as it is sensitive to moisture and oxygen. All the process parameters were varied and the optimum device performance was obtained when polymer PCBM ratio in the solution was 1:1.3 and it was dissolved in CB and DCB solvent. It gives best interpenetrating network of donor acceptor. The solution was stirred for 3 days to make sure that it was dissolved well. When 20 mg/ml concentrated solution was spin-coated at 400 rpm, 300 nm thick film was obtained. Thicker film absorbs higher amount of photon energy but the collection of charge carrier degrades due to low diffusion length of charge carriers in organic films. The optimum device performance was obtained when the thickness of the active-layer was 300nm. After spin-coating of the active layer, the samples were kept under a petri-dish so that the films dry slowly which facilitates self organization of donor and acceptor. Then the samples are kept in a vacuum chamber that eases the solvents to leave the film.

المنارة للاستشارات
www.manaraa.com

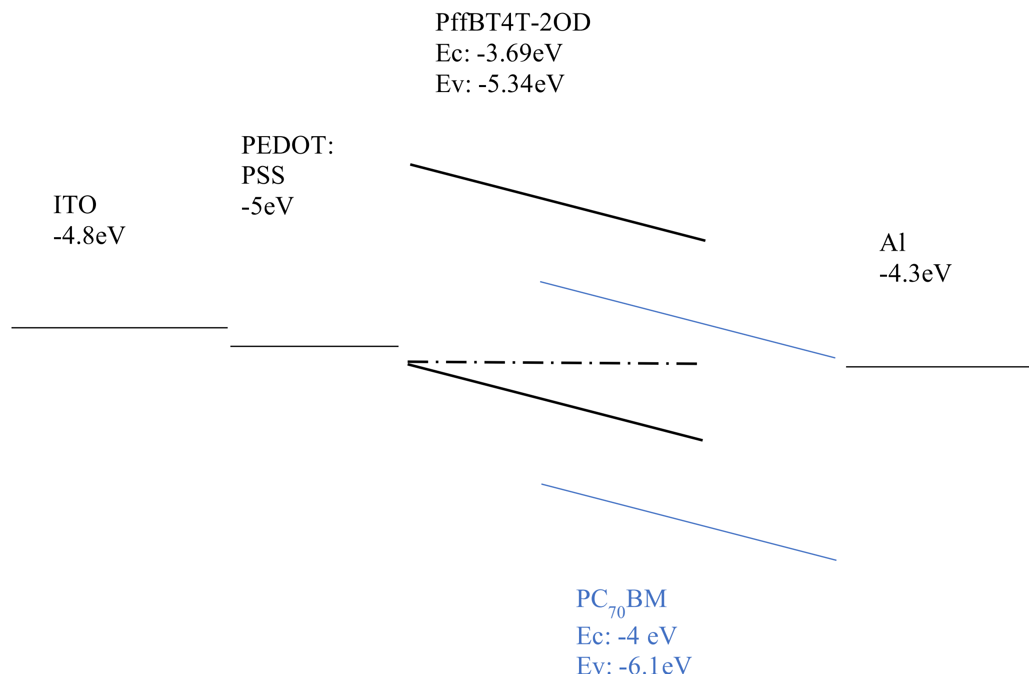

Figure 6.4: Corresponding band-diagram of PffBT4T-2OD based organic solar cell on P-i-N structure.

After solvent annealing and vacuum annealing, the film is thermally annealed at 110^0 C for 5 minutes to make sure only PffBT4T-2OD:PCBM blend is left on the film. Thermal annealing temperature was varied and the optimum devices was obtained when the thermal annealing was conducted at 110^0 C. Polymer crystallinity improves when the thermal annealing temperature is elevated. But, after a certain limit, the donor acceptor domains start to grow larger with higher thermal annealing temperature. This in turn degrades the device performance as the donor-acceptor interfaces area starts to decrease with larger domain sizes.

As the top contact 20nm Ca is thermally evaporated. It was made sure that the vaccum is below 1E-6 torr and rate is slow enough. High rate damages the organic film. Finally 100nm Al is deposited on top of Ca. Initially the rate is around 0.9 A/s and then it is ramped up to 3 A/s.

المنارة للاستشارات
www.manaraa.com

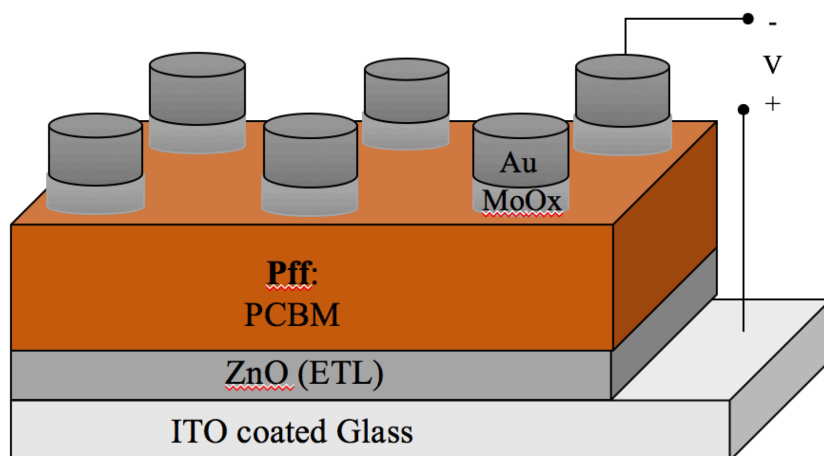

Figure 6.5: Schematic diagram of PffBT4T-2OD based organic solar cell on N-i-P structure

PffBT4T-2OD device on N-i-P structure

The device structure and associated band-diagram is illustrated in figure 6.5 and 6.6, respectively. For the N-i-P structure, Al doped ZnO film is used as the electron transport layer as it is conductive, transparent and n-type. According to literature highest efficiency from N-i-P PffBT4T-2OD cell was obtained when the ZnO layer was spin-coated from Dyehyl zinc solution. But the issue is Dyethyle zinc is pyrophoric and we do not want a pyrophoric material to be a part of our regular process in the lab. So, first I tried ZnO film using a home-made sputtering system. I got the optimum device when I used 80W power, 5 mTorr Ar pressure and set the sample temperature at 150C. The deposition rate at this condition was 40 nm/minute and thickness of the film was 30 nm. To check the device performance with ZnO layer deposited using another technique, I built a ultrasonic-spray pyrolysis system. The system will be explained on next section.

Active layer parameters are same as already explained. The optimum device was obtained when only 6nm of MoOx was deposited as the hole transport layer. Finally 100 nm gold was deposited as the top contact.

المنارة للاستشارات
www.manaraa.com

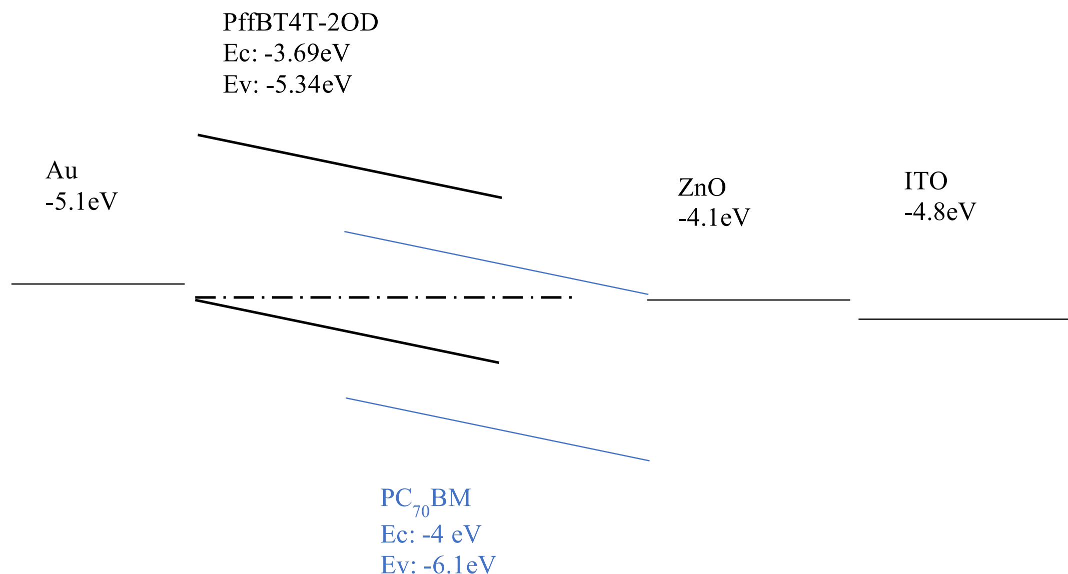

Figure 6.6: Corresponding band-diagram of PffBT4T-2OD based organic solar cell on N-i-P structure.

Ultrasonic-spray pyrolysis setup

The schematic diagram of the ultrasonic-spray pyrolysis setup that was built for this research work is illustrated in figure 6.7. This system was built from the scratch and it took a while to get the system working and deposit transparent, conductive ZnO layer. The basic principle is this chemical reaction:

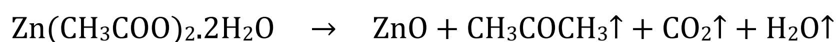

$$Zn(CH_3COO)_2.2H_2O \rightarrow ZnO + CH_3COCH_3\uparrow + CO_2\uparrow + H_2O\uparrow$$

This equation indicates that at high temperature ZnAc decomposes to ZnO. To get a homogenous thin film, we need to flow ZnAc spray through a furnace and keep the sample inside the furnace. To generate the spray, ZnAc solution dissolved in DI water is put in a flask and the flask is clamped in a sonicator. To make the film conductive, Al-nitrate is added in the solution, so the deposited ZnO film is Aluminum doped. When the sonicator is turned on, spray

المنارة للاستشارات
www.manaraa.com

is generated in the flask. To carry this spray to the furnace, 0_2 carrier gas is used. The oxygen cylinder is connected to a regulator and a rotameter by which the flow rate can be controlled. Furnace temperature is controlled by a variable autotransformer. Temperature monitor shows the temperature from the thermocouple. The sample is kept on the sample holder and the furnace temperature is ramped up to 450^0 C. When O_2 carrier gas is flown through the flask, ZnAc spray goes through the furnace and at high temperature it is decomposed into ZnO on the sample.

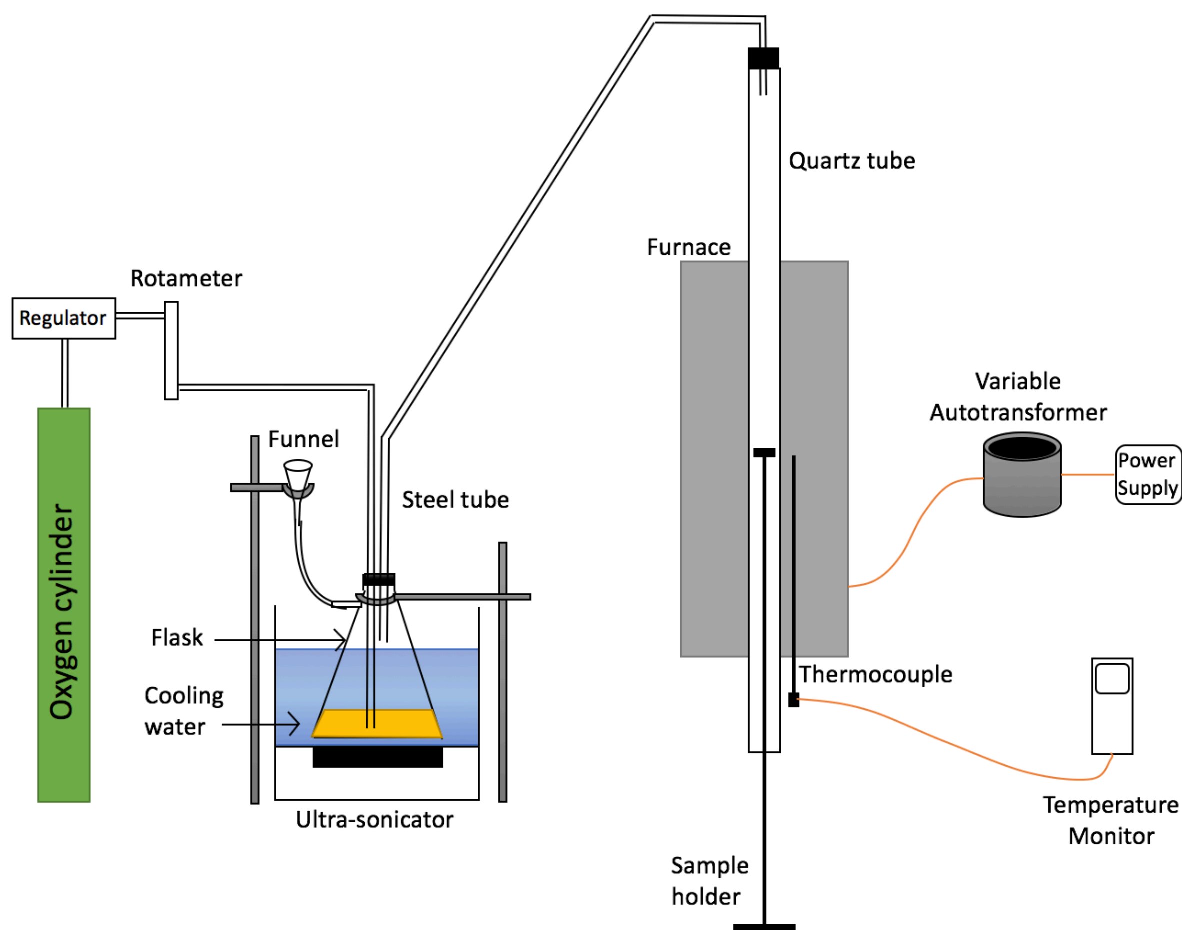

Figure 6.7: Schematic diagram of the ultrasonic-spray pyrolysis setup built for this study

المنارة للاستشارات
www.manaraa.com

Few notable things here: Initially the furnace was in horizontal setup, but the spray was being deposited at the face of the furnace. Then the furnace setup was changed to vertical. Still most of the spray was being condensed in the tube before making there way to the furnace. Then the sonicator was brought closer to the furnace face. Inially the films were not homogeneous, then the flow rate of 0_2 was reduced. Finally, transparent and conductive ZnO film was deposited using this setup.

6.3 Optimized Device Performance

For the case of PffBT4T-2OD based organic solar cell on P-i-N structure, 9.1% power conversion efficiency was achieved after several months of optimization. This is so far the record highest efficiency from PffBT4T-2OD based organic solar cell on P-i-N structure. The light IV curve of this solar cell is presented in figure 6.8. This figure also shows the obtained solar cell parameters. Figure 6.9 shows the corresponding QE spectra.

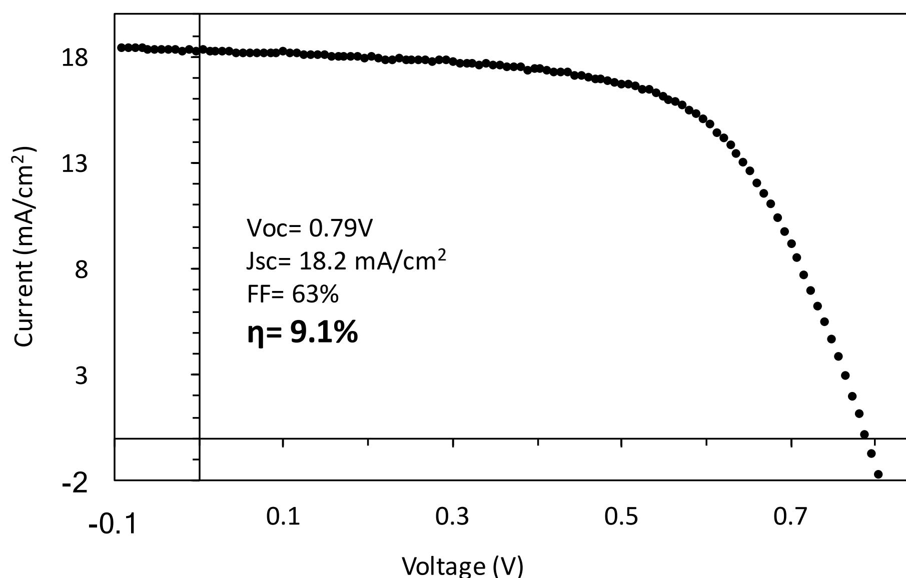

Figure 6.8: Light IV curve of the optimized PffBT4T-2OD solar cell on P-i-N structure

www.manaraa.com

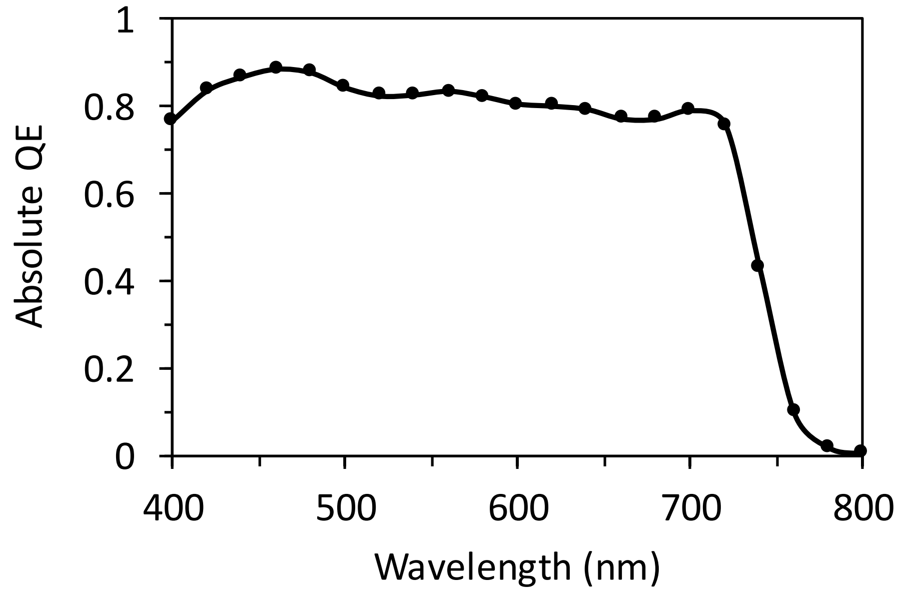

Figure 6.9: QE spectra of the optimized PffBT4T-2OD solar cell on P-i-N structure

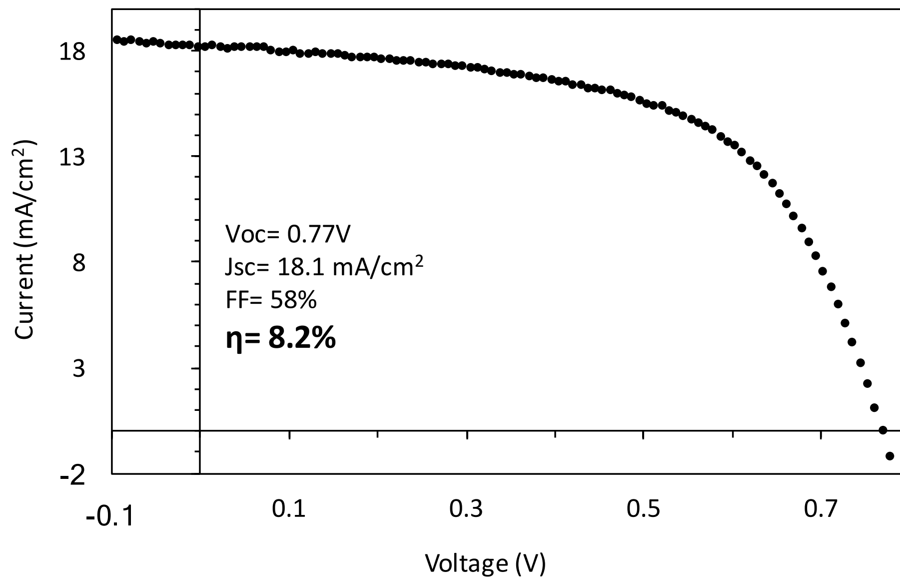

Figure 6.10: Light IV curve of the optimized PffBT4T-2OD solar cell on N-i-P structure

المنارة للاستشارات
www.manaraa.com

For the case of PffBT4T-2OD based organic solar cell on N-i-P structure, 8.2% power conversion efficiency was achieved. The light IV curve of this solar cell is presented in figure 6.10. This figure also shows the obtained solar cell parameters in the inset. Figure 6.9 shows the corresponding QE spectra. For P-i-N device, open circuit voltage was 0.79V while for N-i-P 0.77V. Current density was similar 18 mA/cm^2. For P-i-N fill-factor was 63% while for N-i-P 58%.

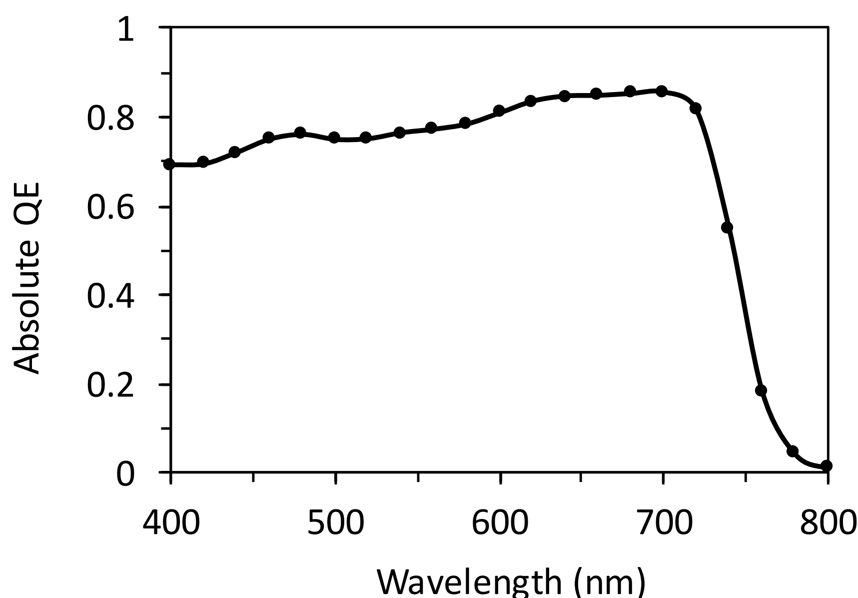

Figure 6.11: QE spectra of the optimized PffBT4T-2OD solar cell on N-i-P structure

For the purpose of comparing defects based on polymer crystallinity, PTB7 devices were also prepared. PTB7 is known to be amorphous and PffBT4T-2OD is known to be crystalline. Following the standard procedures, 7.4% efficient PTB7 device was obtained which is decent efficiency for this type of cell. The corresponding light IV, QE and device structure is illustrated in figure 6.12.

المنارة للاستشارات

www.manaraa.com

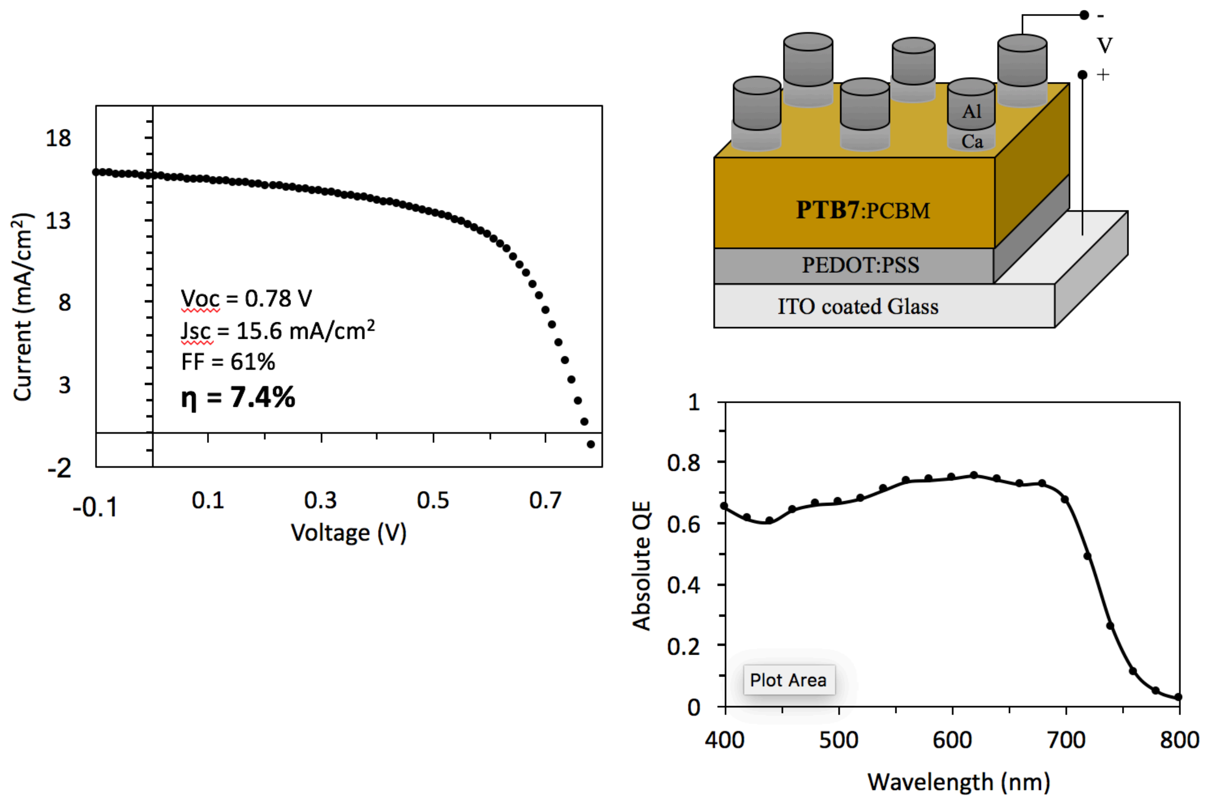

Figure 6.12: Light IV with device parameters, QE plot and device structure of PTB7 device.

6.4 Probing Polymer Crystallinity using Raman Spectroscopy

Polymer crystallinity was probed using Raman spectroscopy. In the top left plot in figure 6.13, the red dots are experimental data collected on the PffBT4T-2OD film and the black line is the single peak fitting. Top right plot of figure 6.13 is the figure for PTB7 film. Obtained Raman spectra is asymmetric and broad. Bottom left plot in figure 6.13 shows the double peak fitting for PffBT4T-2OD film. During fitting the blue curve was kept fixed at wavenumber 1439.4 where we get the peak for PffBT4T-2OD solid and this curve corresponds to the crystalline form of PffBT4T-2OD. The green curve was kept fixed at the wavenumber 1454 where we get the peak of melted PffBT4T-2OD and this curve corresponds to the

المنارة للاستشارات
www.manaraa.com

amorphous form of PffBT4T-2OD. The black line is the convolution of blue and green curves. Bottom right plot of figure 6.13 shows the similar case for PTB7 film. Table 6.2 shows the crystalline and amorphous peak position of PffBT4T-2OD and PTB7 film.

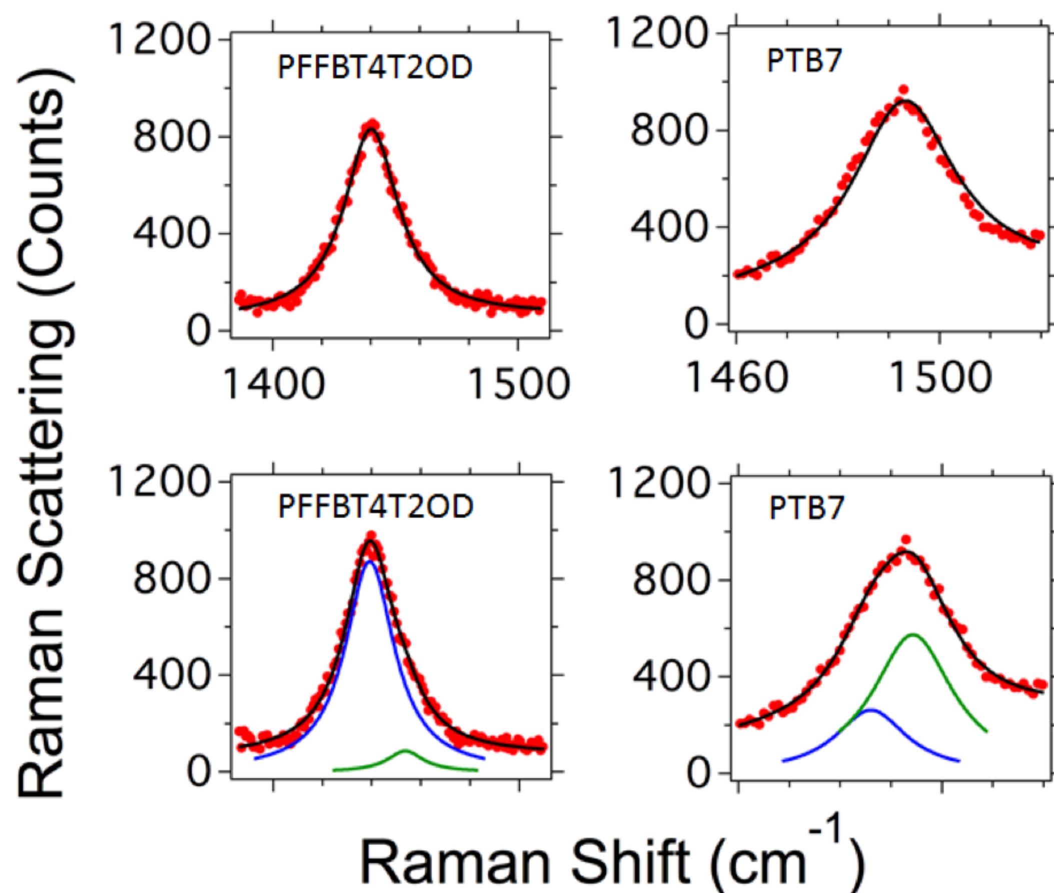

Figure 6.13: Obtained Raman spectra from PffBT4T-2OD and PTB7 films. Top two plots show single peak fitting and bottom two plots show double peak fitting.

Table 6.2: Crystalline and amorphous peak position of PffBT4T-2OD and PTB7 film.

	PffBT4T-2OD		PTB7	
	Peak 1	Peak 2	Peak 1	Peak 2
Average	1439.4	1454	1488	1496
Standard dev.	0.3	2	2	2

المنارة للاستشارات
www.manaraa.com

Crystallinity parameter is obtained from the ratio of the intensity of the crystalline peak and the summation of crystalline and amorphous peak. This table summarizes the crystallinity parameter measured on 3 samples. We found that PffBT4T-2OD film is 93% crystalline and PTB7 film is 40% crystalline.

Table 6.3: Summary of crystallinity parameter of PffBT4T-2OD and PTB7 film.

Crystallinity Parameter		
	PffBT4T-2OD	**PTB7**
1	0.91	0.30
2	0.92	0.59
3	0.95	0.31
Average	0.93	0.4
Std. dev.	0.02	0.2

6.5 Defect Study Based on Polymer Crystallinity

In this study, defect profile of both PffBT4T-2OD devices and PTB7 devices was investigated. In this way, we know how polymer crystallinity play role on defect profile as we know that PffBT4T-2OD film is crystalline and PTB7 film is amorphous.

Net defect density

As discussed in chapter 3, net defect density in the material can be extracted applied CV-profiling on the device. While CV-profiling conducted at high frequency gives the doping concentration, CV-profiling at low frequency gives the net defect density. Extracted Mott-

المنارة للاستشارات

www.manaraa.com

Schottky profile from both PffBT4T-2OD and PTB7 films are illustrated in figure 6.14. The extracted parameters are summarized in table 6.4.

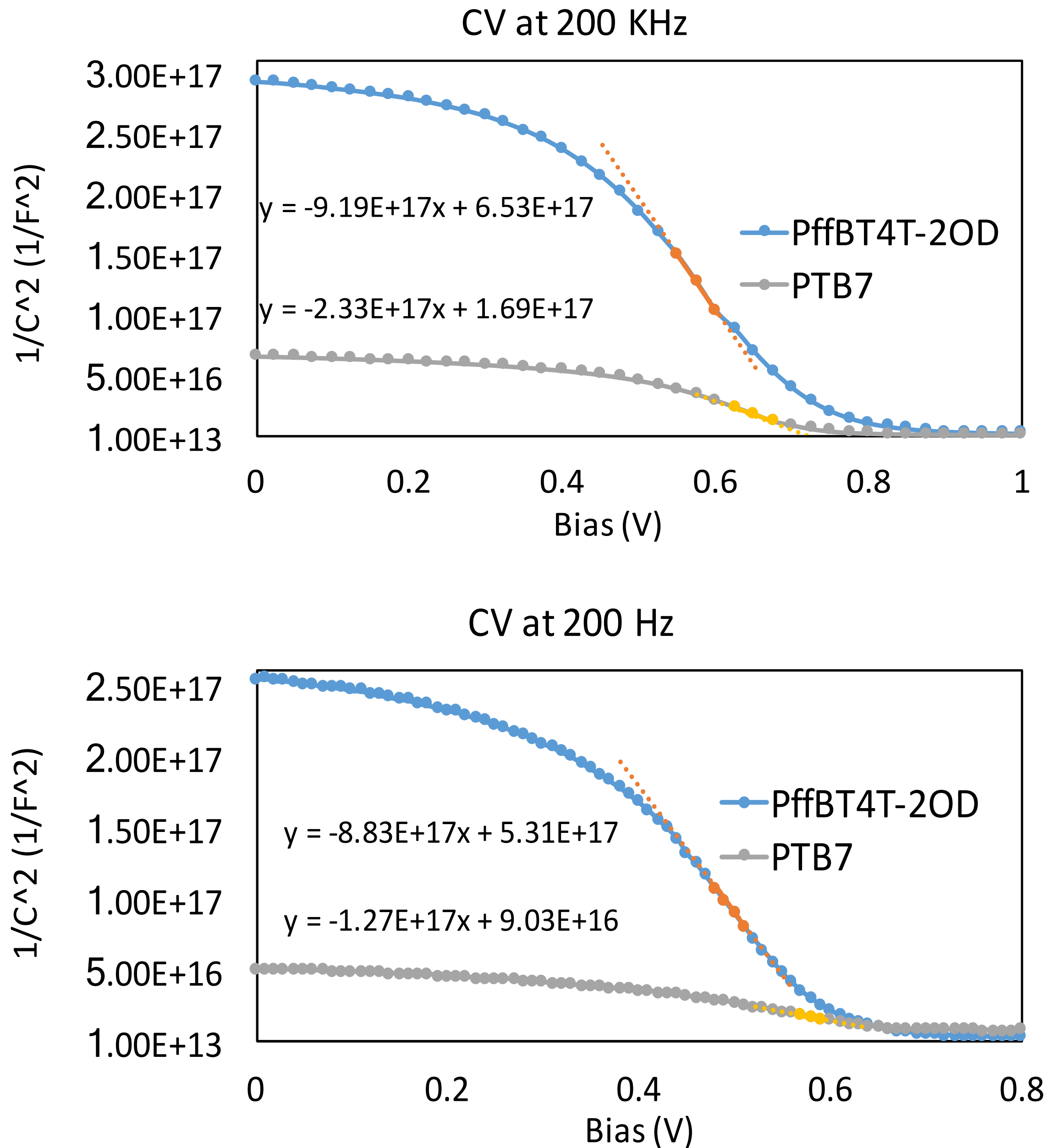

Figure 6.14: Illustration of Mott-Schottky profile of PffBT4T-2OD and PTB7 films. The top figure is extracted from CV-profiling at high frequency and the bottom figure is extracted from CV-profiling at low frequency.

www.manaraa.com

Table 6.4: Summary of extracted parameters from CV-profiling on PffBT4T-2OD and PTB7 films.

	PffBT4T-2OD	PTB7
Doping (/cm^3)	3.15×10^{15}	1.10×10^{16}
Vbi (V)	0.71	0.73
Fermi Energy (eV)	0.21	0.18
Doping + Defect density (/cm^3)	3.35×10^{15}	2.10×10^{16}
Net Defect density (/cm^3)	2.00×10^{14}	1.00×10^{16}

From CV at high frequency, we found doping concentration in PffBT4T-2OD is in the order of 10^{15} while in PTB7, it is 10^{16}. From low frequency CV measurement, obtained defect density is 2 times 10^{14} while in PTB7 defect density is 2 order of magnitude higher. From this result we conclude that net defect density is significantly higher in amorphous films compared to crystalline films of organic semiconductors.

Trap DOS energy spectra

Trap DOS (tDOS) energy spectra of PffBT4T-2OD film was extracted for both P-i-N and N-i-P devices. These profiles were compare with the one of PTB7. This comparison is illustrated in figure 6.15. This figure shows the trap distribution in the bandgap of PTB7 and PffBT4T-2OD both in P-i-N (standard) and N-i-P (inverted) structures.[2,3,5] The defect distribution is similar in PffBT4T-2OD film from both structures confirming this obtained defect distribution is coming from the polymer. Now, if we compare PffBT4T-2OD with PTB7, we see the defect distribution is significantly lower in PffBT4T-2OD film. Our Raman study shows that Pff film is 90% crystalline while PTB7 film is only 40% crystalline.

المنارة للاستشارات
www.manaraa.com

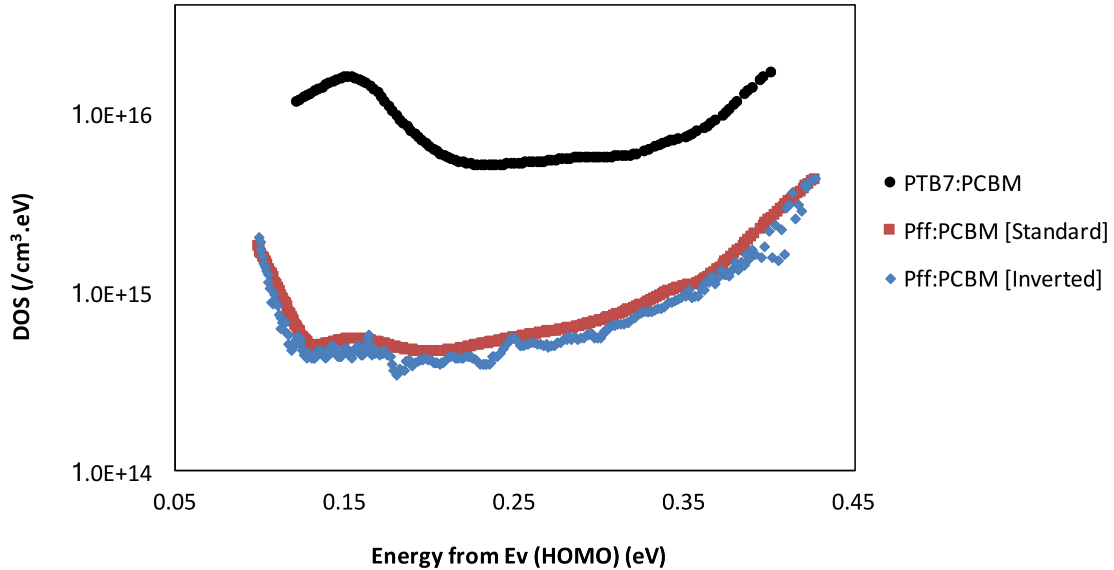

Figure 6.15: Illustration of trap distribution in the bandgap of PTB7 and PffBT4T-2OD in both P-i-N (standard) and N-i-P (inverted) structure.

This comparison shows that polymer crystallinity plays important role in defect distribution in the bandgap. This is the first time we show the relation between polymer crystallinity and electronic defects in organic solar cells.

Tail states

Tail states can be investigated using Sub-gap QE measurements. In this measurement, the device is illuminated by light of specific wavelengths. So, the photon energy is controlled in this experiment. We have a home-made setup to measure electronic excitation at different photon energies. If we shine the device with photon energy less than the bandgap of the semiconductor, there will be no signal. If we shine the device with photon energy higher than or equal to the bandgap energy of the semiconductor, we will get signal from the device. Figure 6.16 illustrates the outcome of this experiment conducted on PTB7 device as well as PffBT4T-2OD devices on both structures.

www.manaraa.com

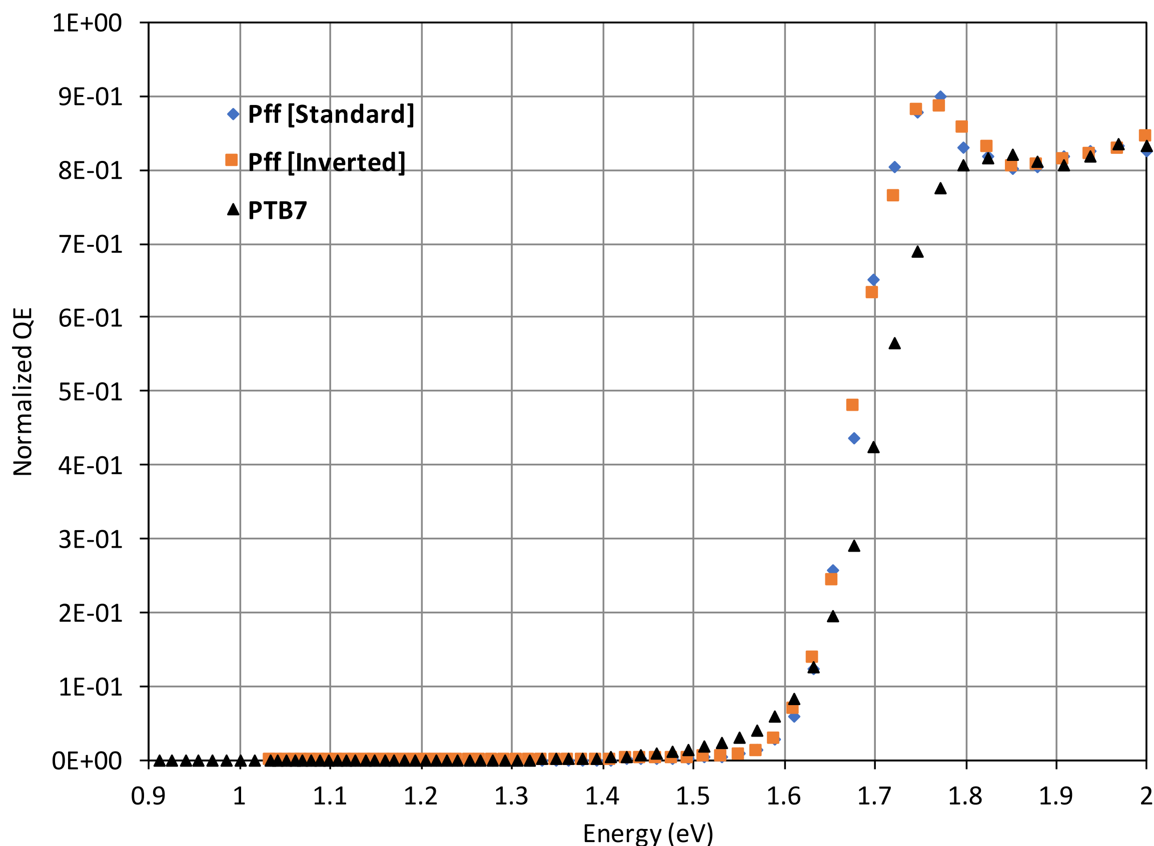

Figure 6.16: Normalized QE plotted with photon energy for PTB7 and PffBT4T devices on both structures.

From figure 6.16, it is apparent that electronic transition from HOMO to LUMO of the polymer takes place when the device is illuminated by photon energy equal to or higher than the bandgap energy of the semiconductor. For the case, when there are tail states present in the bandgap, electronic transition also takes place at photon energy less than the bandgap energy. This phenomenon is understood when figure 6.16 is plotted on semi-log scale as illustrated in figure 6.17. [4,6]

www.manaraa.com

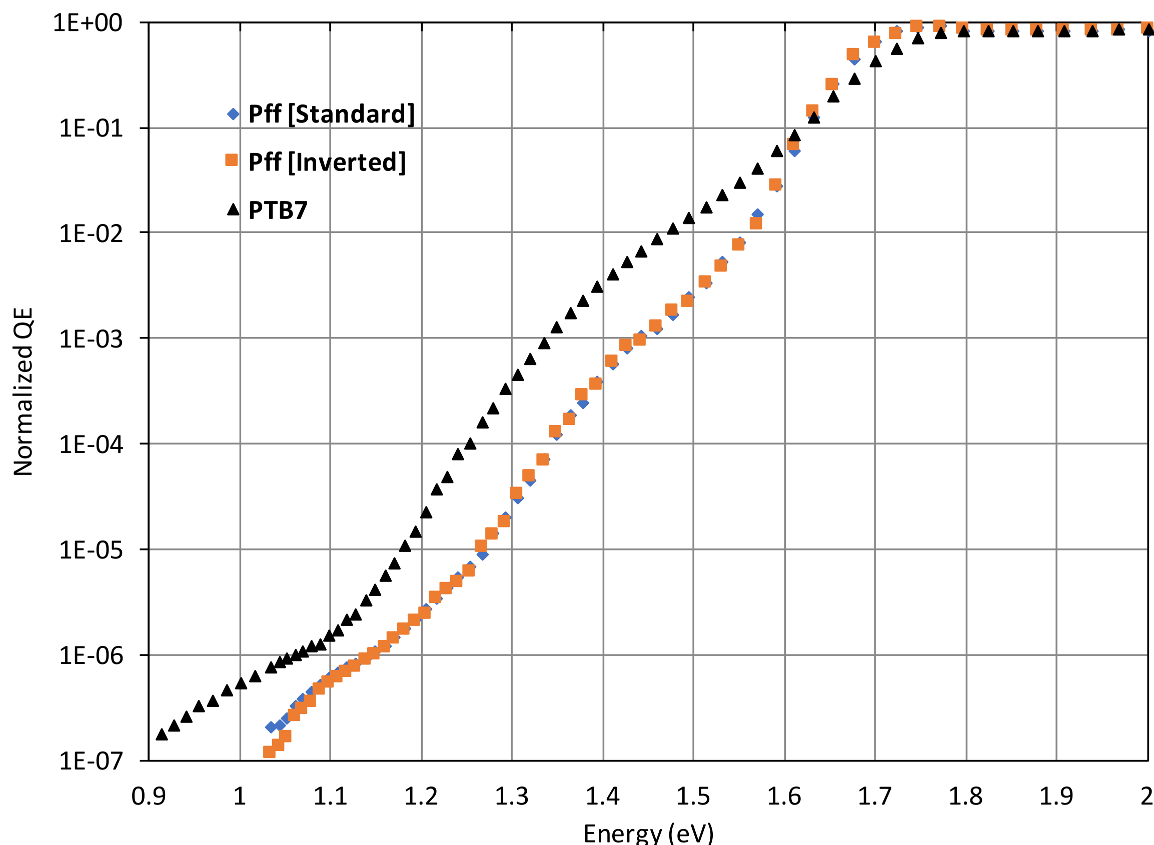

Figure 6.17: Normalized QE plotted with photon energy on semi-log scale for PTB7 and PffBT4T devices on both structures.

Here the black curve is from PTB7 device and the orange and blue one from PffBT4T-2OD N-i-P (inverted) and P-i-N (standard) device. In the high energy region, the excitation is from valence band (HOMO) to conduction band (LUMO). To explain this figure let's take a look at the PffBT4T-2OD:PCBM and PTB7:PCBM type-II heterojunction illustrated in figure 6.18. We can see that PffBT4T-2OD has lower bandgap. The band-to-band excitation starts at lower energy for PffBT4T-2OD confirming lower bandgap.

المنارة للاستشارات
www.manaraa.com

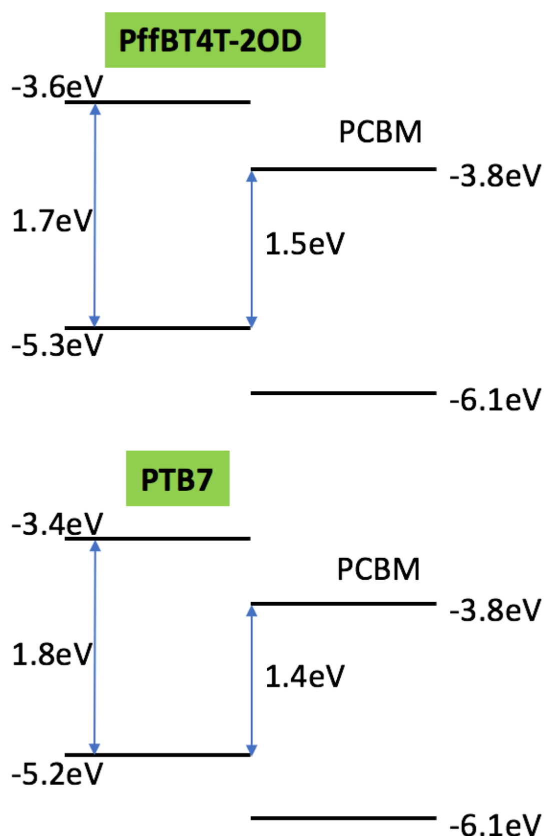

Figure 6.18: Illustration of the PffBT4T-2OD:PCBM and PTB7:PCBM type-II heterojunction.

Below band-to-band excitation, there is a rapid fall in excitation at lower photon energy and in this region, there is a change in the slope as band-to-band excitation at the interface takes place here. We see interfacial bandgap is higher in PffBT4T-2OD and our result shows that this change occurs at higher energy in PffBT4T-2OD compared to PTB7, confirming higher interfacial bandgap in PffBT4T-2OD device.

Now, in the region around 1.5 to 1.7 eV, electronic excitation occurs via the tail states near the conduction band and from the slope of this region we can get the Urbach energy which indicate the depth of tail states. The result shows PffBT4T-2OD film possess significantly less amount of tail states near conduction band (LUMO) compared to PTB7. Urbach energy for

المنارة للاستشارات
www.manaraa.com

PffBT4T-2OD is 28meV while for PTB7 it is 55meV. So, polymer crystallinity plays major role in tail states. These extracted values are summarized in table 6.5.

From the region around 1.2 to 1.4 eV, we get Urbach energy for tail states near valence band (HOMO) as excitation through them takes place at this energy. The result shows both Pff and PTB7 have similar tail states near valence band.

Table 6.5: Extracted Urbach energy of tail states near HOMO and LUMO of PffBT4T-2OD and PTB7.

Urbach energy	**PffBT4T-2OD**	**PTB7**
Tail states near conduction band (LUMO) (meV)	28	55
Tail states near valence band (HOMO) (meV)	38	33

6.6 Conclusion

In conclusion, a comparative study on polymer crystallinity and defect profile was made utilizing PffBT4T-2OD polymer which has high polymer crystallinity and PTB7 polymer which has low polymer crystallinity. Record solar cell efficiency of PffBT4T-2OD device on P-i-N structure is obtained optimizing the process parameters than also minimized the defects in the system. Crystalline film was found to inherit two order of magnitude less defect than amorphous film.

المنارة للاستشارات

www.manaraa.com

6.7 References

1. Yuhang Liu, Jingbo Zhao, Zhengke Li, Cheng Mu, Wei Ma, Huawei Hu, Kui Jiang, Haoran Lin, Harald Ade & He Yan, Nature Communications 5, Article number: 5293 (2014)
2. T. Muntasir and S. Chaudhary, J. Appl. Phys. 118 (20), 205504 (2015).
3. T. Muntasir and S. Chaudhary, J. Appl. Phys. **119**, 025501 (2016).
4. M. Samiee, S. Konduri, B. Ganapathy, R. Kottokkaran, H. Abbas, A. Kitahara, P. Joshi, L. Zhang, M. Noack, and V. Dalal, Appl. Phys. Lett. 105, 153502 (2014).
5. J. Bhattacharya, R. W. Mayer, M. Samiee and V. L. Dalal, Appl Phys Lett **100** (19) (2012).
6. Mehran Samiee, Pranav Joshi, Damir Aidarkhanov, and Vikram Dalal, Appl. Phys. Lett. 105, 133511 (2014)

المنارة للاستشارات
www.manaraa.com